# Optoplasmonic Biosensor for Lung Cancer Telemedicine: Classical and Quantum Approach


**Alemayehu Getahun Kumela**

**A Dissertation Submitted to the Department of Applied Physics**

**School of Applied Natural Science**

**Presented in the Partial Fulfilment of the Requirements for the Degree of Doctor of**

**Philosophy in Physics**

**(Laser Spectroscopy)**

**Office of Graduate Studies**

**Adama Science and Technology University**

**October 2023**

**Adama, Ethiopia**

# Optoplasmonic Biosensor for Lung Cancer Telemedicine: Classical and Quantum Approach

**Alemayehu Getahun Kumela**

**Supervisor: Abebe Belay (Prof.)**

**Co-supervisor: Alemu Kebede (Ph.D.)**

**A Dissertation Submitted to the Department of Applied Physics**

**School of Applied Natural Science**

**Presented in the Partial Fulfilment of the Requirements for the Degree of Doctor of**

**Philosophy in Physics**

**(Laser Spectroscopy)**

**Office of Graduate Studies**

**Adama Science and Technology University**

**October 2023**

**Adama, Ethiopia**

# Declaration

I declare that this dissertation entitled **Optoplasmonic Biosensor for Lung Cancer Telemedicine: Classical and Quantum Approach** is my own work and has not been submitted to any university for a similar purpose. The references used in this dissertation are duly recognized by proper citations.

| Alemayehu Getahun Kumela | _____ | _____ |
|---|---|---|
| Name of student | Signature | Date |

## RECOMMENDATION OF SUPERVISORS

We, the supervisors of this research, hereby certify that we have closely supervised the student while developing this dissertation and read the draft dissertation entitled **Optoplasmonic Biosensor for Lung Cancer Telemedicine: Classical and Quantum Approach** prepared under our guidance by **Alemayehu Getahun Kumela**. Therefore, we recommend the submission of the dissertation to the department for further review and evaluation.

| Abebe Belay Gemta | _____ | _____ |
|---|---|---|
| Supervisor | Signature | Date |

| Alemu Kebede Hordofa | _____ | _____ |
|---|---|---|
| Co-supervisor | Signature | Date |

# Approval Page

We hereby certify that the recommendation and suggestion given by the dissertation review committee is appropriately incorporated into the dissertation entitled **Optoplasmonic Biosensor for Lung Cancer Telemedicine: Classical and Quantum Approach** by **Alemayehu Getahun Kumela**.

| | | |
|---|---|---|
| Abebe Belay Gemta | _____ | _____ |
| Supervisor | Signature | Date |
| Alemu Kebede Hordofa | _____ | _____ |
| Co-supervisor | Signature | Date |

# Approval of Board of Reviewers

We, the undersigned, members of the board of reviewers of the dissertation open defense by **Alemayehu Getahun Kumela** have read and evaluated the dissertation entitled **Optoplasmonic Biosensor for Lung Cancer Telemedicine: Classical and Quantum Approach** and assessed the understanding of the candidate about the research. This is, therefore, to certify that the the dissertation is accepted and we recommend the implementation of the dissertation.

| | | |
|---|---|---|
| Chairperson | Signature | Date |
| Reviewer-1 | Signature | Date |
| Reviewer-2 | Signature | Date |

Finally, approval and acceptance of the the dissertation is contingent upon the submission of its final copy to the Office of Postgraduate Studies (OPGS) through the Department Graduate Council (DGC) and School Graduate Committee (SGC).

| | | |
|---|---|---|
| Department Head | Signature | Date |
| School Dean | Signature | Date |
| Office of Postgraduate Studies, Dean | Signature | Date |

# List of Acronyms

| | |
|---|---|
| 2D | Two-dimensional |
| Biosignals | Biological Signals |
| CML | Classical Machine Learning |
| DA | Detection Accuracy |
| FOM | Figure of Merit |
| FWAHM | Full Width at Half Maximum |
| GGG | Gadolinium Gallium Garnet |
| IG | Information Gain |
| LCCD | Lung Cancer Clinical Data |
| LITT | Laser Interstitial Thermal Therapy |
| LOD | Limit of Detection |
| LSPR | Localized Surface Plasmon Resonance |
| MI | Molcule Induced |
| MNS | Metallic Nanno Surface |
| MS | Metallic Surface |
| NLO | Non Linear Optics |
| OBs | Optical Biosensor |
| OPB | Optoplasmonic Biosensor |
| SERS | Surface Enhance Raman Spectroscopy |
| SI | Surface Induced |
| SPP | Surface Plasmonic Polariton |
| RIU | Refractive Index Unit |

# Contents

# List of Figures

# List of Tables

# Acknowledgment

I would like to take this opportunity to express my sincere gratitude and appreciation to the individuals who have contributed significantly to my successful journey in completing my PhD dissertation. Their unwavering support, guidance, and encouragement have played a pivotal role in my achievements, and I am deeply grateful to each and every one of them.

First and foremost, I would like to extend my heartfelt thanks to the Almighty God for bestowing upon me good health, strength, and resilience throughout the entire dissertation process. I am immensely indebted to my supervisor, Prof. Abebe Belay, for his limitless support, close guidance, timely response, and effective supervision. His expertise, dedication, and willingness to share his knowledge have been invaluable in shaping the trajectory of my research. His enthusiasm for my success and belief in my capabilities have motivated me to strive for excellence.

I would also like to express my sincere appreciation to my co-supervisor, Dr. Alemu Kebede, for his valuable contribution to my research. His insights, suggestions, and feedback have significantly enhanced the quality and depth of my work. His dedication and commitment to my academic growth have been truly inspiring.

I am profoundly grateful to my family for their unwavering support throughout this rigorous academic journey. To my loving wife, Ruth Birhanu, your constant encouragement, patience, and understanding have been a source of strength for me during challenging times. To my father, Getahun Kumela, and my mother, Gobbine Angessa, your belief in my abilities and your continuous support have been a driving force behind my accomplishments. To my brothers, sisters, and son (Eyosias Alemayehu, Eliyad Alemayehu), thank you for standing by my side and ensuring that I had the moral and material support needed for the successful

completion of my work.

Last but not least, I would like to extend my gratitude to all the fellow PhD candidates in the ASTU physics department. The camaraderie, intellectual discussions, and support we shared have made this journey more enjoyable and meaningful. The stimulating academic environment and the exchange of ideas have shaped my research and broadened my perspectives.

To each and every person mentioned above, and to those who have assisted me silently along the way, please accept my heartfelt thanks for your invaluable contributions. Your unwavering support, dedication, and belief in my abilities have been crucial to my success in completing my PhD dissertation.

# Abstract

*Recently, the healthcare industry has faced significant pressure due to the factors such as population growth, escalating medical equipment costs, and the rising prevalence of complex diseases. As a result, there has been a notable shift towards electronic consulting, telediagnosis, and remote treatment as means of overcoming such physical constraints. In this research, the classical and quantum approaches were developed for lung cancer telemedicine. The classical methods utilized to investigate the impact of noble metallic nanosurface (NMNS) thickness and biomolecule concentration on the performance of optoplasmonic biosensor (OPB). The result indicated that, the nonlinear intensity have more broader spectra than linear, absorption cross section increase with size of NMNS, scattering cross section have inversely proportional with NMNS size, and silver nanosurface (Ag NS) exhibits more robust plasmonic properties than gold and aluminum NS. Notably, the addition of eight layers of Ag NS yields optimum sensitivity (10421 nm/RIU), and increasing biomolecule concentration leads to increase signal response. In addition, the lung cancer biosignals extracted from the OPB are correlated with patient information in the cloud using quantum machine learning (QML) techniques, to determine the appropriate doses of laser interstitial thermal therapy (LITT). The findings reveal that, as the quality and quantity of lung cancer clinical data (LCCD) improved, the accuracy of diagnosis increases. Moreover, through the utilization of quantum teleportation techniques, the biosignals and LITT are successfully teleported between two remote health stations with fidelity rates of 96% for biosignals and 98% for LITT doses. This shows the proposed telemedicine schemes is anticipated solutions for long-distance faithful lung cancer telemedicine.*

**Keyword:** Optoplasmonic Biosensor, Lung Cancer, Telediagnosis, and Telemedicine.

# 1

# Introduction

## 1.1 Background

Cancer is a leading cause of death worldwide, accounting for nearly 10 million deaths in 2020 (Kargbo, 2022). Around one-third of cancer deaths are due to tobacco use, high body mass index, alcohol consumption, low fruit and vegetable intake, and lack of physical activity (Kais and Hamdi, 2022). A combination of genetic factors as well as external agents such as chemicals, physical agents, and biological carcinogens leads to the growth of abnormal cells beyond their normal bounds, which is a major cause of cancer disease. On the other hand, cancer-causing infections, such as human papillomavirus (HPV) and hepatitis, are responsible for approximately 30% of cancer cases in low and lower-middle-income countries (Pazzi et al., 2023).

Cancer can be classified by its stages, proliferating rate, and organ of origin (breast, brain, lung, skin, etc.). From the all, lung cancer tends to be more aggressive and has a lower survival rate compared to several other cancer types (Lemjabbar-Alaoui et al., 2015). This is due to factors such as environmental factors (including exposure to secondhand smoke, air pollution, and certain occupational hazards), late-stage diagnosis, rapid tumor growth, and the tendency of lung cancer to metastasize early to other parts of the body (Shi et al., 2021). Lung cancer can be cured if detected early and treated effectively (Roy and Saikia, 2016). Thus, the advancement of early diagnosis techniques has proven to improve

cancer patients' survival rates.

Recently, in order to diagnose and identify the stage of lung cancer, extensive diagnostic modalities such as magnetic resonance imaging (Bainbridge et al., 2017), chest X-rays (Gohagan et al., 2005), positron emission tomography (Bastarrika et al., 2005), sputum cytology (Doria-Rose et al., 2009), etc) were developed. However, those techniques have required a combination of several imaging studies to ensure the accuracy of the diagnosis (Altintas and Tothill, 2013). As a result, those methods are time-consuming, costy, and inappropriate for patients with other pathology (Shintani et al., 2017). Therefore, in order to overcome the above-mentioned problems, biosensors of various kinds (mechanical, electrochemical (Liu et al., 2018b), and optical (Prabhakar et al., 2018)) have been introduced. In particular, optical biosensors (OBs) offer high sensitivity, selectivity, cost-effective, and easily engineered (Jha et al., 2020).

Several simulations and experimental work have been reported to improve the performance of sensor and the cost of OBs (Yan et al., 2020). The effect of physical properties of dielectric materials (SiC, $TiO_2$, $Si_2O$, and $Fe_2O_3$) (Graniel et al., 2018) and shiny metallic nanoparticles (MNPs) (Ag, Au, Al, and Cu) has been investigated with different geometric structures (such as nanoscale mushrooms, nanocheckerboard, and nanopyramids) (Si et al., 2021). The efficiency of OBs has been determined using: limit of detection (LOD), specificity, sensitivity, and quality factor (Tseng et al., 2020).

So far, with further work on incident angle, azimuthal angle, and polarization, the excellent performance and distinct spectral features of OBs like: surface plasmon resonance (SPR) (Rich and Myszka, 2000), localized SPR (LSPR)(Haes et al., 2004), and surface-enhanced Raman scattering (SERS) (Lin et al., 2023)) were introduced. The unique features such as: fast detection, simplicity, high accuracy, better stability, real-time monitoring, and high sensitivity make the SPR sensors widely preferred (Nangare and Patil, 2023).

On the other hand, several lung cancer treatment techniques like surgery (Forrest et al., 2013), chemotherapy (El-Hussein et al., 2021), radiation (Stenmark et al., 2012), and laser interstitial thermal therapy (LITT) (Beechar et al., 2018) was reported. In contrast, LITT is more accurate, has fewer risks, and a shorter recovery time than other treatment techniques (Cardia et al., 2023). It can be applied through a thin fiber placed inside the body to shrink and damage only the tumor cells, and can be used for breast, brain, skin, head, neck, cervical, and lung cancers (Pang et al., 2022). Nd: Yag lasers (1064 nm) are commonly used as a laser source in LITT (Bozinov et al., 2020). However, the substantial cost of LITT installation has far outpaced that of other medical specialties like telemedicine (Samanta et al., 2021). Thus, a real-time, low-cost, and multi-user SPR-based telemedicine platform is needed (Wang et al., 2022b). As a suggestion, quantum teleportation-based telemedicine methods are fascinating platforms to connect two distant locations healthcare stations for sharing diagnosis equipment and medical doctors through biosignal and dose of LITT teleportation, with highly secured, specific detection, and reproducible responses (Kumela et al., 2023a).

It's noteworthy that the recent telemedicine platform is experiencing heavy file traffic when it's being utilized with multiple skills and a variety of environments between the host and second healthcare stations (Albahri et al., 2021). To address these issues, several pioneers developed high computing techniques by training computers to mimic intelligent human behavior using a variety of algorithms (machine learning (ML)) (Steinkamp and Cook, 2021). A combination of mathematics, statistics, and computer science can be used to accomplish these tasks. In a recent report, ML is widely applied to record responses to medications based on patient conditions, it is also used to classify lung cancer sub-types, and discover new therapies by employing representation, evaluation, and optimization techniques, respectively (Yang et al., 2022).

Thus, classical and quantum ML models have been dispensed based on their efficiency as shown in (Díaz-Santos and Escanez-Exposito, 2023). Classical ML

(CML) algorithms use statistical techniques such as classification, regression, and segmentation to predict new data by finding patterns and trends (Yadavendra and Chand, 2020). The main drawbacks of CML are that it takes an extended period, requires large amounts of data, can be prone to over-fitting, and does not scale well when dealing with large and complex medical datasets (Nazir et al., 2021). These factors led to the development of quantum machine learning (QML), which has the advantages of responsive model training, enhanced accuracy, and reduced reliance on human-derived data (Azevedo et al., 2022). In contrast with CML, QML encounters the disadvantage of loading clinical data from classical machines into qubits (Wei et al., 2023). Thus, several works provide encoding, processing, and measurement or prediction procedures for the quantization of classical medical data to develop efficient and personalized treatment methods for lung cancer and related complex diseases (Yang et al., 2020).

In this research, we have developed a highly secured, efficient and personalised lung cancer telemedicine platform in which an optoplasmonic biosensor, a quantum-based biosignal processing system, as well as quantum-classical hybrid machine learning algorithms can be utilized.

## 1.2 Statement of the Problem

According to World Health Statistics (WHS) 2022, lung cancer is the second most common and killer disease in the world (Siegel et al., 2023). Much experimental and theoretical research has been proclaimed on early treatment methods. However, failing to achieve cost effectiveness, optimum sensitivity for diagnostics, and the availability of well-trained physicians. The extensive work on design shape, material type, and thickness clock in for cost and sensitivity improvement. While, to share expensive medical equipment, skilled labor, save treatment time, and reduce disease transmission scales, telediagnosis has been developed yet. However, most of today's telemedicine platform encounters low security, limited data transmission speed, and low image quality and efficiency. Thus, the application of

quantum technology in telemedicine has the power to revolutionize healthcare by ensuring secure and efficient communication, improving diagnostic accuracy, and enabling precise remote monitoring for better patient care.

Therefore, this dissertation work developed an effective optoplasmonic biosensor using classical model, and quantum information processing and computing to connect two remotely located healthcare stations employing quantum model. With the classical model, we determined the optical properties of light, NMNS, MS and biological samples interactions like; intensity, absorption cross-section, scattering cross-section, extinction cross-section, sensitivity, selectivity, and figure of merit. In addition, with the quantum model we investigated; biosignal processing, teleportation of biosignals, and teleportation of doses of LITT. The proposed telemedicine platform minimize patients extra diagnosis time and budget expense, government foreign currency, and medical sectors equipment installation, maintenance, and space budget.

## 1.3 Objectives of the Study

### 1.3.1 General Objective

The general objective of this research is to investigate the quantum and classical model of optoplasmonic biosensor and biosignal processing platform to develop an effective and accurate lung cancer telemedicine.

### 1.3.2 Specific Objectives

The specific objective of this work are to:

- develop the classical and quantum models of light-matter interaction to optimize the surface plasmon polariton properties for optoplasmonic biosensors application.
- design and analysis optoplasmonic biosensor performance for lung cancer telediagnosis, via developing the teleportation scheme of biosignals between two distant located healthcare station.

- compute quantum machine learning for estimation and teleportation of dose of LITT to perform effective lung cancer telemedicine.

## 1.4 Significance of the Study

This research provides new insights into the optoplasmonic biosensor for quantum-based lung cancer telediagnosis and telecare systems. The output of this work helps the medical engineer to construct a cost-effective, accurate, and efficient lung cancer telecare platform. In addition, the theoretical physicist may use mathematical procedures to develop further medical instrument models. Furthermore, the analysis presented in this study will convey valuable information for future research to explore the various medicinal benefits of classical and quantum models of light-matter interactions. Moreover, the commercial availability of designed OPBs will help to control the early-stage and prostrate lung cancer disease over 95%.

## 1.5 Delimitation and Scope

This study primarily focuses on the numerical modeling of optoplasmonic biosensors with the classical and quantum approaches to enhance the sensitivity of optoplasmonic biosensors, teleportation of biosignals, classification of lung cancer to determine doses of LITT and teleportation of LITT for remote-based lung cancer detection and treatment techniques. However, the delimitations of this work were it did not include the experimental and engineering part of the optoplasmonic biosensors.

The research work in this dissertation structured as follows. In chapter one the background, objectives, scope and statement problem of the dissertation were discussed. In chapter 2, lung cancer classification, diagnosis and treatment mechanisms, classification of biosensors, classical and quantum model of surface plasmon polariton biosensors, and classical and quantum machine learning were discussed. In addition, the concept and theories necessary for a better understanding of the light-matter interaction, classical and quantum modeling of optical

biosensors, classical and quantum machine learning for cancer classification, and quantum teleportation-assisted medical techniques were discussed in detail.

In chapter three materials and methods are presented. In the first section, the list of software, optical components, and data sources that are commonly used to conduct research described are point out. In the second section, methods used in this study such as mathematical modeling of biosensors, biosensor-laser light interaction, quantum machine learning for biosignal processing, quantization and teleportation of biosignals, and LITT dose are discussed briefly.

In Chapter four, the results and discussion of the dissertation were presented. The first section discusses the optical properties of noble metallic nanoparticles for plasmonic biosensor applications. In the second section, the sensor region-biological analyte interaction, biosignal processing, quantum machine learning for lung cancer classification, prediction of dose of laser light for lung cancer treatment, and teleportation of dose LITT for lung cancer telemedicine were presented in the last section of this chapter.

Finally, in chapter five the conclusion, recommendations, and future work of the overall work was discussed.

# 2

# Literature Review

This chapter introduces lung cancer classification, recent dignosis and medication techniques by employing the classical and quantum perspectives of light-matter interactions in a plasmonic biosensor. With detailed classifications, causes and spreading mechanisms of each lung cancer subclass. This was followed by an analysis of each diagnosis mechanism in terms of cost, time, material, and method efficiency, as well as different plasmonic biosensor modeling schemes. The detail theoretical foundation of plasmonic biosensors in terms of classical and quantum mechanical principles were dispensed. The class of plasmonic biosensor is discussed in terms of its pros and cons as well as its development scheme. We briefly discusses the recent lung cancer treatment techniques, finally this chapter discusses the details progress of recent digital technology like classical machine learning, quantum machine learning, and quantum teleportation applications in lung cancer telemedications.

## 2.1 Lung Cancer Classification

The bronchioles and alveoli are the major areas where lung cancer typically develops (Boubertakh et al., 2022). Lung cancer is a complex and diverse disease with various sub-types, each having distinct molecular features and clinical outcomes. Accurate classification of lung cancer is essential for tailoring treatments and improving patient prognosis. Oncologists recently categorized lung cancer from histopathological to molecular and genomic approaches, to enabling personalized

therapeutic approaches.

### 2.1.1 Histopathological classification

Histopathology involves examining tissues and/or cells under a microscope to diagnose and study diseases of tissues (Wolf et al., 2015). Basically, these classifications are primarily based on the microscopic characteristics of tumours, morphological identifiable cell types and histological patterns using light microscopy and conventional staining techniques (Slaoui and Fiette, 2011). Under these classification, lung cancer is classified into primary and secondary (Venturini et al., 2020). Primary lung cancer is caused by malignancy in the lungs, which leads to lung lesions as-whole. Further, it restricts into small-cell lung carcinomas (SCLC) and non-small-cell lung carcinomas (NSCLC) (Tammemägi et al., 2022). In SCLC, the tumor starts in neuroendocrine cells of the lung that are usually caused by smoking and tends to spread fair early (Siegel et al., 2023). While, NSCLC is the most common type (80%) and it was further classified into squamous-cell carcinoma, adenocarcinoma, and large-cell carcinoma. Typically, squamous cell carcinomas develop within the airways of the lung and associated with smoking (Boubertakh et al., 2022). Adenocarcinoma and large cell carcinomas can be appeared in any part of the lung, grow faster, and are difficult to treat compared to other types of lung cancer (Selenica et al., 2022).

On the other hand, secondary lung cancer are neoplasms that spread from primary lesion of other parts of the body to the lung, as a result of primary cancer cells break away and move through the bloodstream or lymphatic system and form a new tumour in the lung (Venturini et al., 2020). It may typically appear as well-circumscribed and identified by its site of origin. It is a late-stage, the outcome varies from person to person, and difficult to treat (Ho et al., 2021). To this end, recent advancements in immunohistochemistry and molecular profiling have improved the precision of histopathological classification, enabling the identification of specific sub-types and providing guidance for targeted therapies.

### 2.1.2 Molecular classification

The molecular classification of lung cancer has revolutionized the field of oncology by providing a more precise understanding of the underlying biology of the disease (Rodriguez-Canales et al., 2016). This classification has not only enhanced diagnosis and prognostication, but has also paved the way for targeted therapies and personalized medicine (Kamel and Al-Amodi, 2017). Specifically, in lung cancer classification various genomic techniques such as next-generation sequencing (NGS) and gene expression profiling were applied (Arora and Tollefsbol, 2021). These approaches have revealed the heterogeneity of lung cancer at the molecular level and have identified several key molecular alterations that drive the development and progression of the disease. Thus, the NSCLC further classified into several sub-types based on specific molecular alterations, such as epidermal growth factor receptor (EGFR) mutations, anapestic lymphoma kinase (ALK) rearrangements, and ROS1 rearrangements (Wigle et al., 2002). These molecular alterations have been shown to have prognostic and predictive implications, as patients with these alterations may respond better to targeted therapies (Siegal, 2016).

In addition, recently several molecular alterations in SCLC, such as loss of tumor suppressor genes TP53 and RB1, as well as amplification of MYC family genes are articulated (Skoulidis and Heymach, 2019). These molecular alterations have provided insights into the underlying biology of SCLC and potential therapeutic targets. Further, besides to NSCLC and SCLC, other rare sub-division of lung cancer, such as adenocarcinoma with lepidic growth pattern and neuroendocrine tumors, have also been characterized at the molecular level (Inamura, 2017).

To summarize, challenges such as access to molecular profiling assays, standardization of classification systems, and incorporating the latest advancements into clinical practice need to be addressed. Future research should focus on refining classification methods to improve accuracy, minimize inter observer variability,

and identify additional genomic markers to optimize treatment outcomes for patients with lung cancer.

## 2.2 Recent Lung Cancer Diagnosis Techniques

Lung cancer screening and the use of novel tools to manage early cancer have brought several challenges (Shankar et al., 2019). The practicality of more precisely identifying those who are at risk and the use of less invasive treatments may preserve the quality of life and increase the survival of many lung cancer patients, despite epidemiological disagreement surrounding lung cancer screening (Roch et al., 2020). Over years several diagnosis techniques (like: imaging, biomarkers, tissue sample, biosensors etc) are under development. With this aim the proceeding subsections reveal the recent diagnosis platforms with their historical development, diagnosis techniques, efficiency, and drawbacks.

### 2.2.1 Biomarkers

Biomarkers, including molecular, genetic, and protein-based markers, have emerged as valuable tools for several cancer diagnosis, prognosis, and targeted treatment selection (Tainsky, 2009). Lung cancer biomarkers are proteins, hormones, or pieces of DNA that cancer cells/bodies release in response to cancer infection. Physicians test for these biomarkers in blood, urine, other bodily fluids, stool, and tissues (Baghel et al., 2021). Some drawbacks of biomarkers in lung cancer diagnosis are: i) biomarker assays may produce false-positive or false-negative results, leading to misdiagnosis (Nevraumont et al., 2022), ii) biomarker expression levels can vary among individuals, making it challenging to establish universal cutoff values for diagnosis or prognosis (Blennow et al., 2015), iii) some biomarkers may lack adequate sensitivity and specificity to distinguish lung cancer from other lung diseases or accurately predict patient outcomes (Phillips et al., 2008), iv) biomarker analysis often requires obtaining tissue samples or blood samples with adequate tumor-derived material, which may not always be feasible or of sufficient quality, and v) biomarkers need extensive validation and standardization across differ-

ent laboratories and platforms to ensure their clinical utility and reproducible (Blennow et al., 2015).

Therefore, extensive research efforts should been applied to overcome these limitations and validating promising biomarkers to improve early detection, prognosis assessment, and personalized treatment selection in lung cancer patients.

### 2.2.2 Tissue Sample

Tissue sampling techniques involve the collection of cells or tissues from suspected lung cancer lesions for histopathological examinations (Sun et al., 2013). To determine the cancer type, stage, and molecular markers useful for personalized treatment strategies. This techniques provide important information about tumor histology and molecular characteristics (Ofiara et al., 2014). Thus, surgical resection, transthoracic needle aspiration, and bronchoscopy with biopsy are commonly used tissue sample techniques (Yung, 2003). However, these techniques also have limitations and drawbacks that need to be addressed effectively. Some are: limited sample availability, sampling errors and false-negative results, invasive nature and complications, inadequate tumor representation, and patient discomfort and anxiety (Wu et al., 2018a). Therefore, the future research should focus on improving sampling techniques to minimize errors, enhance the representatives of samples, and reduce patient discomfort and anxiety.

### 2.2.3 Imaging Techniques

Accurate and timely imaging plays a critical role in lung cancer detection, staging, and monitoring (Paydar et al., 2012). Various imaging techniques developed over the years have improved diagnostic accuracy and guided treatment decisions (Liu et al., 2021). The following subsub-sections provide a comprehensive overview of the various imaging modalities and their advances for diagnosing lung cancer.

#### 2.2.3.1 Chest X-rays

X-rays was discovered by W. C. Roentgen in 1895 while working with a cathode-ray tube in a laboratory, and justified that ray could pass through human tissue, but

could not through bones or metal objects (Röntgen, 1896). A year later, with the advantages of different parts of the body absorbing varying degrees of X-ray (bone absorbs much radiation and appears white (Joarder and Crundwell, 2009) and soft tissue allows more X-rays to pass through them and shows up in shades of gray and appears black (Thrall, 2017)), Hall-Edwards applied x-ray for surgical operation (Ward, 1896)

The recent advances in X-rays and radioactivity resulted in compact, portable X-ray machines that produces images of chest bones, blood vessels, heart, airways, and lungs using electromagnetic waves and ionizing radiation (Chen et al., 2016). Specifically, since the lung tissue absorbs little radiation and will appear dark in the image, physicians use the chest x-rays (CXR) examination for pneumonia, fluid or air collection around the lungs, lung cancer, etc. This can be done by positioning the patient between the machine to obtain front and side views (Malik and Anees, 2022). The front view can be obtained through posterior-anterior (X-Ray beams hit the posterior part of the chest before the anterior part, and it gives a clear image) (Paydar et al., 2012) and anterior-posterior (the patient is standing with their back against the film) (Lahham et al., 2018) as shown in Figure.2.1.

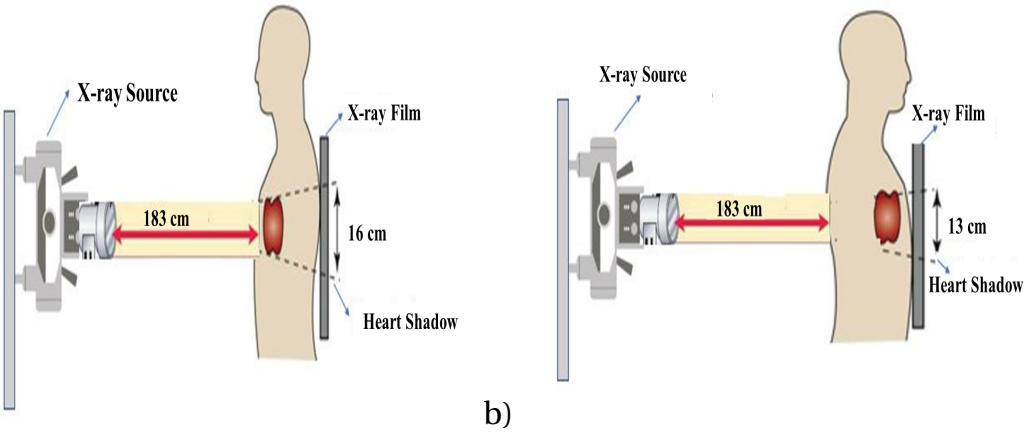


a) b)

Figure 2.1: *The different view of chest x-rays. a) posterior-anterior, and b) anterior-posterior.*

In general, some of the main advantages of CXR are it does not require special preparation, highly efficient, require simple equipment setup, inexpensive, and

have no side effects for patients as compared with others techniques (Liu et al., 2021). On the other hand, some of the disadvantages of the techniques are , it may not be detect early stage cancers, and blood clots in the lungs need further imaging studies to clarify the results (Matsubara et al., 2020).

#### 2.2.3.2 Computed Tomography

In the late 1960s, the first computed tomography (CT) scanner was invented, and by the early 1970s, the first CT scan on a patient was performed (PAPAIOANNOU and FRANCIS, 1965). The techniques of CT uses x-rays, ionizing radiation, and an electronic detector array to record a pattern of densities and created higher resolution images of specific parts of the tissue and organ (Bastarrika et al., 2005). These can be performed by rotating the x-ray beam around the patient within the scanner to allow multiple x-ray projections to gate a clear image, by combining traditional x-ray technology with computer processing (Bravin et al., 2007). CT produces two-dimensional cross-sectional images from the three-dimensional body (Sullivan et al., 2017).

The CT scan provides more detailed images than plain radiography, allowing them to see structures from different perspectives (Bastarrika et al., 2005). There has been recent research reporting that low-dose CT (LDCT) is effective in detecting lung cancer at an earlier stage and at a smaller scale (Sullivan et al., 2017). Based on the National Lung Screening Trial (NLST) results, LDCT screening reduced lung cancer-specific mortality in individuals at high risk of smoking by 20% when compared to chest radiographs (Tammemägi et al., 2019). The main limitation of CT examinations is ionizing radiation exposure to patients, requiring whole-body imaging, relatively expensive, and image interpretation requiring sophisticated mathematical algorithms (Lambert et al., 2021).

#### 2.2.3.3 Magnetic Resonance Imaging

The nuclear magnetic resonance (NMR) phenomenon was described in 1946 by Bloch and Purcell (Purcell et al., 1946). Following the introduction of wide-bar superconducting magnets by Lauterbur, the first clinical magnetic resonance images

(MRI) were produced in 1980 (Roughton, 1982). Recently, either cylindrical narrow tunnel or more open MRI machines are applied to capture image of patient by passing an electrical current through a massive coil (used to eliminate electrical resistance to bring it into a superconducting state) that results in 1.5 to 3.0 magnetic field density (Fischer et al., 2008).

These magnetic field densities were achieved by employing powerful magnets for the generation of a strong magnetic field to force protons in the body to align with the strong magnetic field (Grover et al., 2015). Besides, pulsing a radio frequency (RF) current to the patient, results the stimulation of protons that tend to spin out of equilibrium. After the removal of the RF field , the MRI sensors detect the energy released by protons as they realign with the magnetic field (Collins and Wang, 2011). The quantity of energy released and the time it takes for the protons to realign with the magnetic field vary depending on the environment and the chemical nature of the molecules. The duration of this return differs depending on the type of tissue (muscle, blood, fat, etc.) to which the protons are bonded (Schick, 2005). This can be received as a signal, and image is formed by analyzing the signal and return time. With these procedures, the ligaments, brain, nerves, spinal cord, as well as muscles, and tendons, are seen much more clearly (Atesok et al., 2018).

In general, some advantages of MRI include: providing higher tissue resolution, the capacity to visualize blood arteries without contrast agents, and non invasiveness and lack of radiation exposure (Gordillo et al., 2013). While the disadvantage is: the inability to perform the test when metal is present in the body, the long scan time, the difficulty in scanning claustrophobic patients, and the inability to obtain a signal from cortical bone and calcification (Mervak et al., 2019).

To summarize, the traditional lung cancer diagnostic methods, such as imaging techniques and tissue biopsy, often have limitations in terms of cost, invasiveness, and sensitivity (Mervak et al., 2019). The use of biosensors offers the possibility

of convenient, non-invasive, and sensitive detection of lung cancer biomarkers. Thus, the vast research have been underdevelopment on electrochemical, optical, and field-effect transistor biosensors for cancer diagnosis (Liu et al., 2018b). Specifically, these biosensors utilize various lung cancer biomarkers, such as microRNA, circulating tumor cells (CTCs), exosomes, and volatile organic compounds (VOCs) (Baghel et al., 2021). From all, the plasmonic biosensors, which are special kinds of optical sensors, have the potential to revolutionize lung cancer diagnosis and enable personalized treatment strategies. However, further research is needed to validate their clinical utility, optimize their performance, and determine their cost-effectiveness.

#### 2.2.3.4 Impact of Machine learning on Lung Cancer Diagnosis

Both classical and quantum machine learning have the potential to revolutionize lung cancer diagnosis by significantly enhancing the accuracy and effectiveness of the process. By training algorithms on large datasets of medical images, machine learning models can learn to detect patterns and abnormalities that may be indicative of lung cancer. Classical machine learning algorithms, are designed to continuously improve as they receive more data, leading to more accurate and reliable diagnoses over time. With the ability to analyze vast amounts of data in a short period, machine learning algorithms can assist radiologists in detecting early-stage lung cancer with high precision, even in complex cases. This technology has the potential to reduce false positives, minimize missed diagnoses, and enhance overall diagnostic accuracy. On the other hand, quantum machine learning has the potential to process and analyze vast amounts of data exponentially faster compared to classical methods (Steinkamp and Cook, 2021). With the ability to exploit quantum entanglement and superposition, quantum machine learning algorithms can accelerate the analysis of complex medical images and enhance the accuracy of lung cancer diagnosis. Moreover, the powerful computational capabilities of quantum computers can support more sophisticated modeling, enabling the development of highly accurate predictive models and treatment

plans (Yadavendra and Chand, 2020).

Moreover, the classical and quantum machine learning have the potential to significantly impact lung cancer telediagnosis. Classical machine learning algorithms can be used to analyze medical images and patient data remotely, aiding in the accurate diagnosis of lung cancer. These algorithms can assist healthcare providers in interpreting radiographic images, identifying suspicious lesions, making informed decisions regarding treatment plans, facilitate risk stratification, and prognosis prediction based on patient-specific characteristics (Azevedo et al., 2022). On the other hand, quantum algorithms can utilize the computational power of quantum computers to process large-scale data sets more rapidly, thereby accelerating the diagnostic process and reducing response times in remote consultations. However, the practical implementation of quantum machine learning in telediagnosis requires significant advancements in quantum hardware and expertise. Nevertheless, the combined impact of classical and quantum machine learning on lung cancer telediagnosis has the potential to improve access to specialized care, enhance diagnostic accuracy, and enable timely treatment decisions for patients regardless of their physical location (Wei et al., 2023).

## 2.3 Plasmonic Biosensors

Plasmonic biosensors are engineered periodic 2D optical instruments designed by arranging shiny metallic nanosurface (MNS) on the dielectric layer to replace the conventional bulky optical instrument with $10^4$ times thinner flat optical components (Kumela et al., 2023b). For quantitative measurements of analytes and information on molecular structures by concentrating, blocking, absorbing, and dispersing or guiding electromagnetic waves both on the surface and in space at normal and oblique incidence. Thus, in the following subsection the basic principles, classification, detection mechanism, with objective of revealing pros and cons of each plasmonic biosensor are discussed in detail.

### 2.3.1 Principles of Plasmonic Biosensor

Plasmons are collective oscillation of free electrons, resulted when a photon of incident light hits a shinny metallic surface or plasmonic NS at certain angle of incidence. Spectral control of the plasmon resonance is achieved by tuning particle shape, size, composition, and local environment, leading to novel biosensor applications. Those can be governed by classical, quantum mechanical, and hybrid models (Kumela et al., 2022a).

#### 2.3.1.1 Classical Model for Plasmonic Biosensor

Light is an electromagnetic wave (EMW) containing both oscillatory electric field (**E**(r,t)) and magnetic fields (**B**(r,t)) that fully expressed employing the magnitude and direction at every point in space (r). This can be expressed using Maxwell differential equations (Yeh and Shimabukuro, 2008);

$$\nabla.\mathbf{E} = 0, \tag{2.1a}$$

$$\nabla.\mathbf{B} = 0, \tag{2.1b}$$

$$\nabla \times \mathbf{E} = -\frac{\partial \mathbf{B}}{\partial t}, \tag{2.1c}$$

$$\nabla \times \mathbf{B} = \epsilon_0 \mu_0 \frac{\partial \mathbf{E}}{\partial t}. \tag{2.1d}$$

Where, $\epsilon_0$ is vacuum permittivity and $\mu_0$ vacuum permeability. These equations enable solutions for electric and magnetic fields that oscillate in space and time. Instead of attempting to solve for both simultaneously, we utilize these equations to derive an expression that imposes conditions on electric field without explicit dependence on magnetic field (Kumela et al., 2023b). Thus taking the curl of Eq.(2.1c) and the negative time derivative of Eq.(2.1d), we find

$$\nabla \times \nabla \times \mathbf{E} = -\frac{\partial}{\partial t}(\nabla \times \mathbf{B}), \tag{2.2a}$$

$$-\frac{\partial}{\partial t}(\nabla \times \mathbf{B}) = -\epsilon_0 \mu_0 \frac{\partial^2 \mathbf{E}}{\partial t^2}. \tag{2.2b}$$

Comparing both equations we see,

$$\nabla \times \nabla \times \mathbf{E} = -\epsilon_0 \mu_0 \frac{\partial^2 \mathbf{E}}{\partial t^2}. \tag{2.3}$$

Considering the general identity of vector calculus ($\nabla \times (\nabla \times \mathbf{E}) = \nabla.(\nabla.\mathbf{E}) - \nabla^2\mathbf{E}$) into Eq.(2.3) inline with Eq.(2.1a), we find

$$\nabla^2 \mathbf{E} - \epsilon_0 \mu_0 \frac{\partial^2 \mathbf{E}}{\partial t^2} = 0. \tag{2.4}$$

Eq.(2.4) is the wave equation in a vacuum, employing the time-dependent solution, the plane wave equation in vacuum is given by

$$\mathbf{E}(r,t) = \mathbf{E}_0 e^{i(kr-\omega t)} + \mathbf{E}_0^* e^{-i(kr-\omega t)}, \tag{2.5}$$

here, $r = x\hat{i} + y\hat{j} + z\hat{k}$ is position in three dimension (3D) with $\omega$ and $\mathbf{E}_0$ is frequency and amplitude of incident field respectively for, $k$ is the wave vector of the incident wave.

Eq.(2.5) represents position dependent field, from which the spatial distribution, intensity variations, and structures present in the field were investigated. Aiding in the understanding of its spatial features such as peaks, boundaries, or spatial relationships among different components. This information is valuable for fields like imaging, pattern recognition, and understanding the physical properties of the system under consideration. While, from a frequency-dependent field, we gain insights into the spectral composition, frequency components, and characteristic frequencies present in the field. Analysis of the frequency-dependent field helps identify resonant frequencies, frequency bands, or frequency shifts, providing information about the behavior and properties of the system. This information is valuable for areas such as signal processing, communication systems, and understanding the frequency response of the system (Wei et al., 2023). Thus, to convert a position-dependent field into a frequency-dependent field, the Fourier

transform, which expresses the field in terms of its frequency components were given in Eq.(A.1a).

On the other hand, for light-matter interaction, we can consider Maxwell's equations with the inclusion of terms related to charges and currents in the material. In the modified set of Maxwell's equations the divergence of magnetic field and curl of EMW remains the same with vacuum but the rest are written as follows (Fernandez-Corbaton et al., 2013):

$$\nabla.\mathbf{E} = D, \tag{2.6a}$$

$$\nabla \times \mathbf{B} = \mu J + \varepsilon\mu\frac{\partial \mathbf{E}}{\partial t}. \tag{2.6b}$$

Where, D=$\rho/\varepsilon$ is electric displacement vector, for $\rho$ and $\varepsilon$ are charge density, and dielectric permittivity, respectively. And J is the electric current density, $\mu$ is permeability of materials. Taking the same procedure dispensed in Eq.(2.2a) to Eq.(2.4) we find

$$\nabla^2\mathbf{E} = \frac{\rho}{\varepsilon} + \mu J + \mu\varepsilon\frac{\partial^2}{\partial t^2}\mathbf{E}. \tag{2.7}$$

The general solution of Eq.(2.7) yields the total electromagnetic field (EMF) resulting from light-matter interaction as follows:

$$\mathbf{E}_{Tot}(\omega, t) = \gamma\mathbf{E}(\omega, t). \tag{2.8}$$

In which $\gamma$ is decay rate of free electrons. Thus, the total electromagnetic field resulting from light-matter interaction is explicit into incident and output field as expressed in Eq.(A.3) (Kumela et al., 2022a).

$$\mathbf{E}_{Tot}(\omega, t) = \mathbf{E}_{in}(\omega, t) + \mathbf{E}_{out}(\omega, t). \tag{2.9}$$

Where, $\mathbf{E}_{in}(\omega, t)$ incident field given in Eq.(A.2a) and $\mathbf{E}_{out}(\omega, t)$ is output field explained in Eq.(A.3).

The strong or weak light-matter coupling results in the linear and nonlinear response of light-matter interactions that expressed by polarization, dielectric constant, extinction coefficient and refractive index. Liner response of light-matter interactions occurred when a single incident field produces a single photon as a result of a weak incident field and material properties that given by, (Hu et al., 2021)

$$\mathbf{P}^{L}(\omega,t) = \epsilon_0 \chi^{(1)} \mathbf{E}_{in}(\omega,t). \tag{2.10}$$

For $\chi^{(1)}$ is first order susceptibility. Besides, when the matter is pumped by an intense incident field more than a single photon is resulted in **i.e** nonlinear response of light (Nicoletti and Cavalleri, 2016).

$$\mathbf{P}^{NL}(\omega,t) = \epsilon_0 \chi^{(2)} \mathbf{E}^{2}_{in}(\omega,t) + \epsilon_0 \chi^{(3)} \mathbf{E}^{3}_{in}(\omega,t) + ...\epsilon_0 \chi^{(n)} \mathbf{E}^{n}_{in}(\omega,t) \tag{2.11}$$

Where, $\chi^{(2)}$, $\chi^{(3)}$, and $\chi^{(n)}$ are second, third, and n$^{th}$ order susceptibility respectively, that is used for frequency conversion processes.

Employing Eq.(2.10) and (2.11) the total polarization of light resulted from light-matter interaction gives, (Kauranen and Persoons, 1996).

$$\begin{aligned} \mathbf{P}(\omega,t) &= \mathbf{P}^{L}(\omega,t) + \mathbf{P}^{NL}(\omega,t), \\ &= \epsilon_0 \chi^{L} \mathbf{E}_{in}(\omega,t) + \epsilon_0 \chi^{NL} \mathbf{E}_{in}(\omega,t). \end{aligned} \tag{2.12}$$

Here, $\chi^{L}$ and $\chi^{NL}$ are linear and nonlinear susceptibility of matter respectively.

In addition, the collective outermost electronic motion (polarization) resulted from either weak or intense light-matter interaction, causes vibrating like a damped harmonic oscillator. This can be governed by the differential equation of motion ($-e\mathbf{E}(\omega,t) = m\frac{d^2\mathbf{P}}{dt^2} + m\gamma\frac{d\mathbf{P}}{dt} + K\mathbf{P}$), in which e is electron charge, m is mass of free electron, and K is is the spring constant (MacDonald, 1952). The goal of this model is to use Newton's second law to calculate electron motion, which can then be used to calculate the dipole moment, polarization, susceptibility, and dielectric

constant (Zheng et al., 2021). Thus, using the second derivation of the polarization of light given in Eq.(2.12), the collective movement of free electrons inside the metal surface is described by considering incident field as macroscopic applied force, which is dependent on conductivity $(\sigma)$, size, shape, and decay rate of free electrons ($\gamma_{ab} = \sum_i \gamma_i$) as (Zheng et al., 2021),

$$\begin{aligned} \epsilon_0 \omega_p^2 \mathbf{E}_{in}(\omega, t) &= \ddot{\mathbf{P}}(\omega, t) + \gamma_{ab} \dot{\mathbf{P}} + \omega_0^2 \mathbf{P}(\omega, t), \\ &= \left(\omega_0^2 - \omega^2 - i\gamma_{ab}\omega\right) \epsilon_0 \chi^n \mu \mathbf{E}_{in}(\omega, t). \end{aligned} \tag{2.13}$$

Where,

$$\omega_p = \sqrt{\frac{\Gamma q^2}{\epsilon_0 m_e}}, \tag{2.14}$$

is plasma frequency, for, $m_e$ is mass of electron, q is charge and $\Gamma = \frac{\rho N_a}{M} n_e$ in which, $N_a$ is Avogadro number, M is atomic mass of particle and $n_e$ is number of free electron.

Applying simplification and rearrangement on Eq.(2.13), the nonlinear-susceptibility of material gives,

$$\chi^{NL}(\omega) = \frac{\omega_p^2}{(1+\mu)(\omega_0^2 - \omega^2 - i\gamma_{ab}\omega)}, \tag{2.15}$$

for weak interaction or linear response, $\mu \approx 0$ since the rate decay of free electron is proportional to the incident field and Eq.(2.15) reduced to,

$$\chi^{L}(\omega) = \frac{\omega_p^2}{(\omega_0^2 - \omega^2 - i\gamma_{ab}\omega)}. \tag{2.16}$$

Using Eqs.(2.15) and (2.16) into Eq.(2.10) and (2.11) the linear and nonlinear

polarization, gives (Kumela et al., 2022a),

$$\mathbf{P}^{L}(\omega,t) = \left[\frac{\omega_p^2}{(\omega_0^2-\omega^2-i\gamma_{ab}\omega)}\right]E_0 cos(\omega t), \tag{2.17a}$$

$$\mathbf{P}^{NL}(\omega,t) = \left[\frac{\omega_p^2}{(1+\mu)(\omega_0^2-\omega^2-i\gamma_{ab}\omega)}\right]E_0 cos(\omega t). \tag{2.17b}$$

Where,

$$cos(\omega t) = \frac{e^{i(kr-\omega t)}+e^{-i(kt-\omega t)}}{2}. \tag{2.18}$$

Further, the dielectric function of materials is derived using Maxwell's relation which connects the electric displacement field (D) with material properties as,

$$\mathbf{D}(\omega,t) = \epsilon_0\mathbf{E}_{in}(\omega,t) + \mathbf{P}(\omega,t), \tag{2.19}$$

from this relation we can establish

$$\varepsilon(\omega) = 1+\chi. \tag{2.20}$$

Using Eq.(2.15) to Eq.(2.17b) into Eq.(2.20) in line with $\varepsilon = \varepsilon^{'} + \varepsilon^{"}$ for $\varepsilon^{'}$ is real part and $\varepsilon^{"}$ is imaginary part, the linear and nonlinear dielectric function respectively defined as,

$$\varepsilon^{L}(\omega) = 1 + \frac{\omega_p^2}{\omega_0^2+i\gamma_{ab}\omega} + i\frac{\omega_p^2\gamma_{ab}\omega}{(\omega_0^2-\omega^2-i\gamma_{ab}\omega)}, \tag{2.21}$$

and

$$\varepsilon^{NL}(\omega) = 1 + \frac{\omega_p^2}{(1+\mu)\left(\omega_0^2+i\gamma_{ab}\omega\right)} + i\frac{\omega_p^2\gamma_{ab}\omega}{(1+\mu)(\omega_0^2-\omega^2-i\gamma_{ab}\omega)}. \tag{2.22}$$

To gain valuable information about the optical properties of material, the reflectivity of a material is obtained from its dielectric function, which describes its response to an electromagnetic wave. The dielectric function consists of real and

imaginary components, representing the material's ability to polarize and absorb light, respectively. By using the dielectric function, the complex refractive index of the material, which determines the behavior of light at the material interface can be calculated. Employing this relation, the reflectivity of light inside any proposed sensor region takes the form,

$$R_{ij} = \frac{\varepsilon_j k_i - \varepsilon_j k_i}{\varepsilon_j k_i - \varepsilon_j k_i}. \tag{2.23}$$

Where i,j represents different material layers and propagation strength.

Moreover, applying the Clausius-Mossotti relation developed by Ottaviano-Fabrizio Mossotti and Rudolf Clausis, the relationship between the dielectric constant of two different media were investigated (Hannay, 1983). To analyze the polarization density of (i) ionic polarizability resulted from displacement between positive and negative ions of materials (MacDonald, 1952), (ii) electronic polarization raises from the displacement of positive nuclei and negative electrons inside the same atoms (Nicoletti and Cavalleri, 2016), and (iii) the presence of dipole moment of complex ions or molecules. Using this relation, one can express conductivity and the refractive index of any material at a much higher density (Giannini et al., 2010). So, the loss of free electrons resulted from light-matter interaction by transforming into heat called absorption cross-section ($\delta_{abs}$) or redirected to a different direction called scattering cross section ($\delta_{sca}$) are defined in terms of the dielectric function of materials (Eq.(2.21) and (2.22)) respectively, by (Kumela et al., 2022a),

$$\delta^{L}_{abs} = \frac{16\pi k^4}{6\pi} \Re \left[ \frac{\varepsilon^{L}_{M} - \varepsilon^{L}_{D}}{\varepsilon^{L}_{M} + 2\varepsilon^{L}_{D}} \right]^2, \tag{2.24a}$$

$$\delta^{NL}_{abs} = \frac{16\pi k^4}{6\pi} \Re \left[ \frac{\varepsilon^{NL}_{M} - \varepsilon^{NL}_{D}}{\varepsilon^{NL}_{M} + 2\varepsilon^{NL}_{D}} \right]^2, \tag{2.24b}$$

and

$$\delta_{sca}^{NL} = \frac{16\pi^2 k}{r^4} \Im \left[ \frac{\varepsilon_M^{NL} - \varepsilon_D^{NL}}{\varepsilon_M^{NL} + 2\varepsilon_D^{NL}} \right]^2, \tag{2.25a}$$

$$\delta_{sca}^{L} = \frac{16\pi^2 k}{r^4} \Im \left[ \frac{\varepsilon_M^{L} - \varepsilon_D^{L}}{\varepsilon_M^{L} + 2\varepsilon_D^{L}} \right]^2. \tag{2.25b}$$

$$\tag{2.25c}$$

Here, $\Re$ real, and $\Im$ imaginary part of polarizability. And r is the radius of materials, $\varepsilon_M$ is the linear or nonlinear dielectric function of the metallic surface, and $\varepsilon_D$ is the dielectric function of dielectric materials. With this, the total radiant flux area (extinction cross-section) is defined by a superposition of absorption and scattering cross-section (Giannini et al., 2010),

$$\delta_{exc} = \delta_{sca} + \delta_{abs}. \tag{2.26}$$

The sensitivity of the optical sensor depends on the efficiency of propagation light. That defined as the ratio of absorption cross-section to extinction cross-section and scattering to extinction cross-section. Thus, mathematically defined by (Giannini et al., 2010),

$$\eta_{sca}^{L} = \frac{\delta_{sca}^{L}}{\delta_{exc}^{L}}, \rightarrow \eta_{sca}^{NL} = \frac{\delta_{sca}^{NL}}{\delta_{exc}^{NL}}, \tag{2.27a}$$

$$\eta_{abs}^{L} = \frac{\delta_{abs}^{L}}{\delta_{exc}^{L}}, \rightarrow \eta_{abs}^{NL} = \frac{\delta_{abs}^{NL}}{\delta_{exc}^{NL}}, \tag{2.27b}$$

$$\eta_{ext}^{L} = \eta_{sca}^{L} + \eta_{abs}^{L}, \rightarrow \eta_{ext}^{NL} = \eta_{sca}^{NL} + \eta_{abs}^{NL}. \tag{2.27c}$$

Where, $\eta_{sca}$, $\eta_{abs}$ and $\eta_{ext}$ are scattering efficiency, absorption efficiency and extinction efficiency respectively.

#### 2.3.1.2 Quantum approach to model plasmonic biosensor

One of the most important topics in time-dependent quantum mechanics is the description of spectroscopy interms of interaction of electromagnetic radiation with matter (Hofmann et al., 2012). Quantum mechanically, we treat spectroscopy

as a perturbation induced by the light which acts to couple quantum states of the charged particles in the matter and their interactions are expressed by quantization scheme (both photons and matter particles can be created and annihilated) (Ruggenthaler et al., 2018).

The quantum field model is explain by quantized light-matter interaction, with three boson fields representing the electromagnetic, polarization, and damping fields (Hofmann et al., 2012). The quantum theory of light-matter interactions in semiconductors and dielectrics has been approached from two different angles. One team looked at the interaction between electrons and lattices and showed how it results in the dampening of excited electronic states. Another team looked at the interaction between radiation and electrons and showed how it results in radiation field dispersion (Kira and Koch, 2011). Thus expressed using quantization scheme, Edwin Jaynes, and Fred Cumming and Quantum input-output model (QIM)(Iurov and Gumbs, 2013; Scott, 2019).

The light-matter interaction in quantum mechanical expression is the essential physical process used in many experiments including; trapping of atoms, spectroscopy, atomic interferometry, and collision physics (Wieman et al., 1999). To design this the laser-atom interaction with time is often required. The QED model treats the atom within the quantized form of an electromagnetic field to unravel the equation of motion for the expression of radiative and nonradiative decay of the atom (Schuurmans and Van Dijk, 1984). These systems did not use extensively since solving the laser-atom interaction is time-intensive, complex, and vulnerable to mistakes. However, models that treat both the atom and field quantum mechanically can describe the relief terms more rigorously when the system is complex with many substrates involved within the interaction (Rice and Carmichael, 1994).

On the other hand, the Edwin Jaynes and Fred Cummings model developed in 1963 clarify the interaction of atoms with an electromagnetic field in the form of

quantized energy levels using the ladder operator (Jaynes and Cummings, 1963). Several corrections have been made to extend the original model to express multiple atoms interacting with the same field. For example, the non-linear nature of energy levels by direct spectroscopic the observation was developed in the Dicke model or the Tavis-Cummings model (Retzker et al., 2007). To express the quantum superposition state on a macroscopic scale using a Hamiltonian of the quantized radiation field by (Kumela et al., 2022a)

$$\hat{H} = \hat{H}_F + \hat{H}_M + \hat{H}_{Int}. \tag{2.28}$$

Here, $\hat{H}_F, \hat{H}_M, \hat{H}_{Int}$ are field, matter and light-matter interaction respectively.

With the dynamics of those models, the theoretical demonstration of coupling nanoscale materials or samples with electromagnetic fields was potentially suited to a model plasmonic biosensors for several medical applications (Jain et al., 2008). In addition, the quantum input-output theory developed by Gardiner and Collet presents the formalism that accounts for the interaction of an atom or a cavity with traveling pulses of a quantized field (Combes et al., 2017). Using Markovian coupling of the stationary system to the input and output fields, the non-dispersive asymptotic propagation of the pulses before and after the interaction was used to drive the Hamiltonian of light-matter interaction (Alicki, 1989). With this, the quantum Langevin equations were analyzed to express the large-scale quantum networks that fully support the quantum communication protocol over a certain distance (Ford et al., 1988; Childress et al., 2006).

Thus, the dynamical equations are given by Heisenberg-Langevin equations of the evolution of atomic operators applying quantized systems as reported by (Madureira et al., 1998),

$$\frac{d}{dt}\hat{a} = -\frac{i}{\hbar}[\hat{a}, \hat{H}] - \frac{\kappa}{2}\hat{a}. \tag{2.29}$$

Here, $\kappa$ is the cavity damping constant and $\hat{a}$ is bosonic operator.

Eq.(2.29), represents, the Heisenberg-Langevin equations of light-matter inter-

action that provides the valuable information about dynamics and fluctuations of the system (Jiang et al., 2023). By taking the Hamiltonian of the system into account, the dissipation caused by the environment, and the fluctuations arising from the quantum nature of the system can be analyzed (Blasone et al., 2003). These phenomena provides the valuable information for sensor applications by aiding in sensitivity analysis, noise characterization, signal processing, understanding quantum states, and accounting for environmental interactions (Wang et al., 2023). This knowledge can guide the design, operation, and optimization of sensors for improved performance and reliability in a wide range of applications (Yu et al., 2021).

#### 2.3.1.3 Semi-classical approach

The time-dependent dynamics of matter-laser field interaction is usually described within the so-called quantum-classical hybrid approach or semi-classical approximation (Kantner et al., 2018). In this approximation, the laser field may be considered equivalent to a classical electromagnetic field and the dynamics of the atomic system is treated fully quantum mechanically by means of the time-dependent Schrodinger equation (Tal-Ezer and Kosloff, 1984). The laser-matter interaction is often simplified by imposing the so-called dipole approximation. The dipole approximation is a type of long-wavelength approximation (LWA) in that, it is likely to be valid whenever the laser wavelength is much larger than the relevant atomic dimensions (Ruggenthaler et al., 2010).

### 2.3.2 Classification of Plasmonic Biosensor

Plasmonic biosensors were grouped into: those that use thin metallic films and individual inorganic plasmon resonant nanostructures (Hill, 2015). Within each class, there are many sensing modalities developed to provide extraordinary capabilities of high sensitivity, specificity, and real-time monitoring of biological analytes in the field of cancer diagnosis (Ouyang et al., 2016). Over the years, new sensing mechanism have been developed (Xu et al., 2012; Cetin et al., 2014; Chang et al., 2018). In the proceeding subsections, we review different classifications,

experimental and theoretical designs, sensor and detection mechanisms, and limitations and future perspectives of recent plasmonic biosensors in detail.

#### 2.3.2.1 Surface-enhanced Raman spectroscopy Biosensor

The interaction of photons with molecules resulted in either elastic (Rayleigh), or inelastic (Raman) scattering (Fazio et al., 2017). As a result of this interaction, photons may gain energy from a molecule that undergoes the opposite process (anti-Stokes Raman scattering) or lose energy in favor of a molecule that advances from the ground state to its first excited vibrational state (Stokes Raman scattering) (Xu et al., 2012). And the in-elastically scattered photons contain information on the vibrational modes of the molecules they interact with (OMODELE et al., 2023), this was dispensed in Figure.2.2. For the first time, these phenomena were observed in 1974 by Fleischmann who reported an unexpectedly large Raman signal from pyridine adsorbed on a roughened silver electrode (Creighton et al., 1979). Following, Jeanmaire and van Duyne, and Albrecht and Creighton confirmed Fleishman's findings and hypothesized that, this phenomenon originated from strong electrochemical electric fields at the metal surface (Jeanmaire) or by the formation of a molecule–metal complex (Albrecht). Lately, Moskovits proposed that the large signal was originated by the optical excitation of collective oscillations of the electrons in the metallic nanosized features at the surface (Daniels and Chumanov, 2005).

Recently, Xu et al. (2012) designed graphene-mediated SERS substrate to result electromagnetic "hot" spots signals. These signals are free from various metal-molecule interactions and being more stable against photo-induced damage that have interesting advantages over normal SERS. Thus, their work enable direct, real time and reliable detection of trace amounts of analytes in various systems, with high efficiency and universality of analyses substrates. In addition, (Polavarapu et al., 2014) with high motivation on recent advances in conductive ink pens for electronic devices on paper, they presented a simple"pen-on-paper" based SERS substrates. The proposed "pen-on-paper" write SERS arrays uses plasmonic inks

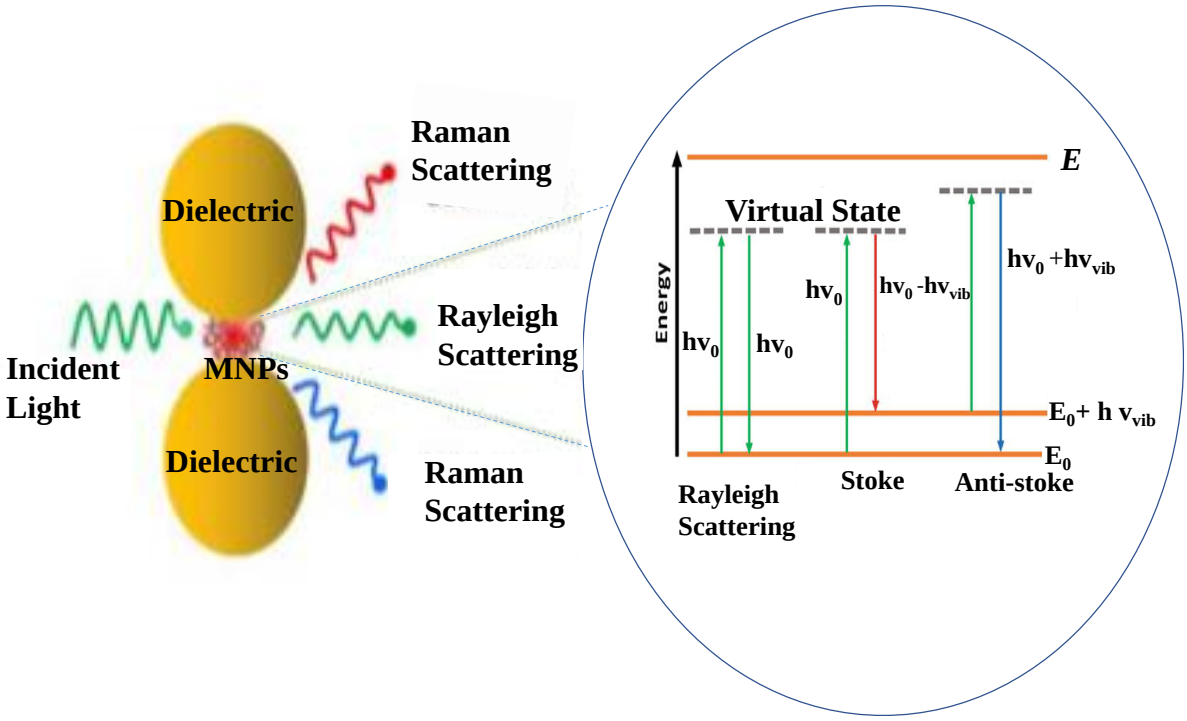


Figure 2.2: *Schematic diagram of surface enhance Raman spectroscopy.*

( made of silver nanospheres, gold nanospheres, and gold nanorods), that result various excitation wavelengths. There method offers cost effective, portable, and efficient SERS substrates at the point of care. Further, (Koh et al., 2021) reported a wearable surface-enhanced Raman scattering (SERS) sensor. That constituted of SERS active layer, dermal protecting layer, silk fibroin protein film layer, plasmonic silver nanowire, and transparent dermal protecting layer. Their work reports, the feasibility of the proposed wearable SERS biosensor by applying for drug detection on the human cadaver skin.

Indeed, SERS shows a broad range of advantages: (i) possible unique fingerprint signature of the analyte causing high selectivity (Polavarapu et al., 2014), (ii) easy sample preparation method (OMODELE et al., 2023), (iii) no signal interference from the analyte medium, which is usually water-based, (iv) single-molecule detection (Koh et al., 2021), (v) potential for multiplexed sensing with a single laser beam, (vi) high throughput, and (vii) POC applicability by using commercially available portable Raman probes (Polavarapu et al., 2014).

#### 2.3.2.2 Surface plasmon resonance biosensor

The interaction of incident photons at a certain angle of incidence with shiny MNPs (Ag, Au, Al, etc) on a metallic surface (dielectric materials) resulted in, the collective oscillations of free electron in parallel direction to the metallic surface called surface plasmon (Si et al., 2021; Li et al., 2022) as seen in Figure.2.3. On the other hand, the interaction of resulted surface plasmons with the biological sample generates an electric field (in the range of 100 to 600 nm) which is different from bare (without biological sample) (Challis, 2005). This phenomenon results a surface plasmon resonance biosensor (SPRB). The advancement in standard components of SPRB such as light source, detector, coupling components (grating, prism, optical fiber and wave-guide) and imaging optical system leads to use SPRB in applications ranging from environmental protection to medical services (Yan et al., 2020; Pandey et al., 2020).

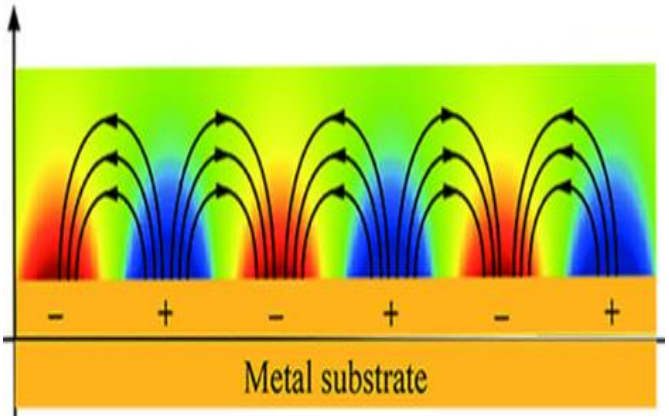


Figure 2.3: Arrangement of free electron in thin metallic sheet (surface plasmon resonance) adopted from Chen et al. (2020)

Thus the first SPRB with the components of light, gratings, and dielectric materials was introduced in 1902 by R.M. Wood, that applied to observe patterns of unusual dark and light bands in reflected light Wood (1902). Following, the theoretical formulation of MNPs spectroscopy in dielectric was given by J.C. Maxwell Garnett in 1904 Lamb (1904). In addition, the theoretical conclusion of surface plasmons supported by the network was given in 1941 by Fano (1941). Further, the excitation of surface waves on the metal-film surface on the other side of a prism

with attenuated total reflection (ATR) techniques was simultaneously proved by Otto (1968); Kretschmann and Raether (1968). These allow light to be confined below the diffraction limit and open up sub-wavelength photonic device integration.

Recently, Cetin et al. (2014) fabricated the compact optoelectronic sensor with a 60 g and 7.5 cm tall, for high-throughput screening of biomolecular interactions. By employing plasmonic micro-arrays coupled with a lens-free computational imaging system, to record the diffraction patterns of plasmonic nanostructures under uniform illumination by a single-light emitting diode tuned to the plasmonic mode of the nanoapertures. The fabricated label-free biosensor was applied for the quantitative detection of mono and bilayers protein in the thickness of 3 nm. Following, Liu et al. (2015) reported light weight fiber optics SPRB made up of light-guiding silica capillary coated with 50 nm gold film that linked with easily removable smart phone case. In this platform the phone case is used as light source (LED flash) and detector (phone camera), to record light intensity of different concentration of antibody binding in every 0.5 second. However, the phone case and SPRB connector need more sophisticated android application and hardware.

Ouyang et al. (2016) designed SPRB using silicon nanosheet and two-dimensional transition metal dichalcogenides. Their configuration was governed by Fresnel equations and transfer matrix method in the visible and near infrared wavelength range. From reflectivity, sensitivity, and full width at half maximum (FWHM) of SPR curve obtained, they reveal much better performance than that of the conventional sensing scheme. However, the scheme they develop was difficult to perform experimentally. Thus to configure the relative merits of one configuration over the other Vasudevan Pillai Radha et al. (2021) proposed multi-layer metallic surface (Ag, Al, Au and Cu) employing N-layer matrix formalism. Their work reveal the use of Al/Cu/Al/Cu configuration provides extra ordinary (1433.82/RIU) figure of merit (FOM) for detecting analytes with only refractive index in the range of 1.350

to 1.414.

In general, SPRB detect alterations in the refractive index to assess molecules bind to a metal surface with rapid and real-time evaluation, excellent selectivity, and reproducibile response (Yu et al., 2019). Despite these advances, some limitations of SPRB are (i) anything that alters the refractive index at the sensing surface will interfere with the analysis including nonhomogenous (complex) sample matrices, and nonspecific binding interactions (Li et al., 2019), (ii) the ligand may not maintain its native configuration upon immobilization on the sensor chip surface (Puiu and Bala, 2016), and (iii) limited sensor area, leading to a diminished capacity.

## 2.4 Quantum Mechanical Approach for Lung Cancer Telemedicine

Quantum mechanics, with its principles of superposition and entanglement, offers the potential to dramatically improve the accuracy and efficiency of lung cancer diagnosis and treatment in remote settings (Sergi, 2019). By harnessing the computational power of quantum computers, this approach can analyze large and complex datasets with lightning speed, enabling faster and more precise diagnosis of lung cancer (Mohr et al., 2019). Quantum algorithms can detect subtle patterns and anomalies in medical images, enhancing early detection rates and enabling personalized treatment plans (How and Cheah, 2023). Additionally, the properties of quantum mechanics can provide robust security and privacy measures for telemedicine interactions, protecting sensitive patient information. While the practical implementation of this approach is still evolving, it holds great promise for revolutionizing lung cancer telemedicine by expanding access to specialized care, improving diagnostic accuracy, and ultimately saving lives. These can be done employing two inter-going quantum phenomena called quantum teleportation's and the Bell measurement (Pirandola et al., 2015; Cacciapuoti et al., 2020).

### 2.4.1 Bell Measurement for Lung cancer Telemedicine

Bell measurement is a crucial technique applied in quantum teleportation for lung cancer telemedicine (Das et al., 2023). In this context, quantum teleportation involves transmitting the quantum state of a lung cancer patient's cells to a distant healthcare facility for analysis and diagnosis (Tarasov et al., 2020). Bell measurement allows us to measure the entanglement between two distant particles, known as qubits, and extract useful information from them (Vyshnevyy et al., 2013). In lung cancer telemedicine, this measurement enables the transfer of the patient's quantum state to the receiving facility without physically transporting the cells (Luo et al., 2021). By using Bell measurement, healthcare professionals can accurately analyze the patient's cells remotely, leading to timely and efficient diagnosis and treatment decisions (Mohr et al., 2019).

While, there are also some negative impacts worth considering. One significant concern relates to the complexity and high cost associated with implementing and maintaining quantum systems capable of performing Bell measurements (Córcoles et al., 2019). The infrastructure required for quantum teleportation is currently limited and expensive, making it challenging to establish widespread adoption in healthcare facilities (Córcoles et al., 2019). In addition, the need for specialized expertise in quantum physics and quantum computing could hinder the accessibility of this technology to healthcare professionals (Aithal, 2023). The risk of errors and technical difficulties in the quantum teleportation process could also lead to inaccuracies in the diagnosis and treatment decisions (Awan et al., 2022). Additionally, ensuring privacy and security during the transmission of sensitive patient data through quantum channels may raise concerns about data protection and encryption vulnerabilities (Sun et al., 2019). Consideration of these challenges and the continuous development of quantum technologies are vital for addressing the potential negative impacts and enhancing the applicability of Bell measurement in lung cancer telemedicine.

### 2.4.2 Impact of Quantum teleportation on Lung Cancer Telemedicine

Quantum teleportation is a concept in quantum physics that involves the transfer of quantum information from one location to another without physically moving the particles based on the principles of entanglement and superposition (Furusawa and Van Loock, 2011). In telemedicine, the transmission of medical information, such as patient data, medical images, and test results, is crucial for accurate diagnosis and treatment decisions (Haleem et al., 2021). Quantum teleportation offers a way to securely and efficiently transfer this information between remote locations. By creating an entangled pair of quantum particles, such as photons, with one particle remaining at the sending location and the other sent to the receiving location. The sender then performs a measurement on the entangled particle at their location, which collapses the state of the particle at the receiving end, effectively teleporting the information about the original quantum state (Singh et al., 2021; Cacciapuoti et al., 2020).

In the context of telemedicine, quantum teleportation can be utilized to transmit medical data with unprecedented security and accuracy. By encoding the patient's medical information into quantum states and teleporting it to the receiving end, quantum teleportation ensures that the data remains intact and cannot be intercepted or tampered with (Shams et al., 2023). This can greatly enhance privacy and data security, which are critical aspects of telemedicine. The potential benefits of applying quantum teleportation to telemedicine include real-time sharing of high-resolution medical images for diagnosis, remote consultations with specialists, and secure transmission of patient data for analysis and treatment planning (Sergi, 2019). While the practical implementation of quantum teleportation in telemedicine is still in early stages of research, it holds promise for advancing the efficiency, accuracy, and security of medical data transmission in telemedicine settings (How and Cheah, 2023).

While the concept of quantum teleportation shows promise for applications

in telemedication, there are several limitations that currently hinder its practical implementation:

- Fragility of quantum states: Quantum states are delicate and susceptible to noise and decoherence caused by interactions with the environment. This makes it challenging to maintain the integrity and fidelity of quantum states during the teleportation process, especially over long distances or in the presence of interference (Fröwis et al., 2018).

- Technical requirements: Implementing quantum teleportation requires advanced and sophisticated quantum systems, such as entangled particles and precise measurement setups. These requirements pose significant challenges in terms of hardware, scalability, and resource-demanding infrastructure, making it difficult to deploy quantum telemedicine systems on a large scale (Cacciapuoti et al., 2020).

- Limited distance and reliability: The transmission of quantum states through quantum teleportation is subject to distance limitations and signal degradation. Currently, the distance over which quantum teleportation can be achieved reliably is not sufficient for widespread telemedicine applications (Pirandola et al., 2015).

- Complex setup and expertise: Quantum teleportation requires specialized knowledge and expertise in quantum physics and quantum information theory. The design, implementation, and operation of a functional quantum telemedicine system require highly skilled professionals. The limited availability of such experts restricts the widespread adoption of quantum teleportation in telemedicine (Cacciapuoti et al., 2020).

- Integration with existing infrastructure: Implementing quantum teleportation in telemedicine would require integrating it seamlessly into existing telecommunication networks and healthcare systems(Gupta et al., 2023).

# 3

# Materials and Methods

In this chapter, materials and methods of the dissertation are peresented in two sections. The first section describes, the detail instruments, biological analyits, and lists of software's used to carry out this research. In the second section, the detail analysis of modeling and optimization scheme of optoplasmonic biosensors for extraction and interpretation of biosignals, and QML models for biosignal processing and LITT estimation and teleportation of biosignals and LITT via fiber optics cable is dispensed.

## 3.1 Materials

For optimizations of the proposed plasmonic biosensor, we used some experimental results of the optical properties of Ag, Al, Au, and $Fe_2O_3$ NS from a secondary source (Ali et al., 2023; Wu et al., 2018b; Moosmüller et al., 2021). In addition, the refractive index of different lung cancer biomarkers such as: CL15, A549, HT-29, EGFR, CK19, Calu-1, A427, and 95D were applied for simulation work (Liu et al., 2018a; Chiu et al., 2018; Zhang et al., 2022; Liou et al., 2014; Cao et al., 2021). From the VirtualLabFusion software (Yang et al., 2023), we used; three-level laser light of 1500 nm (Huang et al., 2017), gadolinium gallium garnet (GGG) prism (Matiatou et al., 2021), $90^o$ prism, fiber optics cable with multimode silica core (df c = 40 $\mu$m), and plastic cladding (dc = 48 $\mu$m) (Bourdine et al., 2018), matchzender intrfrometer, Homodyne detector, beam splitter, beam combiner, mirror, and endoscopy (Kumela et al., 2023b). Further, we used several open access softwares like; i)

FDTD Lumerical to design different shapes, sizes, and properties of Nobel MNPs interaction with laser light (McCoy et al., 2021), ii) CST Studio to design, analyze, and optimize electromagnetic components of systems (Budania et al., 2020), iii) Matlab 2022a to plot the mathematical result for analyzing sensor performance and to investigate quantum features of SPP (Khulbe, 2023), iv) Phyton with IBM packages to build the quantum circuit (Neha et al., 2023), for illustration of the teleportation of biological signals and dose of LITT.

## 3.2 Methods

### 3.2.1 Classical Method to Model Plasmonic Biosensor

The transitional and noble MNPs are found in various phases and have different properties depending on size, shape, and pumping mode (Gangareddy et al., 2018). In particular, to perform biological measurements using those materials, confirmation of size, shape, and optical properties of MNPs has been suggested. Since, toxicity is highly dependent on those parameters. Notably, considering the crystallinity and aggregation of metal oxide, the $\alpha$-type $Fe_2O_3$ precipitation has been chosen, and Al, Au, and Ag NS with a size range of 20 to 80 nm are considered to design bio-compatible plasmonic materials for improvement of the light absorption ability. In addition, under biomolecules, the concentration, shape, size, sequence, surface charge, surface charge hydrophobicity, H, and $\pi$ bond type are considered (Sakulkhu et al., 2015). Under environmental media conditions, PH, ionic strength, polarity, temperature, string, and viscosity are determined (McClements and Gumus, 2016) to construct biosensor model in Figure.3.1.

Figure.3.1 depicted the optical layout of the proposed optoplasmonic biosensors. Where, the first layer of the sensor region is a gadolinium gallium garnet (GGG) prism selected for its excellent reflectivity (Motogaito et al., 2015). The second layer is silver nanosurface (Ag NS), considered for its sharper resonance peak, less broad SPR curve, small optical damping, and no interband transfer at visible light frequency. The third layer ($Fe_2O_3$) is used as a sensing medium for its

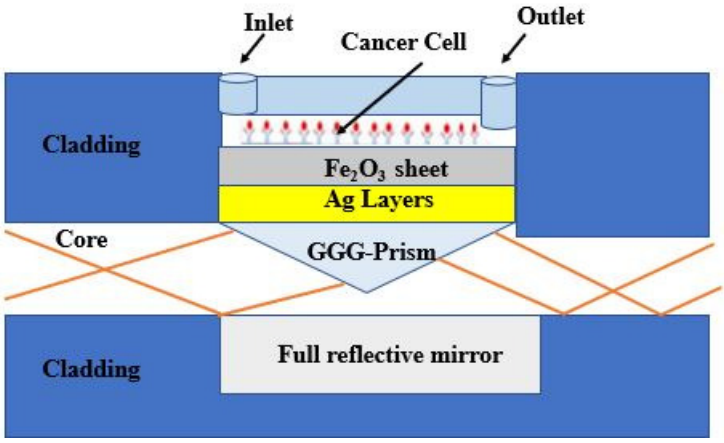


Figure 3.1: *Optical layout of the proposed plasmonic biosensor.*

outstanding properties of high surface area and biocompatability (Güneş et al., 2022). The fourth layer consists of the biomolecule composed of different lung cancer cells (Pietzner et al., 2022), this arrengment forms the plasmonic biosensor.

The working principles of proposed plasmonic biosensor follows, the biosensor consists of a metallic surface coated with specific biomolecules that can selectively bind to lung cancer biomarkers present in a patient's breath or sputum sample. When this sample is introduced to the biosensor, the target biomarkers bind to the biomolecular layer, causing a change in the LSPR characteristics. The interaction between the biomarkers and the plasmons results in a shift in the resonance wavelength or intensity of the reflected or transmitted light. This change is detected remotely and can be transmitted to a diagnostic center for analysis. By monitoring these changes in real-time, the plasmonic biosensor enables the rapid and non-invasive detection of lung cancer biomarkers, facilitating early diagnosis and timely treatment initiation for improved patient outcomes in telediagnosis scenarios. To achieve the simulation result, we applied both classical and quantum mechanical approaches.

#### 3.2.1.1 Modeling and Optimization of the Optical Properties of Plasmonic Biosensor

To model the properties of SPP classically, we consider Maxwell equations and Drude-Lorentz models following the same procedures dispensed in Eq.(2.11) to (2.22). Then, the intensity, absorption cross-section, scattering cross-section, extinction cross section and the efficiency of proposed optical layout were calculated. Since, those parameters are tools to measure capacity of any given sensor. So, the collective oscillation of electric field resulting from light-matter interaction is calculated following the same procedure dispensed in Eq.(2.6a) to (2.8) as,

$$\mathbf{E}_{SPP}(\omega,t) = (1+\xi)\mathbf{E}_{in}(\omega,t). \tag{3.1}$$

In which, $\xi$ is relative permittivity, that given by a summation of permittivity of metal and dielectric ($\varepsilon_r(\omega) = \varepsilon_m(\omega) + \varepsilon_d(\omega)$), and each permittivity is given as a summation of the real and imaginary part ($\varepsilon_{i=d,m,A}(\omega) = \varepsilon_i^{'}(\omega) + j\varepsilon_i^{''}(\omega)$). Where, $\omega$ is the frequency of incident light and the subscript d, m, and A represent; the permittivity of metal, dielectric materials, and biomolecule respectively, with j is an imaginary number. So, the relative permittivity of optoplasmonic surface on account of Eq.(2.21) and (2.22) gives,

$$\varepsilon_r(\omega) = \sum_{i=d,m,A}\left[\varepsilon_\infty^i - \frac{\Omega_i^2}{\omega_i^{*2} + i\gamma_i\omega_i} + j\frac{\Omega_i^2(\gamma_i\omega_i)}{(\omega_i^{*2} - \omega_i^2 - i\gamma_i\omega_i)}\right]. \tag{3.2}$$

Where $\Omega$, $\omega^*$, and $\gamma$ represent the plasma frequency, resonant frequency, and damping factor, respectively.

Coupling of the incident electromagnetic field with the sensor region is expressed by mass-dielectric polarization (**P**) using,

$$\mathbf{P} = \chi^{(1)}\mathbf{E}_{SPP}(\omega,t) + \chi^{(2)}\mathbf{E}_{SPP}^{(2)}(\omega,t) + \chi^{(3)}\mathbf{E}_{SPP}^{(3)}(\omega,t) + ...\chi^{(n)}\mathbf{E}_{SPP}^{(n)}(\omega,t). \tag{3.3}$$

For, $\chi^{(1)}, \chi^{(2)}, \chi^{(3)}$ and $\chi^{(n)}$ are linear, second order, third order and n$^{th}$ order suscep-

tibility respectively, that vary with the electronic structure of considered materials. Thus, the second-order susceptibility is diverged ($\chi^{(2)} = 0$) for optically isotropic material (Sohail and Ashiq, 2023), and depending on anharmonic terms of the polarization of bound electron, we have ignored the higher order ($> \chi^{(4)}$) value. To this end, the third-order susceptibility is expressed in terms of relative permittivity of optoplasmonic surface electric permittivity as (Kumela et al., 2022b),

$$\chi^{(3)} = [\varepsilon_r(\omega) - 1]^4, \tag{3.4}$$

In which, the electric permittivity of each layer ($\varepsilon_r(\omega) = \epsilon_0\sqrt{n}$) is expressed in terms of refractive index (n) as summarized in Table.3.1

Table 3.1: Design parameters of proposed sensor structure at visible wavelength.

| **Materials** | **Type** | **Refractive Index** | **Ref.** |
|---|---|---|---|
| Biomolecules | EGFR | 1.66 | Liu et al. (2018a) |
| | ck19 | 1.62 | Chiu et al. (2018) |
| | calu-1 | 1.3 | Zhang et al. (2022) |
| | A427 | 1.5 | Zhang et al. (2022) |
| | 95D | 1.7 | Zhang et al. (2022) |
| | CL1-5 | 1.41 | Liou et al. (2014) |
| | A549 | 1.5 | Huang et al. (2020) |
| | HT-29 | 1.67 | Cao et al. (2021) |
| Dielectric | $Fe_2O_3$ | 3.125 | Jongen et al. (2000) |
| NMNS | Ag | 0.056 | Ali et al. (2023) |
| | Au | 0.185 | Wu et al. (2018b) |
| | Al | 1.43 | Moosmüller et al. (2021) |
| Prism | GGG-Prism | 1.97 | Matiatou et al. (2021) |

On the other hand, the NS and biological molecule (gene) interaction in sensor region resulted in the reflectance of light with different intensities from input (laser light with 1500nm) intensity. This phenomenon helps to investigate the biomolecule's properties by comparing input and output laser intensity. With this consideration, the reflectance of laser-dielectric surface ($r_{Ld}$), dielectric-MNPs ($r_{dm}$) and plasmonic field-biomolecule ($r_{pA}$), interaction calculated employing Eq.(2.23) as,

$$r_{Ld} = \frac{\varepsilon_m k_p - \varepsilon_p k_m}{\varepsilon_m k_p - \varepsilon_p k_m}, \tag{3.5}$$

$$r_{dm} = \frac{\varepsilon_d k_p - \varepsilon_d k_d}{\varepsilon_d k_m - \varepsilon_m k_d}, \tag{3.6}$$

and

$$r_{pA} = \frac{\varepsilon_A k_d - \varepsilon_A k_A}{\varepsilon_A k_d - \varepsilon_d k_A}. \tag{3.7}$$

Where $\varepsilon_A$, $\varepsilon_d$, and $\varepsilon_m$ are permittivity of the biological analyte, dielectric surface, and metallic surface, respectively. Following this, the reflection coefficient of the incident optical signal of the sensor expressed employing Eqs.(3.5) and (3.7) as,

$$r_{LmdA} = \frac{r_{dm+r_{LdA}e^{2jk_{mpA}}}}{1 + r_{LmdA}e^{2jk_{mdA}}}. \tag{3.8}$$

From Eq.(3.8), the propagation constant of resulted biosignals takes the form,

$$k_{sp} = \frac{2\pi}{\lambda}\sqrt{\frac{\varepsilon_A \varepsilon_d \varepsilon_m}{\varepsilon_d + \varepsilon_m}}. \tag{3.9}$$

.

### 3.2.2 Quantum Method to Model Surface Plasmon Polariton Biosensor

To model light-matter interaction into quantum mechanical principle, we neglect the environmental factor by considering the interaction inside the noiseless (closed) cavity mode as illustrated in Figure.3.2. The electron configuration of Figure.3.1 when interact with intense laser field result in V-type electron configuration. Since, two lower energy levels are optically pumped and lead to population inversion and result in subsequent stimulated emission of photons. Thus the V-type laser configuration lies in its ability to achieve population inversion and gain through the excitation of two lower energy levels. This configuration allows for the emission of coherent light at specific wavelengths (Boutabba and Eleuch, 2020). So, by quantizing SPP field dispensed in Eq.(3.1), we express the interaction of laser light and proposed OL by using quantum superposition state via the Hamiltonian

of each quantized SPP field as,

$$\hat{H}_{SPP} = \hat{H}_F + \hat{H}_{OL} + \hat{H}_{Int}. \tag{3.10}$$

Here, $\hat{H}_F, \hat{H}_{OL}, \hat{H}_{Int}$ are Hamiltonian of laser field, Hamiltonian of optical layers (OL), and interaction Hamiltonian, respectively. Thus, starting from classical

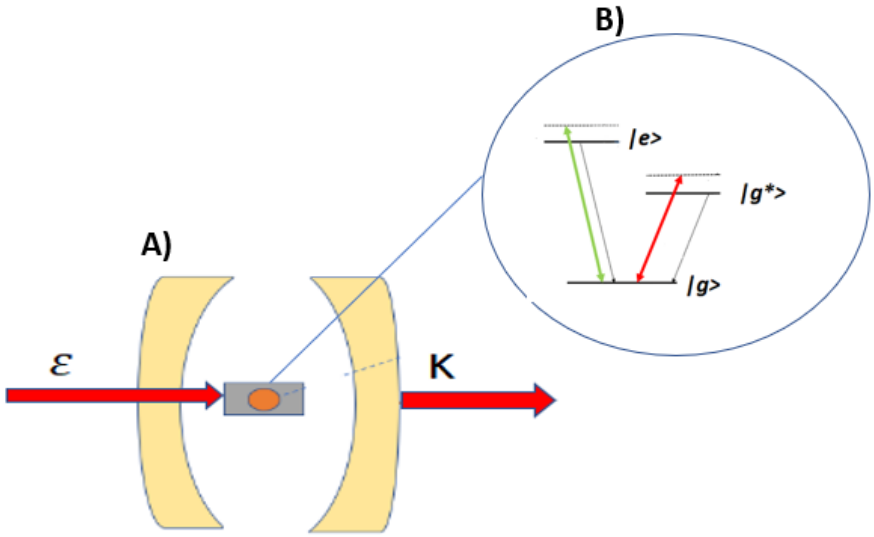


Figure 3.2: *The model of the interaction of laser light ($\lambda = 1500nm$) and MNS inside a closed cavity. A) arrangement of MNS inside closed cavity. B) $V$-type energy level of atom resulted after pumping MNS by intense coherent light.*

incident field given in Eq.(2.8) and substituting the classical variable into quantum notation using Eq.(B.1), the quantized Hamiltonian of the laser field takes the form,

$$\hat{H}_F = \hbar\omega\big(\hat{a}^\dagger\hat{a} + 1/2\big). \tag{3.11}$$

In addition, the laser light-optical layout interaction resulted the collective oscillation of free electrons. Those denoted by $|e\rangle, |g\rangle$ and $|g^*\rangle$ that represent excited state, first ground state and second ground state respectively with the possible transition of atom between $|e\rangle \leftrightarrow |g\rangle$ and $|e\rangle \leftrightarrow |g^*\rangle$ but forbidden for $|g\rangle \leftrightarrow |g^*\rangle$. From the possible transition we drive the generalized quantized Hamiltonian of proposed OL in Eq.(C.4) and we find,

$$\hat{H}_{OL} = \hbar\omega_{eg}\Delta\hat{\delta}^i_+. \tag{3.12}$$

Where, $\frac{E_e - E_g}{2} = \hbar\omega_{eg}$, $\Delta = \omega_{eg} - \omega_{eg^*}$ is detuning and $\hat{\delta}^i_+ = (\hat{\delta}^{i\dagger}_{eg} - \hat{\delta}^i_{eg}) + (\hat{\delta}^{i\dagger}_{g^*e} - \hat{\delta}^i_{g^*e})$, with atomic ladder operators $\hat{\delta}^i_{eg} = |e\rangle\langle g|$, $\hat{\delta}^{i\dagger}_{eg} = |g\rangle\langle e|$, $\hat{\delta}^i_{g^*e} = |g^*\rangle\langle e|$ and $\hat{\delta}^{i\dagger}_{g^*e} = |e\rangle\langle g^*|$.

Following this, the interaction Hamiltonian is calculated employing the quantized dipole approximation given in Eq.(C.5), and by substituting incident field and rearranging atomic operator, the Hamiltonian of light matter interaction takes the form,

$$\hat{H}_{Int} = g\left[\hat{\delta}^{i\dagger}_{eg}\hat{a} - \hat{a}^\dagger\hat{\delta}^i_{eg} + \hat{\delta}^{i\dagger}_{g^*e}\hat{b} - \hat{b}^\dagger\hat{\delta}^i_{g^*e}\right]. \tag{3.13}$$

For, $g = \omega_p^2\sqrt{\frac{\hbar\omega}{2\epsilon_o V}}$ is coupling between field and OL, with V is quantized volume of OL that results $g \propto \frac{1}{R}$ for R is radius of MNPs this implies the smaller the radius the stronger coupling, that expected to have strong quantum properties. And the plasma frequency ($\omega_p^2$). Substituting Eq.(3.11) to Eq.3.13 into Eq.3.10 the patent Hamiltonian of a system takes the form,

$$\hat{H}_{SPP} = \hbar\big(\omega\hat{a}^\dagger\hat{a} + \Delta\hat{\delta}_+ + \omega/2\big) + g\left[\hat{\delta}^{i\dagger}_{eg}\hat{a} - \hat{a}^\dagger\hat{\delta}^i_{eg} + \hat{\delta}^{i\dagger}_{g^*e}\hat{b} - \hat{b}^\dagger\hat{\delta}^i_{g^*e}\right]. \tag{3.14}$$

Moreover, we drive the dynamical equations of proposed system employing Heisenberg-Langavin given Eq.(2.29), and by introducing Eq. (3.14) and applying commutation relations, $[\hat{a},\hat{a}] = [\hat{a},\hat{b}] = [\hat{a},\hat{\delta}_+] = 0$, with $\hbar = 1$ we can see that,

$$\frac{d}{dt}\hat{a} = \frac{-\kappa}{2}\hat{a} - i\omega\hat{a} - ig\hat{\delta}^i_{eg}, \tag{3.15}$$

and

$$\frac{d}{dt}\hat{b} = \frac{-\kappa}{2}\hat{b} - ig\hat{\delta}^i_{g^*e}. \tag{3.16}$$

Using Eq.(D.1) to Eq.(D.16) and steady state solution, the atomic operators

defined as,

$$\hat{a} = \frac{2ig}{\sqrt{N}(\kappa - 2i\omega)}\hat{X}_a, \tag{3.17a}$$

$$\hat{b} = \frac{2ig}{\sqrt{N}}\hat{X}_b, \tag{3.17b}$$

$$\hat{c} = \frac{2g(\hat{X}_a + \hat{X}_b(\kappa - 2i\omega))}{\sqrt{N}(\kappa - 2i\omega)}. \tag{3.17c}$$

Where, $\hat{c} = \hat{a} + \hat{b}$.

Similarly we can find

$$\langle Y_a \rangle_s = \left[\frac{\Delta}{3\Delta^2 + \gamma_b^2}\right] N, \tag{3.18a}$$

$$\langle Y_b \rangle_s = \left[\frac{\Delta}{3\Delta^2 + \gamma_a^2}\right] N, \tag{3.18b}$$

$$\langle Y_c \rangle_s = \left[\frac{\gamma_b}{3\Delta^2 + \gamma_b^2}\right] N. \tag{3.18c}$$

Eq.(3.15) to Eq.(3.18c), represents the dynamical equations of the quantized SPP field. Employing these equations, tailoring plasmonic properties, exploring quantum coherence and entanglement effects, harnessing nonlinear phenomena and quantum information processing (Schulte et al., 2015) were quantified. Thus, some general quantification criteria that can be used to describe quantum properties are; probability distributions, entanglement measures, coherence measures, noise and decoherence rates, and quantum information metrics (such as quantum entropies, fidelity, squeezing, and quantum concurrency) are calculated (Tesfa, 2012).

So, the squeezing properties of certain quantum field are described by quadrature squeezing and quadrature variance that given by (Schulte et al., 2015)

$$(\Delta\hat{c}_\pm)^2 = \langle \hat{c}_+ \hat{c}_- \rangle^2. \tag{3.19}$$

Where, $\hat{c}_+ = \hat{c}^\dagger + \hat{c}$ and $\hat{c}_- = i(\hat{c}^\dagger - \hat{c})$ for, $\hat{c} = \hat{a} + \hat{b}$.

With help of Eq.(3.17a) and (3.18c) , Eq. (3.19) rewritten as,

$$(\Delta\hat{c}_{\pm})^2 = 2(1 + \langle\hat{a}^{\dagger}\hat{a}\rangle + \langle\hat{b}^{\dagger}\hat{b}\rangle + \langle\hat{a}^{\dagger}\hat{b}\rangle + \langle\hat{b}^{\dagger}\hat{a}\rangle) \pm 2(\langle\hat{a}\hat{b}\rangle + \langle\hat{a}^{\dagger}\hat{b}^{\dagger}\rangle) \tag{3.20}$$

Employing the expectation values notation into Eq.(3.17a) to Eq.(3.17c) we find,

$$\begin{aligned}(\Delta\hat{c}_{\pm})^2 &= 2\big[1 + r_a\Delta^2(\langle Y_a\rangle - \langle Y_b\rangle)^2 - r_b\Delta^2(\langle Y_a\rangle - \langle Y_c\rangle)^2 \\ &\quad +\Delta^2\langle Y_a\rangle(\langle Y_a\rangle - \langle Y_b\rangle - \langle Y_c\rangle) + \Delta^2\langle Y_cY_b\rangle\big] \\ &\quad \pm 4\Big[\Delta^2\langle Y_a\rangle(\langle Y_a\rangle - \langle Y_b\rangle - \langle Y_c\rangle) + \Delta^2\langle Y_cY_b\rangle\Big],\end{aligned} \tag{3.21}$$

Substituting Eq.(3.18a) to Eq.(3.18c) into Eq.(3.22), we find,

$$(\Delta\hat{c}_{\pm})^2 = \Delta^2 N\left[1 + \frac{4}{\gamma_a^2 + 3\Delta^2} \pm \frac{2}{\gamma_b^2 + 3\Delta^2}\right]. \tag{3.22}$$

Eq.(3.22) represents, the the plus and minus quadrature. Understanding and characterizing both plus and minus quadrature variances are crucial, as they provide important information about the quantum behavior and fluctuations in a given system. By reducing the quadrature variance, one can minimize the fluctuations and noise in quantum systems, enabling greater precision in measurements and enhanced control over quantum states. This can lead to advancements in various quantum technologies, including quantum computing, quantum communication, and quantum sensing. For instance, in quantum sensing used to reduce measurement noise and improved sensitivity (Chen, 2013; Kandala et al., 2019).

In addition, from quadrature variance we can drive quadrature squeezing using (Kim and Kumar, 1994),

$$S = \frac{(\Delta\hat{c}_{\pm})^2 - (\Delta\hat{c}_{-})^2}{(\Delta\hat{c}_{\pm})^2}. \tag{3.23}$$

Quadrature squeezing allows for reduction in the noise or uncertainty associated with one of the complementary variables of a quantum system. By decreasing this uncertainty, it becomes possible to make more precise measurements of the system's properties. This reduction in uncertainty enables more precise and

accurate measurements, making it a valuable tool for sensing applications by reducing the noise in the interferometer's measurement (Lawrie et al., 2019).

Further, the first inseparability condition proposed by Simon and Duan (Tesfa, 2012) is the sufficient condition for quantification of entanglement in a two-mode CV system. The criterion suggests that if the two modes are separable, they should satisfy the inequality of

$$\Delta\hat{u}^2 + \Delta\hat{v}^2 \leq 2N. \tag{3.24}$$

For, $\hat{u} = m_1 - m_2$, and $\hat{v} = m^{'} - m^{*}$ with $m_1 = (\hat{a}^{\dagger} + \hat{a})/\sqrt{2}$, $m_2 = (\hat{b}^{\dagger} + \hat{b})/\sqrt{2}$, $m^{'} = i(\hat{a}^{\dagger} - \hat{a})/\sqrt{2}$ and $m^{*} = i(\hat{b}^{\dagger} - \hat{b})/\sqrt{2}$.

Substituting Eqs.(3.22) and (3.24) into Eq. (3.23) the Duan-Giedke-Cirac-Zoller (DGCZ) criterion of entanglement quantification takes the form,

$$\begin{aligned} \Delta\hat{u}^2 + \Delta\hat{v}^2 &= 2\Delta^2 N\left[1 + \frac{4}{\gamma_a^2 + 3\Delta^2} - \frac{2}{\gamma_b^2 + 3\Delta^2}\right] \\ &= 2(\Delta\hat{c}_{-})^2. \end{aligned} \tag{3.25}$$

The DGCZ criterion is a measurement that used to quantify the entanglement present in a bipartite quantum system. In the context of plasmonic sensor, this criterion provides insights into the performance analysis of the sensor. Specifically, the DGCZ criterion characterizes the minimum achievable noise level in certain pairs of measurement outcomes for entangled systems. It indicates that if the measured noise levels fall below a certain threshold, called the DGCZ limit, then entanglement is present in the system (Tasgin, 2020).

On the other hand, the second order correlation function (SOCF) is a measure of the statistical correlation between photons in a light field. It quantifies the probability of detecting two photons at different times and locations relative to the probability of detecting them independently. In plasmonic sensor applications, the SOCF provides valuable information about the interaction between light and plasmonic structures. By measuring this function, one can probe the fluctuations and fluctuations in photon emission and absorption processes, that used to study

the dynamics of plasmonic systems as given in (Richards et al., 1982).

$$g^2_{(a,b)}(0) = \frac{\langle \hat{a}^\dagger \hat{a} \hat{b}^\dagger \hat{b} \rangle}{\langle \hat{a}^\dagger \hat{a} \rangle \langle \hat{b}^\dagger \hat{b} \rangle}. \tag{3.26}$$

Since expectation of both beams of light are Gaussian variable with zero means, Eq.(3.26) rewritten as,

$$g^2_{(a,b)}(0) = 1 + \frac{\langle \hat{b}\hat{a} \rangle \langle \hat{a}^\dagger \hat{b}^\dagger \rangle}{\langle \hat{a}^\dagger \hat{a} \rangle \langle \hat{b}^\dagger \hat{b} \rangle}, \tag{3.27}$$

On account of Eq.(3.17a) to Eq.(3.17c) and Eq.(3.18a) to Eq.(3.18c), and applying large time approximation, the second order correlation function takes the form,

$$g^2_{(a,b)}(0) = 1 + \frac{\langle Y_a \rangle \big( \langle Y_a \rangle - \langle Y_b \rangle - \langle Y_c \rangle \big) + \langle Y_c Y_b \rangle}{r_a r_b \Delta^2 (\langle Y_a \rangle - \langle Y_b \rangle)^2 (\langle Y_a \rangle - \langle Y_c \rangle)^2}. \tag{3.28}$$

Eq.(3.28) can reveal important insights into the non-classical properties of light, such as photon antibunching or bunching, which are indicative of the behavior of emitters in close proximity to plasmonic NS. Therefore, analyzing the second-order correlation function in plasmonic sensors offers a powerful tool for investigating and understanding light-matter interactions at the nanoscale, facilitating the development of high-performance plasmonic-based sensing devices (Wang et al., 2022a).

### 3.2.3 Quantum Principles for Biosignal Processing and Telemedicine

#### 3.2.3.1 Lung Cancer Telediagnosis

The phenomenon of quantum information teleportation, as initially proposed by (Bennett et al., 1993), involves transferring the state of a quantum system from a sender to a receiver using entanglement and classical communication. In our proposed scheme, we utilize the concept of teleportation to transfer the quantum state of lung cancer biosignals obtained from a biosensor located at the first health care station (sender) to a second health care station (receiver) without

physically transmitting the signals. This process is accomplished through the use of initialization and bell measurement procedures.

To address this issue, we have proposed the utilization of a dual mirror and a dual beam splitter in a Mach-Zehnder Interferometer (MZI) for further processing of the resulting biosignal, as depicted in Figure.3.2. The incident laser light at a wavelength of 1550 nm serves as the source, and its intensity is divided into two beams by a beam splitter. One of these beams (upper beam) interacts with the sensor region, combines with refracted light, and is subsequently detected by the homodyne detector. Simultaneously, the second beam (reference beam) is directed towards a fully reflective mirror, and upon reflection, is incident on the phase shifter to induce a linearity rotation. This process is repeated twice. Then, a beam splitter is employed to interfere the light originating from the sensor region, as depicted in Figure.3.2. The information gathered from both the lower and upper homodyne detectors is then coupled to the fiber optics cable (FOC).

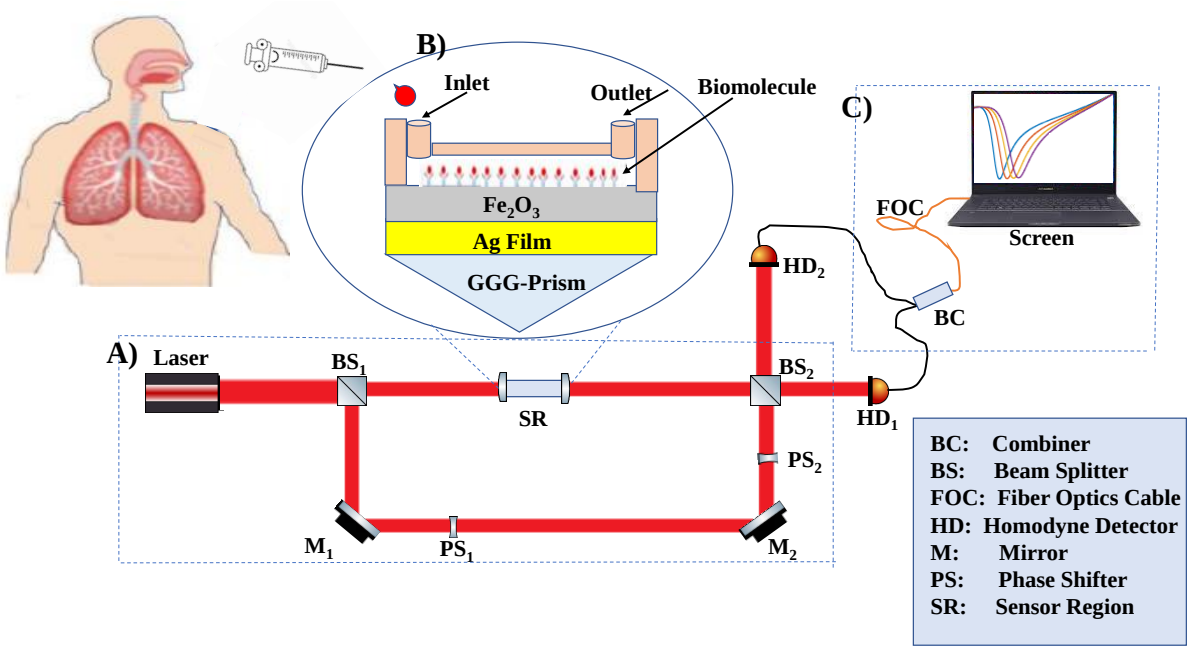


Figure 3.3: *Experimental model of the MZI-based OPBs proposed for lung cancer telediagnosis. A) Laser source, B) arrangement of sensor region (as GGG-prism (12 $\mu m$), Ag (7 $\mu m$), $Fe_2O_3$ (13 $\mu m$) and biomolecules concentration (1250 nM), C) The output biosignals result.*

Quantum mechanically, we can formulate the proposed platform employing

quantization of field obtained from two homodyne detectors by Hamiltonian of a system given by;

$$\hat{H}_{Sys} = \hat{H}_L + \hat{H}_{BS\rightarrow PS} + \hat{H}_{BS\rightarrow SR} + \hat{H}_{int}. \tag{3.29}$$

Where $\hat{H}_L$ is Hamiltonian of the laser light, $\hat{H}_{BS\rightarrow SR}$ is Hamiltonian of the upper beam, and $\hat{H}_{BS\rightarrow PS}$ is Hamiltonian of the lower beam those takes the form,

$$\hat{H}_F = \hbar\omega(\hat{a}^{\dagger in}\hat{a}^{in} + \frac{1}{2}), \tag{3.30a}$$

$$\hat{H}_{BS\rightarrow SR} = \hbar\omega e^{i\phi}\left(\chi^{*(3)}\hat{a}_1^{\dagger}\hat{a}^{\dagger in}\hat{a}^{in} - \chi^{(3)}\hat{a}^{\dagger in}\hat{a}^{in}\hat{a}_1\right), \tag{3.30b}$$

$$\hat{H}_{BS\rightarrow PS} = e^{i\phi\frac{\pi}{2}}\left(\hat{a}_1^{\dagger}\hat{a}^{\dagger in}\hat{a}^{in} - \hat{a}^{\dagger in}\hat{a}^{in}\hat{a}_1\right). \tag{3.30c}$$

In which $\hat{a}^{\dagger in}$ and $\hat{a}^{in}$ are creation and annihilation operator of incident beam and $\hat{a}_1^{\dagger}$ and $\hat{a}_1$ are ladder operator of beam splitter.

Using the Hamiltonian of the upper beam, the beam splitter unitary transformation for the upper arm beam is $\hat{U}_{BS\rightarrow SR} = exp\left[\frac{-i\tau}{\hbar}\hat{H}_{BS\rightarrow SR}\right]$, and for lower arm beam $\hat{U}_{BS\rightarrow PS} = exp\left[\frac{-i\tau}{\hbar}\hat{H}_{BS\rightarrow PS}\right]$ are defined. Then employing the Heisenberg relation (Arthurs and Goodman, 1988) in line with Backer Hausdrof identity (Eriksen, 1968), we can determine the upper and lower arm output field respectively, as

$$\hat{a}_{Upp}^{out} = \hat{U}_{BS\rightarrow SR}^{\dagger}\hat{a}^{in}\hat{U}_{BS\rightarrow SR} = e^{i\phi}cos(|\chi^{(3)}|\tau)\hat{a}^{in}, \tag{3.31}$$

and

$$\hat{a}_{Low}^{out} = \hat{U}_{BS\rightarrow PS}^{\dagger}\hat{a}^{in}\hat{U}_{BS\rightarrow PS} = e^{i\phi}sin(\tau^*)\hat{a}^{in}. \tag{3.32}$$

The upper and lower arm beam superposition is computed with the help of MZI unitary transformation that is expressed by,

$$\hat{U}_{MZI} = \hat{U}_{BS\rightarrow SR}\hat{U}_{BS\rightarrow PS}. \tag{3.33}$$

With this, the output of the combined beam takes the form,

$$\begin{aligned}\hat{c} &= \hat{U}^{\dagger}_{MZI}\hat{a}^{out}_{Upp}\hat{a}^{out}_{Low}\hat{U}_{MZI},\\ &= e^{i\phi}cos\big(|\chi^{(3)}|(\tau-\tau^{*})\big)\hat{a}^{in} - e^{i\phi}sin\big(|\chi^{(3)}|(\tau-\tau^{*})\big)\hat{a}^{in}.\end{aligned} \tag{3.34}$$

From this notation, we can define the horizontal (transmittance) beam and vertical (reflectance) beam respectively, as

$$T = \left|cos(|\chi^{(3)}|(\tau-\tau^{*}))\right|^{2}, \tag{3.35}$$

and

$$R = \left|sin(|\chi^{(3)}|(\tau-\tau^{*}))\right|^{2}. \tag{3.36}$$

The information gained from upper and lower beam are combined using beam combiner to form Bell state formalism (Casado et al., 2010)

$$|\psi\rangle_{FS} = |H\rangle + |V\rangle. \tag{3.37}$$

Where, $|H\rangle = cos(|\chi^{(3)}|(\tau-\tau^{*}))$ is a horizontal beam and $|V\rangle = sin(|\chi^{(3)}|(\tau-\tau^{*}))$ that must satisfy $|H|^2+|V|^2 = 1$, and $\tau$ is the time taken by the upper arm beam and $\tau^{*}$ is the time taken by the lower beam those this shows maximum entanglement for $\tau = \tau^{*}$.

Then, the combined beam is processed as quantum information inside fiber optics cable, by introducing two-mode squeezed vacuum state given as (Van Loock, 2011),

$$\hat{b}^{out} = \hat{S}^{\dagger}(r)\hat{X}^{\dagger}(\theta_{inc})\hat{c}\hat{S}(r)\hat{X}(\theta_{inc}). \tag{3.38}$$

Where, $\hat{S}(r) = exp[\eta^{*}\hat{b}^{\dagger} - \eta^{*}\hat{b}]$ is two-mode squeezed sate for $\eta = e^{r}$ is squeezing parameter, $\hat{X}(\theta_{inc}) = exp[e^{i\theta_{inc}}\hat{b}^{\dagger} - e^{-i\theta_{inc}}\hat{b}]$ is pumping parameters of fiber optics cable for $= \frac{P_{Lo}\varepsilon}{l}$, and $\hat{b}$ and $\hat{b}^{\dagger}$ are ladder operator of squeezed light. In which, $P_{Lo}$ is the power of the local oscillator, $\varepsilon$ is the photon scattering efficiency of fiber and l is the length of the fiber cable and $\theta_{inc}$ is pumping angle. Using Eq.(3.34) into

Eq.(3.38) with Heisenberg picture (Kiilerich and Mølmer, 2019) the output field reduces to

$$\hat{b}^{out} = e^{i\theta_{inc}}\left(cos(\eta^*|\chi^{(3)}|(\tau-\tau^*))\hat{b}^\dagger - sin(\eta|\chi^{(3)}|(\tau-\tau^*))\hat{b}\right). \tag{3.39}$$

#### 3.2.3.2 Teleportation of Biosignals

To further process the resulted biosignals from the proposed biosensor, the first healthcare station (from which the patient blood sample is collected is commonly known as Alice) and second healthcare station (at which lung cancer diagnosis equipment exists commonly known as Bob) must attain a high degree of quantum correlation (entanglement) even if there is infinity distance between them. This phenomenon (entanglement) is used as a physical resource for the quantum teleportation of biosignals between both healthcare stations. Therefore, to demonstrate the teleportation of biosignals, we suppose two qubits ($|\psi_{in}\rangle = \frac{1}{\sqrt{2}}(|00\rangle + |11\rangle)$) and the unknown qubit to be teleported to decode the biosignals ($|\psi_{tel}\rangle = e^{\frac{i\phi}{2}}(cos(\frac{\theta}{2})|0\rangle + e^{\frac{i\phi}{2}}(sin(\frac{\theta}{2})|1\rangle)$ (Pourkarimi and Rahnama, 2014). For $\theta$ and $\phi$ are azimuthal and polar angles, respectively. Then, employing the entanglement quantification parameters called concurrency ($C(\rho_{AB}) = Max(0, \sqrt{\lambda_1} - \sqrt{\lambda_2} - \sqrt{\lambda_3}.... - \sqrt{\lambda_n})$) (Narla et al., 2016), the possibility of the proposed quantum channel to teleport biosignals is determined. For which, $\rho_{AB}$ is the quantum channel between two healthcare stations and $\lambda_i$ are eigenvalues.

So the density operator received by the second healthcare station ($\hat{\rho}_{out}$) in Hamiltonian notation gives,

$$\hat{\rho}_{out} = Tr(\hat{U}\rho_{in} \otimes \rho_{tel}\hat{U}^\dagger). \tag{3.40}$$

Where, $\hat{U} = e^{iH_{Sys}t}$, $\rho_{in} = |\psi_{in}\rangle\langle\psi_{in}|$ and $\rho_{tel} = |\psi_{tel}\rangle\langle\psi_{tel}|$, and employing Heisenberg

interaction picture (Simons, 1978), the teleported biosignal takes the form

$$\hat{\rho}_{out} = e^{\frac{i\phi}{2}} \Bigg( cos(U\hat{n}^{\dagger}\hat{n}^{-} + \omega(\hat{a}^{\dagger}\hat{a} + \hat{b}^{\dagger}\hat{b})) - sin(U\hat{n}^{\dagger}\hat{n}^{-} + \omega(\hat{a}^{\dagger}\hat{a} + \hat{b}^{\dagger}\hat{b})) \Bigg). \tag{3.41}$$

Then, the quality of teleported quantum state (biosignals) is quantified by average fidelity (Pourkarimi and Rahnama, 2014),

$$F_{av} = \frac{1}{4\pi} \int_{0}^{2\pi} d\phi \int_{0}^{\pi} sin\theta F(\theta, \phi) d\theta, \tag{3.42}$$

in which, F$(\theta, \phi) = \langle \psi_{in} | \rho_{out} | \psi_{in} \rangle$ is the fidelity of teleported biosignals.

#### 3.2.3.3 Interpretation of Biosignals

Here, we employ the classical and quantum computing approaches, to interpret the teleported signals. Under classical approach we use the reflectance and transmittance spectra to extract relevant information about biological samples. So, we consider absorption peaks, spectral shape and slope, shifts in wavelength, and quantitative analysis like concentration of biomolecules. With this consideration, the information gain (IG) measurement takes the form (Björk, 2017),

$$IG = \int d\psi_{FS} \sum_{i=1,2,3} {}_{FS}\langle \psi | \hat{c}^{\dagger}\hat{c} | \psi \rangle_{FS}. \tag{3.43}$$

The balance between the information gain and the quantum state disturbance can be quantified by success probability using (Koniorczyk et al., 2001),

$$P(r, \theta_{inc}) = \frac{{}_{FS}\langle \psi | \hat{c}^{\dagger}\hat{c} | \psi \rangle_{FS}}{\sum_{FS} \langle \psi | \hat{c}^{\dagger}\hat{c} | \psi \rangle_{FS}} \tag{3.44}$$

Substitution Eqs.(3.34) and (3.37) into Eq.(3.44) the detection probability reduces to,

$$P(r, \theta_{inc}) = \frac{e^{i\theta_{inc}}}{\qquad} \Bigg( cos(\eta^{*} | \chi^{(3)} | (\tau - \tau^{*})) \hat{b}^{\dagger}) - tanh(\eta^{*} | \chi^{(3)} | (\tau - \tau^{*})) \hat{b}^{\dagger}) \Bigg). \tag{3.45}$$

The discussion of measurement was computed by taking the difference between refractive index after the biomolecule concentration was added (SI) and before the biomolecule (MI) by,

$$\Delta R_{min}^{cancer} = \left| R_{min}^{SI=1250nM} - R_{min}^{MI} \right|, \tag{3.46}$$
$$\Delta \theta_{OPW}^{cancer} = \left| \theta_{OPW}^{SI=1250nM} - \theta_{OPW}^{MI} \right|.$$

Where, $\Delta\theta_{OPW}$ is the angle by which the optoplasmonic wave leaves the sensor region.

Table 3.2: Decisions making based on different situations that occurred in detecting attributes Hossain et al. (2019), and Eq.(3.46)

| **Phatology no.** | **Conditions** | **Discussion** |
|---|---|---|
| 1 | $\Delta R_{min}^{SI-MI} \geq \Delta R_{min}^{cancer} \&\& \Delta\theta_{OPW}^{SI-MI} \geq \Delta\theta_{OPW}^{cancer}$ | Cancer detected |
| 2 | $\Delta R_{min}^{SI-MI} \leq \Delta R_{min}^{cancer} \&\& \Delta\theta_{OPW}^{SI-MI} \geq \Delta\theta_{OPW}^{cancer}$ | Try again |
| 3 | $\Delta R_{min}^{SI-MI} \geq \Delta R_{min}^{cancer} \&\& \Delta\theta_{OPW}^{SI-MI} \leq \Delta\theta_{OPW}^{cancer}$ | Try again |
| 4 | $\Delta R_{min}^{SI-MI} \leq \Delta R_{min}^{cancer} \&\& \Delta\theta_{OPW}^{SI-MI} \leq \Delta\theta_{OPW}^{cancer}$ | no cancer detected |

On the other hand, under quantum computation approach, we apply QML to extract, analyze, and categorize various signals for diagnosis following the three stages of prepossessing (filtering), feature extraction, and classification (Maheshwari et al., 2022). In light of this, we develop the quantum circuit learning (QCL) protocol, which consists of an encoder circuit, variational circuit, and measurement (for estimation of the dose of laser light). Applying the teleported biosignal (Kim et al., 2022) ( $\rho_{out}$) as an input into the encoder circuit, we form quantum state $\rho_{out}|0\rangle^{\otimes n}$) in which n is the number of qubits. Subsequently, the classical database is mapped into a quantum state (Ashhab, 2022) by considering the $Y$ classical (previous lung cancer type, stage, and patient conditions) (Frankell et al., 2023; Li et al., 2023). Each patient data classically represented by $X^N = (x_1, x_2, x_2, ....., x_N)$, this can be mapped to corresponding quantum state as

$N$ quabit $|X^N\rangle = |x_1, x_2, x_2, ....., x_N\rangle$. In general, we can represent the entire dataset as a superposition of computational bases state (Kish, 2023),

$$|Y\rangle = \frac{1}{\sqrt{N}} \sum_{i=1}^{M} |x^i\rangle. \tag{3.47}$$

Following, the classical datasets and teleported lung cancer biosignals were prepossessed and encoded into the quantum circuit. That forms another quantum state $|Y\rangle(\rho_{out}|0\rangle^{\otimes n})$ via a quantum future map that contains entangler blocks to assure flexibility in data representation. Then, the encoded lung cancer dataset is organized into train and test datasets (form variational circuits). Finally, with the measurement circuit, the lung cancer stage is determined by referring input data with registered lung cancer clinical dataset (LCCD) as dispensed in Figure.3.4. In which, $U_{(\Phi(x))}$ is preprocessed previous lung cancer dataset and $U(\phi)$ is the encoded biosignals extracted from optoplasmonic biosensor. This can be expressed by transition probability (Llopis-Cardona et al., 2023),

$$P_{tra} = \langle \Gamma^n | \rho_{out} \rho^*_{out} | \Gamma^n \rangle. \tag{3.48}$$

Where, $|\Gamma^n\rangle = |Y\rangle|0\rangle^{\otimes n}$.

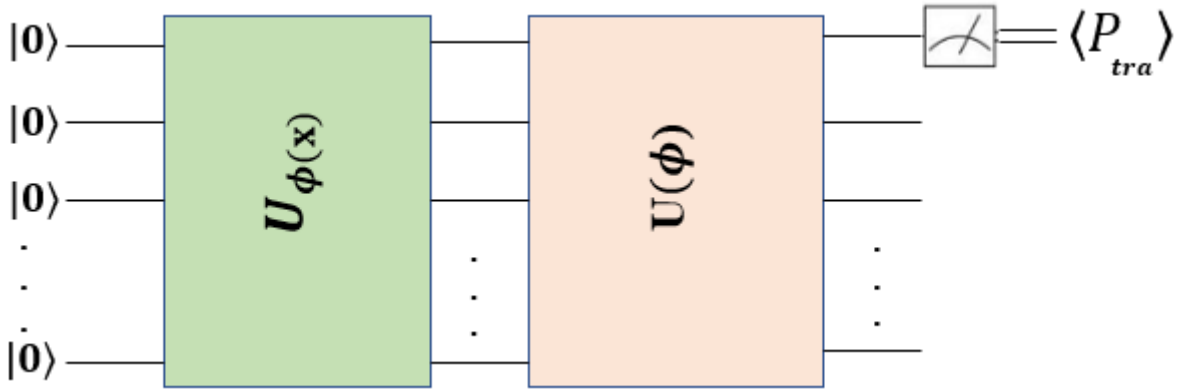


Figure 3.4: *Quantum machine learning circuit for biosignal processing.*

#### 3.2.3.4 Lung Cancer Telemedication

The information obtained under biosignal interpretation section helps to classify lung cancer into different stage, perforation rate, and type. From this information, we establish the procedure dispensed in Figure.3.5, to perform LITT-based lung cancer telemedication. Thus, the estimated LITT takes the form time-varying

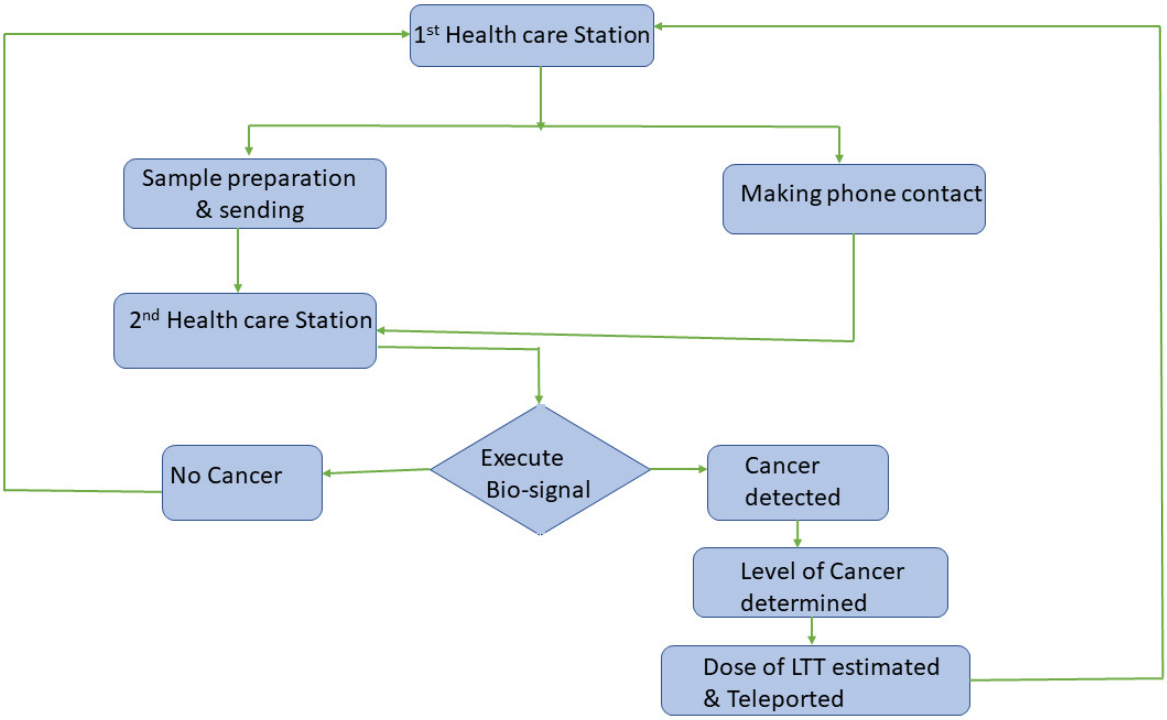


Figure 3.5: The schematic diagram of the overall process to perform lung cancer telemedicine.

electric field that is given by (Liu et al., 2023),

$$\mathbf{E}(r,t) = e_r \frac{\zeta}{r} e^{i(\omega_f t - kr)}. \tag{3.49}$$

For $e_r$ is the longitudinal component of the electric field, $\omega_f$ frequency of LITT field, $\zeta = \sqrt{\frac{jLITT_{in}}{\pi ln(\frac{r_{out}}{r_{in}})}}$ is an integral constant, with j, $LITT_{in}$, $r_{out}$ and $r_{in}$ are wave impedance, LITT input power, the outer and inner radius of endoscopy, respectively, $e^{i(\omega t - kr)}$ is traveling wave factor, for $k = \frac{2\pi}{\lambda}$ is propagation constant. Applying quantization notation proposed by (But et al., 2019), the estimated LITT is ex-

pressed in quantum notation as,

$$\hat{E} = \hbar\omega_f m(\hat{a}^\dagger \hat{a} + \frac{1}{2}). \tag{3.50}$$

Where, $m = e_r \frac{\zeta}{r}$.

In addition, the wavelength-dependent quantum state teleportation with a telecom wavelength can be demonstrated by horizontal and vertical polarisation ($|\Phi\rangle_{in} = cos\frac{\theta}{2}|H\rangle + e^{i\Phi}sin\frac{\theta}{2}|V\rangle$. In which, $\Phi$ are polarisation states, and H and V are horizontal and vertical polarisation eigen basis. In addition, the dose of LITT (Eq.3.50) can be introduced into the input state, and as a result, the output state expressed by,

$$|\Phi\rangle_{out} = \hat{E}|\Phi\rangle_{in}. \tag{3.51}$$

While, by tracing the output state, the final output density operator takes the form,

$$\hat{\rho}_{LTT}^{out} = Tr(|\Phi\rangle_{out\,out}\langle\Phi|). \tag{3.52}$$

The output LITT quantum state is teleported inside fiber optics cable, which is expressed by $\hat{\Omega} = \frac{\alpha}{l}(e^{i\theta}\hat{b}^\dagger - e^{-i\theta}\hat{b})$, for $\alpha$ is scattering efficiency and l is fiber optics length. With this in mind, the teleported LITT takes the form,

$$\hat{\rho}_{LTT}^{tel} = \beta e^{i\theta}\hat{a}^\dagger\hat{a}\big(cos\frac{\theta}{2} + e^{i\Phi}sin\frac{\theta}{2}\big)(\hat{b}^\dagger - \hat{b}). \tag{3.53}$$

In which, $\beta = \frac{\alpha\hbar\omega m}{l}$. The quality and teleportation distance of LITT is expressed by employing teleportation fidelity expressed by (Huo et al., 2018),

$$F_{LITT} =_{in} \langle\Phi|\hat{\rho}_{LTT}^{tel}|\Phi\rangle_{in}. \tag{3.54}$$

To this end, the experimental setup of the proposed platform is dispensed in Figure.3.6. In which, the sensor region and endoscopy are located at the first health care station (from which the patient sample collected), and the patient data

processor, patients situation discussion maker, and the source of LITT are located at second health station. Following, the overall procedure dispensed in Figure.3.5 both health care station are connect via quantum teleportation mechanism.

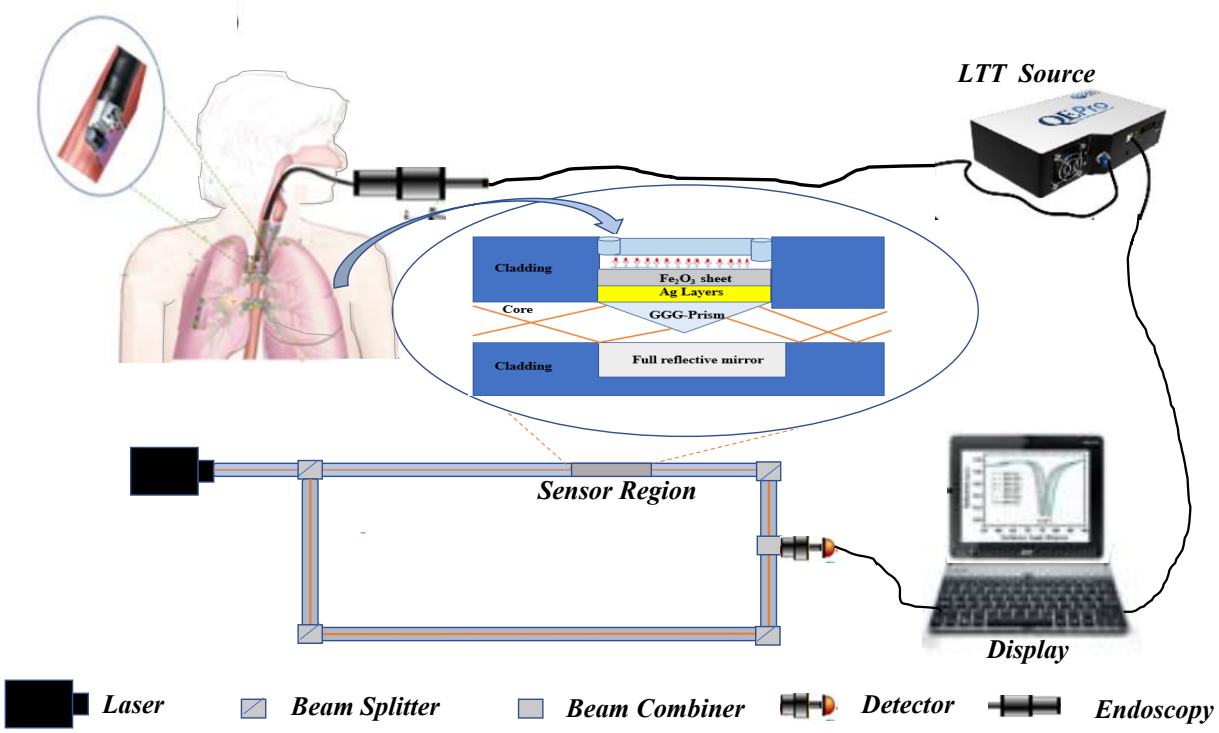


Figure 3.6: The experimental model for lung cancer telemedicine.

# 4

# Results and Discussion

In this chapter the results and discussion of the dissertation work were presented in two sections. Based on theoretical and simulation results, the effects of linear and nonlinear SPR phenomena, sensor layer type, biomolecule concentration, and interrogation type on OPB sensitivity were discussed in the first section. The second section evaluates the quantum mechanical properties of SPP fields and biosignals for further interpretation and processing. Followed by the simulation results of estimation and teleportation of LITT for lung cancer telemedicine.

## 4.1 Classical Approach

### 4.1.1 Evaluation of the Optical Properties of Nanosurface

To utilize noble metallic nanosurface (NMNS) in various applications, such as sensing, imaging, optical manipulation, and optoelectronics, it is necessary to understand their linear and nonlinear properties. Thus, employing Eqs.(2.21) and (2.22) , the properties of different NS (Ag, Au, and Al) under different pumping wavelengths are presented in Figure.4.1. It clearly shows that, the weak interaction between the incident light and NS, leading to a lower overall intensity (as seen in Figure.4.1a ). While, at higher light intensities, NS can experience multiphoton absorption or scattering processes. These nonlinear processes lead to increases in excitation intensity. So, the spectra of nonlinear (Figure.4.1b ) is more broader than linear one (Figure.4.1a ). These indicate that linear properties are mainly attributed to the SPR effect, while nonlinear properties arise from higher-order interactions

between NS and incident photons. Comparing all spectrum of Figure.4.1a and b, the Ag NS tend to exhibit higher intensity, due to fundamental differences in the optical properties of these materials, specifically their plasmonic behavior. Thus, the obtained result agrees with recently reported experimental work of (He et al., 2021), and theoretical work of (Vu Nhat et al., 2021)

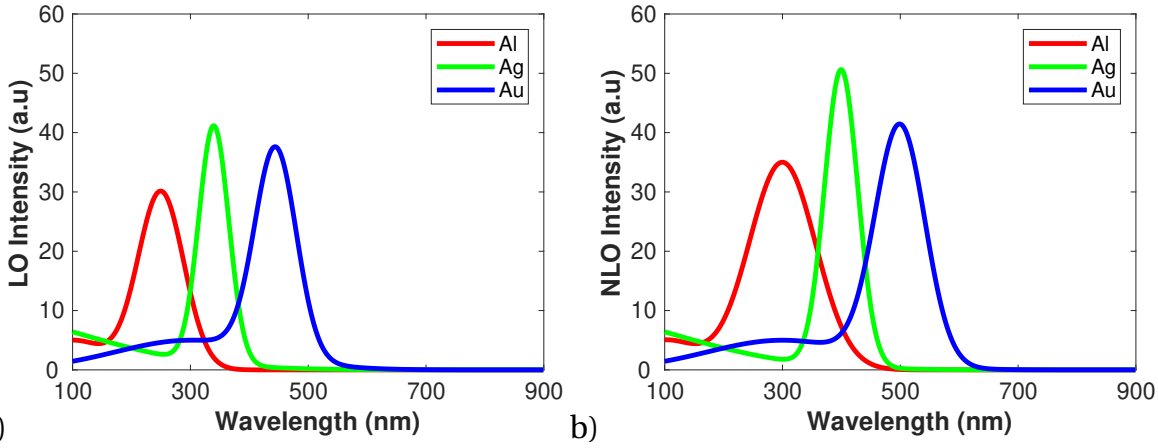


Figure 4.1: *Shows the intensity variation of Al, Ag, and Au NS plotted using Eqs.*(2.21)*, and* (2.22) *and parameters presented in Table. 3.1. For a) linear and b) nonlinear materials.*

In addition, absorption and scattering can have both positive and negative effects on sensitivity, depending on the choice of detection wavelength and the design of the biosensor surface. The size of nanosurface plays a role in enhancing sensitivity by providing a larger surface area for analyte detection and by leveraging unique optical properties associated with nanoscale structures. Thus, employing Eq.(2.24b)b, the absorption cross section of each nonosurface is illustrated in Figure.4.2. It is found that, the absorption spectrum of NMNS shows a distinct peak at the resonant frequency depending on the size, shape, composition, and dielectric environment of the NS. For example, increasing the thickness of MNPS increases the absorption cross-section, since as the size of nanosurface increases, the plasmon resonance wavelength shifts to longer wavelengths.

In comparison of Figure.4.2 a) to c), Al NS have a plasmon resonance in the ultraviolet (UV) region, whereas Ag and Au NS have resonances in the visible region. The UV region has higher photon energies, which can result in increased

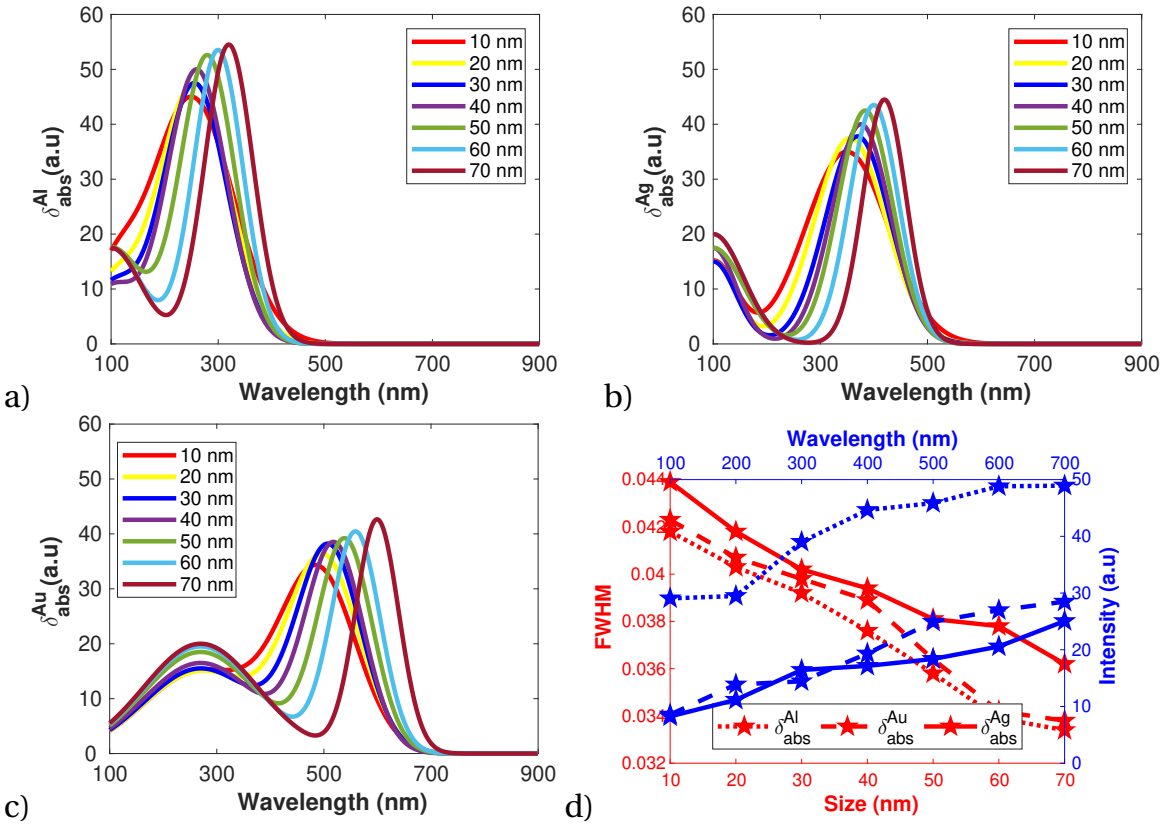


Figure 4.2: *Plot of absorption cross section versus wavelength using Eq.*(2.24b)*, and parameters presented in Table. 3.1. For different surface size of a) Au NS, b) Ag NS, and c) Al NS.*

absorption cross section for Al NS compared to other NMNS of the same shape and size. Further, using the spectra data of Figure.4.2 a) to c), the effect of the size of NS and pumping wavelength on FWHM and intensity is illustrated in Figure.4.2 d). It shows that, when the FWHM is smaller, the spectral feature is narrower, and the intensity tends to be higher. Conversely, when the FWHM is larger, the spectral feature is broader, and the intensity is usually lower since FWHM proportional to length of intensity.

On the other hand, the scattering cross-section tell as the measure of how likely a particle will scatter or deviate from its original path when it encounters another particle or target. Thus, to understand the scattering properties of NMNS, Figure.4.3 plotted employing Eq.3.8. The result indicated that, the size of NMNS is much less than the wavelength of incident light (Rayleigh scattering), and the smaller size results a larger scattering cross-section. Additionally, we observe that Ag NS have a greater scattering cross section than Al and closer scattering

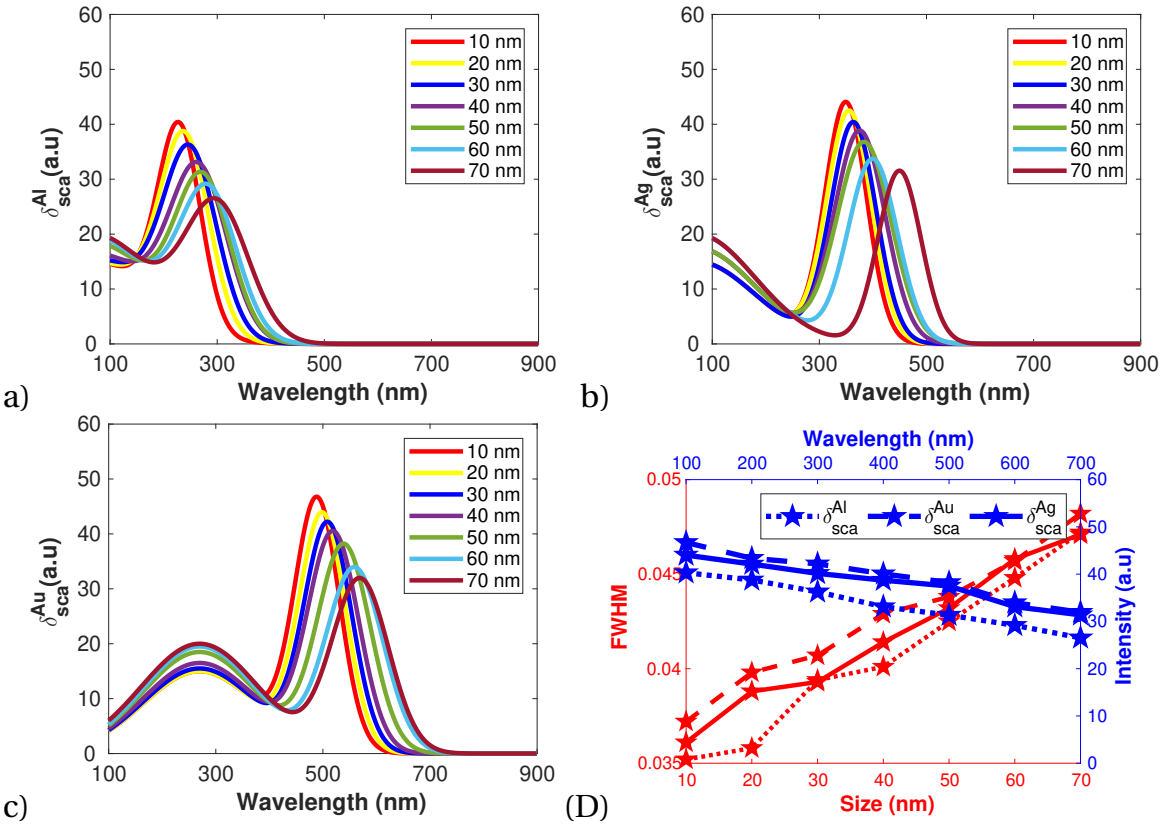


Figure 4.3: *Plot of scattering cross section versus wavelength using Eq.*(2.25b) *b and parameters addressed in Table. 1. For different surface size of a) Al NS, b) Ag NS, and c) Au NS.*

cross section with Au NS of the same shape and size (see Figure.4.3 d) due to their excellent electrical conductivity. Which let free electrons in Ag NS easily interact with incoming light waves and cause scattering. This makes Ag NS to have strong plasmonic resonances as Au NS. As well as, its biocompatability, cheap than Au NPs, and easy to synthesis makes Ag NS more compatible than other NMNS.

In addition, the extinction cross section refers to the ability to absorb and scatter incident light. It plays a crucial role in determining the sensitivity of NMNS for various applications, particularly in sensing and detection. The high extinction cross sections of NMNS are responsible for their sensitivity in sensing applications. So, enhancing the interaction between incident light and NMNS results in higher sensitivity.

Further, the efficiency of SPP field is described by the propagation length and penetration depth, to study cell mechanics for differentiating the affected (cancer)

cells from normal ones. So, to show this clearly, we introduce a nonlinear ray-tracing analyzer with five main components as seen in Figure.4.4. The output measurements of light with and without SPP are presented in Figure.4.5.

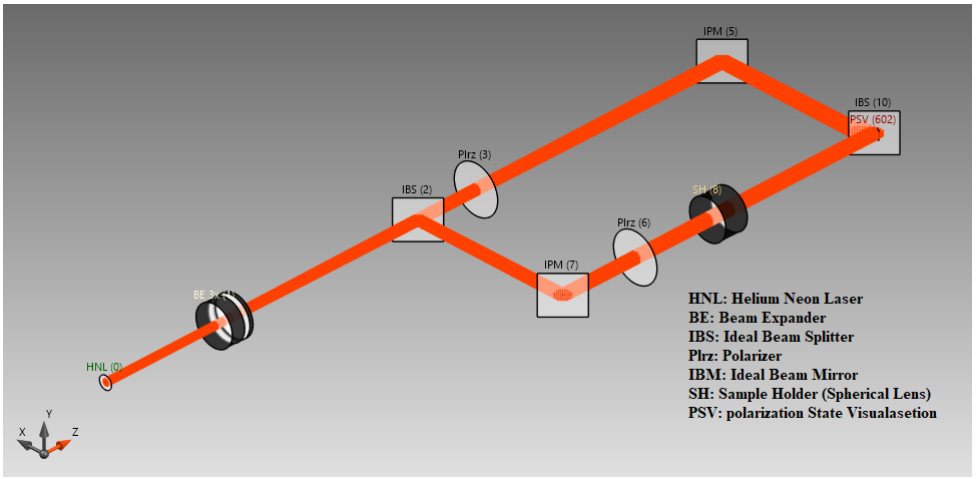


Figure 4.4: *Experimental setup of set up of the components of OPBs using raytracing system analyzer (RSA) simulation engine of VirtualLab Fusion software.*

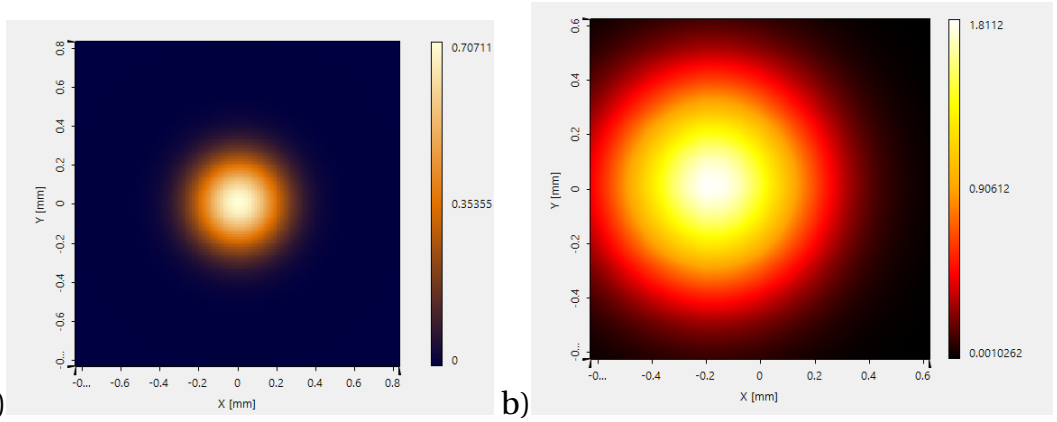


a) b)

Figure 4.5: *Shows the output light without (a) and with surface plasmon polariton (b) in vacuum reservoir using model analyzer simulation engine of VirtualLab fusion software.*

Figure. 4.5 displays, the enhancement of the incident field with MNPs (Ag) to robust the sensitivity and selectivity of OPB. We noted that, Ag NPs have robust brightness of incident light and if any biological samples especially cancer cells are added the obtained brightness is enough to show the cell mechanics of cancer cells clearly.

### 4.1.2 Effect of Sensor Layer on Sensitivity of OPB

The thickness and refractive index of the sensor layer have a significant impact on the sensitivity of SPP biosensor. The sensor layer thickness should be optimized to provide a balance between efficient coupling of incident light to SPP and maximizing interaction with the target analyte. When a sensor layer is too thin, weak signals can be generated, while a layer that is too thick limits the penetration depth of SPP, reducing sensitivity. Additionally, the refractive index contrast between the sensor layer and the surrounding medium affects sensitivity. A higher refractive index contrast leads to stronger SPP coupling and increased sensitivity to changes in analyte concentration or properties. To prove this concept, using Eq.(3.8) we plot reflectance versus plasmonic angle as seen in Figure.4.6.

Figure.4.6a-c shows, the reflectance spectra of different layers of Ag NS layers with different cancer cells. The result demonstrates that, as the number of Ag NPs layers increases, the reflectance spectra shift to the right, and there is a small change in the angle at which biosignals leave the sensor regions. Which clearly indicates the one-to-one correspondence between the number of Ag NS layers and reflectance spectra. In addition, under the same concentration of different types of cancer cells, we observed different spectral shifts since all cells have different refractive indices. These phenomena help to differentiate one type of cancer cell from the other.

Employing Eq.(2.23), the reflection spectra for different arrangement can be piloted. From those spectra, the FWHM ($\frac{\Delta\theta_{OPW}}{2}$) (Karki et al., 2022b), the sensitivity of biosensor ($S = \frac{\Delta\theta_{OPW}}{\delta n}$) (Almawgani et al., 2022) for $\Delta n$ is changed in the refractive index of sample, Figure of merit ($FoM = \frac{S}{FWHM}$), Detection accuracy ($DA = \frac{\Delta\theta_{OPW}}{FWHM}$), Limit of Detection ($LoD = \frac{1}{S}\left(\frac{FWHM}{1.5(DA)^{0.25}}\right)$), and sensor resolution ($SR = LoD \times S$) are evaluated (Hossain et al., 2022). These quantities demonstrates the overall performance of any optical biosensor.

Thus, employing Figure.4.7, the performance of proposed biosensor calculated.

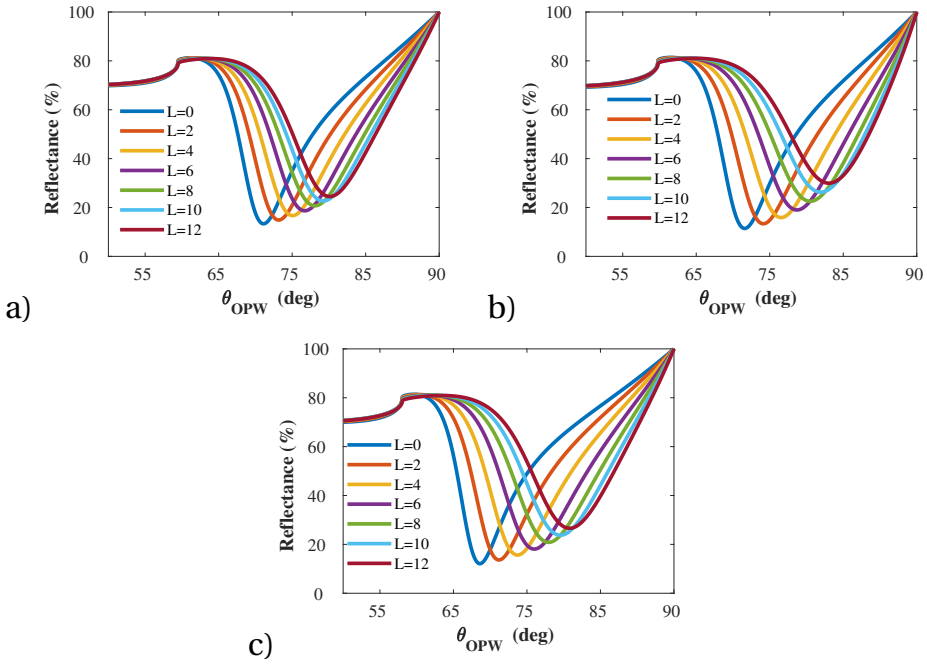


Figure 4.6: *Plot of reflection spectra versus incident angle spectra of various cancer cells measured at different Ag NPs layers plotted using Eq.*(3.8). *a) reflection spectra of CL1-5 cancer cell, b) reflection spectra of A549 cancer cell, c) reflection spectra of HT-29 cancer cells.*

The results indicated that, the sensitivity, FoM, and FWHM increase with the number of Ag NPs layers, and above six layers of Ag NPs, the DA, LoD, and SR decrease since multilayers decrease light penetration. Therefore, the overall performance of the proposed biosensor is high for six layers of Ag NPs. Table. 4.1 generated using the spectral difference shown in Figure.4.7 for six layers of Ag NPs. It demonstrates the overall performance parameters of the proposed sensor under six layers of Ag NPs.

Table 4.1: Performance analysis proposed OPB for three cancer cells. Tabulated using Figure. 4.7.

| Cancer cell | FWHM | $\Delta\theta_{OPW}$ | $\Delta n$ | S (deg/RIU) | FoM (/RIU) | DA(%) | LoD | SR |
|---|---|---|---|---|---|---|---|---|
| CL1-5 | 6.55 | 5.91 | 0.02 | 295.5 | 45.11 | 0.90 | 0.015 | 4.48 |
| A549 | 8.51 | 8.50 | 0.028 | 303.80 | 35.70 | 0.99 | 0.018 | 5.67 |
| HT-29 | 11.52 | 10.39 | 0.031 | 335.45 | 29.11 | 0.91 | 0.023 | 7.88 |

### 4.1.3 Effect of Biomolecule Concentration on Sensitivity of OPB

The biomolecule serves as the recognition element, specifically designed to interact with the target analyte. So, the binding kinetics of biomolecule-analyte

interactions (fast association and dissociation rates) influence biosensor sensitivity. A sensitive biosensor typically requires an optimal balance between fast association for efficient capture and slow dissociation for analyte retention. This ensures prolonged interaction between the biomolecule and the analyte, leading to increased sensitivity. Thus, to show the effect of biomolecule concentration on sensitivity, we employ angle interrogation and wavelength interrogation based investigations.

#### 4.1.3.1 Angle Interrogation

In angle interrogation-based SPP biosensors, the incident angle of light is adjusted to excite SPPs on the sensor surface. The shift in the resonance angle can be detected and correlated with the concentration of analytes or their binding events. Thus, Figure.4.8 explores the impact of cancer cell concentration on sensitivity at which high sensitivity is achieved (L=8). It clearly shows that, the increase in concentration shifts the reflectance spectra to the right and makes the spectral peak short and broad, indicating that light penetration is directly proportional to bio-molecule type and concentration.

On the other hand, by comparing the reflectance spectra of Figure. 4.7 and .4.8, we conclude that, the increment of biomolecule concentration shifts the reflectance spectra to the right (resonance angle increases), which results in a decrease in detection accuracy because the increment of resonance angle shows light scattering. Further, Table. 4.2. illustrates while FWHM and bio-molecule concentration increase, the sensitivity, FoM, and DA decrease. In addition, by comparing the data presented in Table.4.1 and Table.4.2 one can clearly understand the impact of biomolecule concentration on the performance of biosensors.

Table 4.2: Performance analysis proposed OPB in angular interrogation for three cancer cells. Tabulated using Figure. 4.8.

| Cancer cell | FWHM | $\Delta\theta_{OPW}$ | $\Delta n$ | S (deg/RIU) | FoM (/RIU) | DA(%) | LoM | SR |
|---|---|---|---|---|---|---|---|---|
| CL1-5 | 11.42 | 4.65 | 0.0144 | 319.33 | 27.96 | 0.13 | 0.13 | 40.1 |
| A549 | 12 | 6.3 | 0.019 | 332.22 | 27.70 | 0.15 | 0.12 | 40.09 |
| HT-29 | 13.86 | 8.7 | 0.0235 | 365.21 | 26.35 | 0.17 | 0.072 | 26.34 |

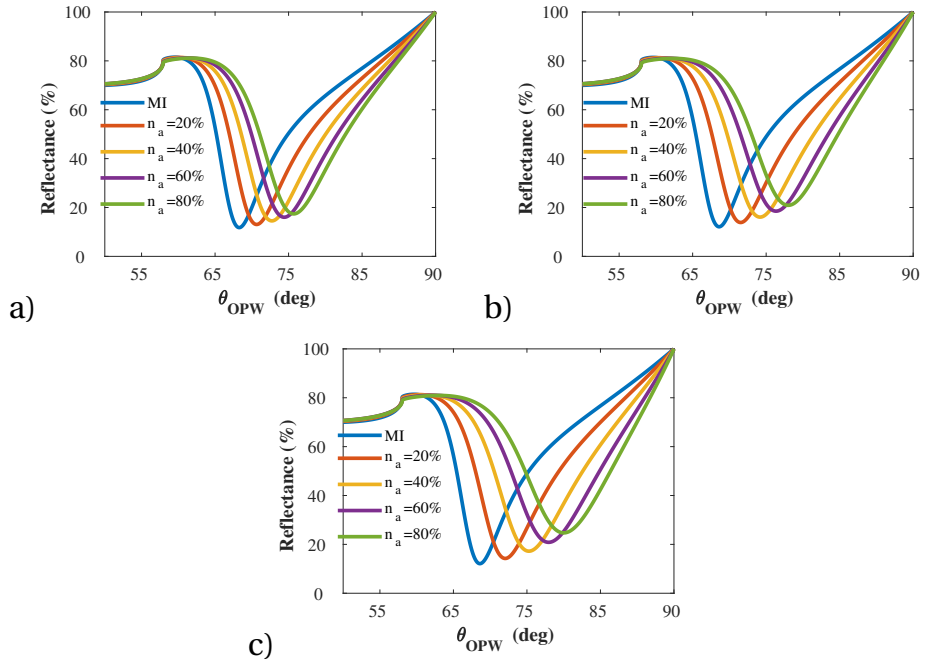


Figure 4.7: *Reflectance spectra of different cancer cell concentrations plotted using Eq.*(3.8) *and parameters defined in Table.3.1. a) reflection spectra of CL1-5 cancer cell, b) reflection spectra of A549 cancer cell, c) reflection spectra of HT-29 cancer cells.*

Further, Figure. 4.8 shows, the considerable variation in sensitivity due to the Ag NPs layers, cancer cell type, and cancer cell concentration. The sensitivity increases with an increase in the number of Ag NPs layers and concentration. In addition, comparing Figure. 4.8 a) and b) the optimized performance of OPBs was obtained by fixing the concentration of biomolecules to 1250 nM and eight layers of Ag NS. In addition, Table.4.3 shows performance analysis of proposed OPB under angular interrogation. The result indicates, the proposed work has highest degree of sensitivity and medium DA, this shows the proposed OPB best suited for lung cancer detection and cost effective than other reported work. On

Table 4.3: Comparison of different performance parameters of the proposed OPBs with other reported SPR biosensors

| **Metal Type** | **S (deg/RIU)** | **DA (%)** | **Detection Target** | **Ref.** |
|---|---|---|---|---|
| SnSe/BlueP/$MoS_2$ | 184 | 0.54 | Blood | Hossain et al. (2022) |
| ZnS/Ag | 293 | 0.16 | DNA | Karki et al. (2022a) |
| $BaTiO_3$Ag/$MoS_2$ | 308 | - | Glucose | Almawgani et al. (2022) |
| Cu/$BaTiO_3$ /BP | 378 | - | Bioanalaytic | Karki et al. (2022b) |
| $Bi_2Te_3$ | 384 | 0.32 | cervical | Uniyal et al. (2022) |
| Ag/$Fe_2O_3$/biomolecule | 365 | 0.17 | Lung Cancer Cell | This Work |

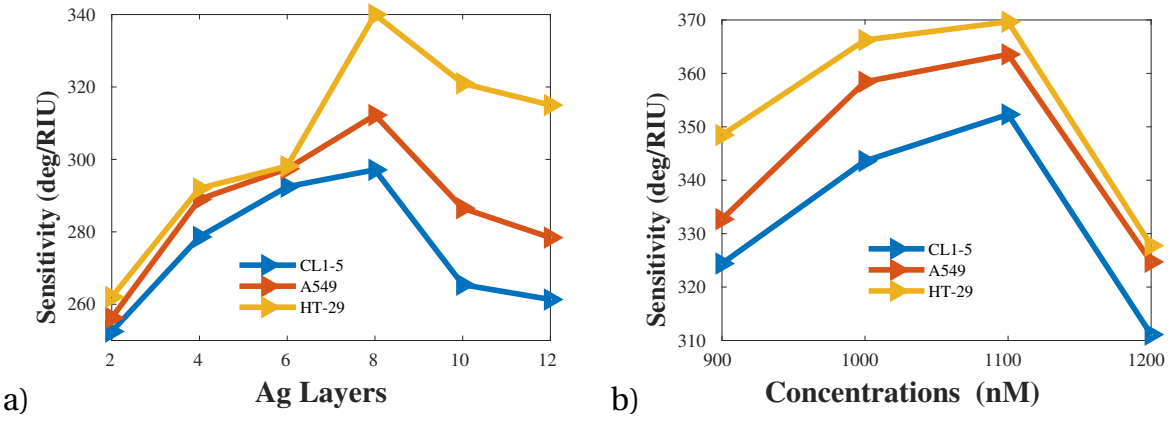


Figure 4.8: *Plot of the sensitivity variation of proposed biosensor obtained by varying Ag NS layers (a) and concentration of cancer cells (b).*

account of Table. 4.1 to Table.4.3, and Figure.4.2 to Figure.4.8, we declare that the proposed OPB is accurately suited for lung cancer telediagnosis.

#### 4.1.3.2 Wavelength Interrogation

In wavelength interrogation SPP biosensor, instead of measuring the angle of resonance, the device tracks the shift in the wavelength of the reflected light. This shift is directly related to the change in the resonance angle caused by binding events on the sensor chip surface. Following, using the parameters given in Table .3.1 and the reflectance equation (Eq. (3.13)), the reflectance spectra of different lung cancer cells under different concentrations are demonstrated clearly in Figure.4.9. Where, Figure.4.9 a) illustrates, the reflectance spectra of the Calu-1 cell, which implies that as the concentration of biomolecules increases, the reflectance also increases, the same is true for Figure.4.9 b), c), d) and e). Notably, Figure.4.9 shows different cancer cell have different spectral profile even at the same concentration, this results from all cancer cell have finger print refractive index this agrees with (Zhang et al., 2021).

In addition, due to the refractive index increment between cancerous cells, the wavelength shifts rightwards with a small increment. This causes a decrease in FOM but increases sensor resolution. In this situation, the cancer cells show a higher refractive index than normal plasma cells, which agrees with other experimental work expressed in (Zhang et al., 2022; Liu et al., 2018a), this helps to

differentiate affected and normal cells. In addition, comparing the five considered lung cancer cells, the 95D cell shows maximum detection efficiency hence, it has a high refractive index (shows 95D cell had the highest metastatic capacity).

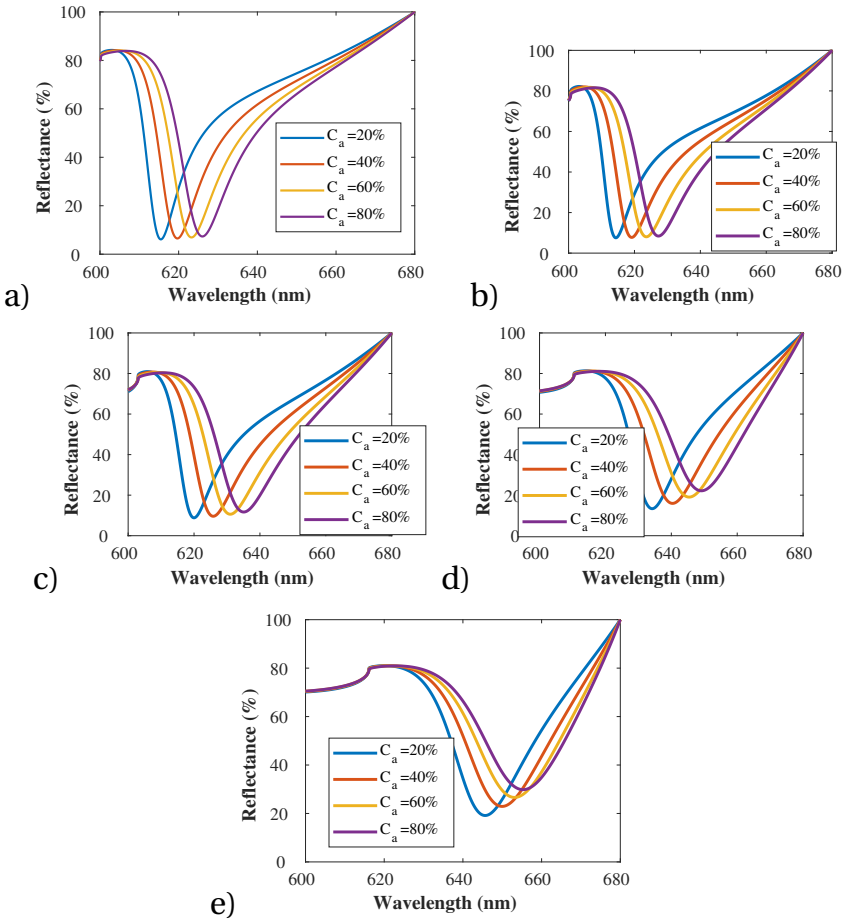


Figure 4.9: *Shows the effect of biomolecule type, and concentration on reflectance spectra plotted using Eq.*(3.8) *and parameters presented in Table.3.1. For a) Calu-1, b) A427, c) CK19, d) EGFR and e) 95D.*

Towards a deeper insight, Table.4.4 summarizes, the evaluation of the sensor performance of the proposed OPB. It clearly shows that the increase in pumping frequency increases sensor sensitivity and resolution. In addition, Figure.4.10 illustrates the performance of OPB for detection of different lung cancer cells. The sensitivity and FOM of the model are calculated under 80% biomolecule concentration. The maximum sensitivity and FOM were recorded to be as high as 10421 nm/RIU and 453.08 $RIU^{-1}$, respectively, at a wavelength of 660 nm. By comparing sensitivity and FOM, we can conclude that as sensitivity increases, FOM decreases due to a low spectral shift, which causes a small change in FWHM.

Table 4.4: The maximum performance of proposed OPB at 80% concentration of different cancer cells impressed in plasma using data presented in Figure.4.9.

| Types of cell | S (nm/RIU) | $\lambda_1$ (nm) | $\lambda_2$ (nm) | FWHM | FOM ($RIU^{-1}$) | R |
|---|---|---|---|---|---|---|
| Calu-1 | 10230 | 620 | 636 | 16 | 639.38 | 2.74 |
| A427 | 10265 | 622 | 639 | 17 | 603.82 | 3.21 |
| Ck19 | 10318 | 638 | 648 | 20 | 515.9 | 3.45 |
| EGFR | 10352 | 640 | 662 | 22 | 470.54 | 3.59 |
| 95D | 10421 | 647 | 670 | 23 | 453.08 | 3.63 |

Furthermore, comparing the proposed biosensor with some recently reported works (Jabin et al., 2019; Yasli, 2021), the proposed biosensor is relatively highly sensitive in terms of wavelength modulation as tabulated in the Table.4.5.

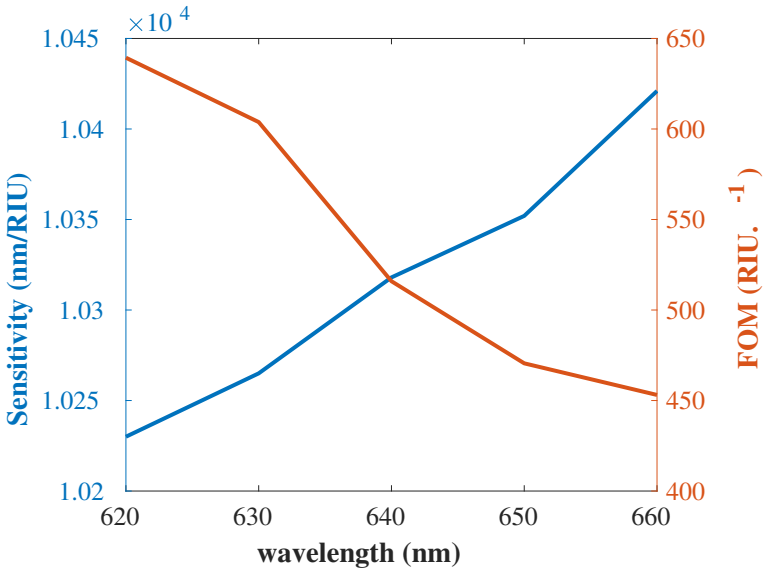


Figure 4.10: Plot of sensitivity versus wavelength plotted using spectral difference of Figure.3.9. Red line for figure of merit, and green for sensitivity.

Table 4.5 presents the performance analysis of the proposed OPB using wavelength interrogation. When compared to other studies, the results indicate that the proposed biosensor exhibits moderate sensitivity, while achieving maximum figures of merit (FOM) and resolution. Consequently, the overall performance of the proposed OPB is highly recommendable for lung cancer detection.

Table 4.5: Comparison of the proposed OPB with existing plasmonic sensors in the literature.

| Model | Cancer | S | FOM | R | Year | Ref |
|---|---|---|---|---|---|---|
| MIM LSPR | A549 | 1670 | | 3.5 | 2018 | (Chang et al., 2018) |
| | Hela | 10208.33 | 340 | - | 2019 | |
| D-shape PCF | Basal | 17500 | 430 | - | 2019 | (Jabin et al., 2019) |
| | PC12 | 10000 | 375 | - | 2019 | |
| | MCF-7 | 742.86 | - | 1.4 | 2021 | |
| PCF | Basal | 3150 | - | 3.2 | 2021 | (Yasli, 2021) |
| | PC12 | 5500 | - | 1.8 | 2021 | |
| | Jurkat | 17143 | 261.84 | 5.83 | 2022 | |
| | Hela | 15833 | 326.72 | 6.32 | 2022 | |
| | MCF-7 | 53571 | 560.66 | 1.87 | 2022 | |
| | Calu-1 | 10230 | 639.38 | 2.74 | 2022 | This Work |
| OPB | A427 | 10265 | 603.82 | 3.21 | 2022 | |
| | Ck19 | 10318 | 515.9 | 3.45 | 2022 | |
| | 95D | 10421 | 453.08 | 3.63 | 2022 | |

## 4.2 Quantum Mechanical Approach

### 4.2.1 Verification of Quantum Feature of SPP

SPPs exhibit unique quantum plasmonic effects, such as quantum tunneling and quantum correlations. Quantum tunneling enables SPPs to propagate through subwavelength gaps or barriers, which would not be possible classically. So, quantifying the quantumness, or the degree of quantum behavior, of a physical system is critical. Some measurements that can be used to assess the quantumness of a system are: observation of non-classical effects in light-matter interactions (such as photon antibunching or squeezing), degree of entanglement (measured by concurrence, entropy-based measures, or entanglement witness), and coherence (represents the stability and phase relationship between different quantum states).

Quantum correlations arise due to the interaction of SPPs with other quantum systems, leading to phenomena such as quantum squeezing or anti-bunching. Therefore, using Eq.3.49 and .3.50, we plot quadrature variance (Figure.4.11) and quadrature squeezing (Figure.4.12). Figure.4.11 shows, the quadrature variance

increases with detuning and frequency but decreases as the size of MNS increases. This indicates that more tiny particles (10-40 nm) have quantum future than bulk materials, and the squeezing occurs in minus quadrature. In plasmonic biosensors, this phenomenon indicates improved sensing performance and increased sensitivity. This phenomenon has valuable implications for optimizing the design and performance of biosensors, enabling advancements in diverse applications including medical diagnostics, environmental monitoring, and food safety.

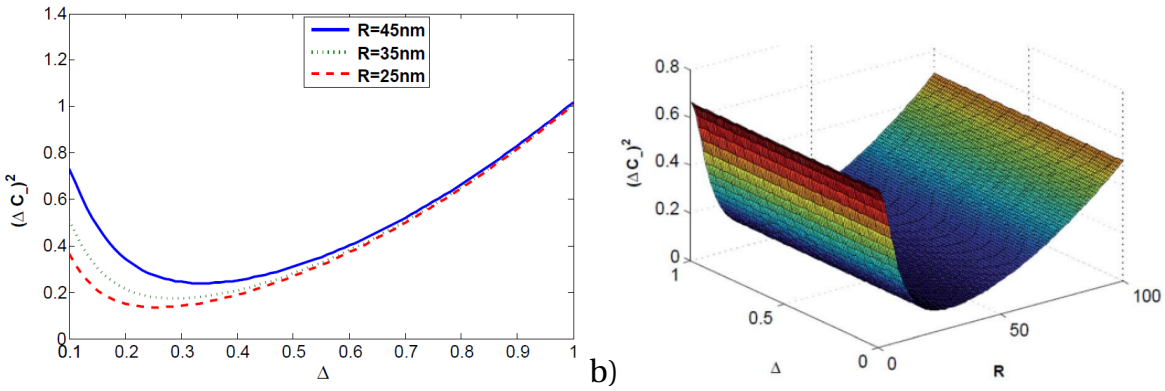


Figure 4.11: *Plot of quadrature variance versus detuning for different size of Ag NS,* $\kappa = 0.8$*, plotted using Eq.*(3.23) *and parameters presented in Table. 1. a) 2D and b) 3D*

In addition, Figure.4.12 illustrates the direct relationship between degree of squeezing and detuning, as well as the inverse relationship between size of Ag NS, and frequency. Therefore, to enable perfect encoding and transmitting quantum information within a given communication channel, it is recommended to use nonlinear optical systems with small sizes. Notably, increasing quadrature squeezing enables the plasmonic sensor to detect smaller changes in the surrounding environment, leading to higher resolution and enhanced capabilities in biomedical sensing, the result agree with (Lawrie et al., 2019; Li et al., 2020).

On the other hand, from Figure.4.13 we observe, the degree of entanglement is proportional to detuning but decreases as the size of MNS increases. This shows detuning is proportional to relaxation time, and as the size of MNS decreases relaxation time increases since polariton (collective free electron) can propagate through tiny particles freely. Thus, the higher entanglement implies enhanced

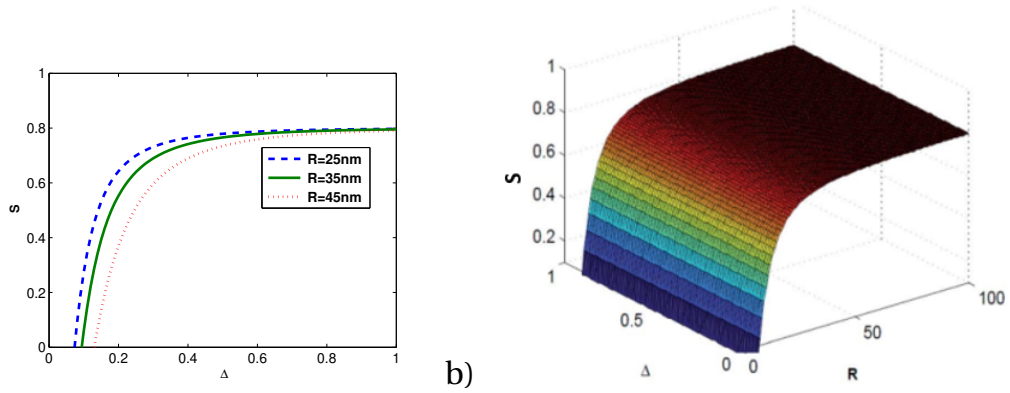


Figure 4.12: *Plots of quadrature squeezing versus detuning for different size of Ag NS and* $\kappa = 0.8$, $\omega_p = 13.716$ *plotted using Eq.*(3.24). *a) 2D and b) 3D.*

correlation and precision, enabling more precise measurements and increased information extraction from the sensor's output signals. This can lead to improved detection limits and better characterization of bioanalytes, enhancing the overall performance of the plasmonic biosensor this agree with (Xavier et al., 2021; Mataji-Kojouri et al., 2020).

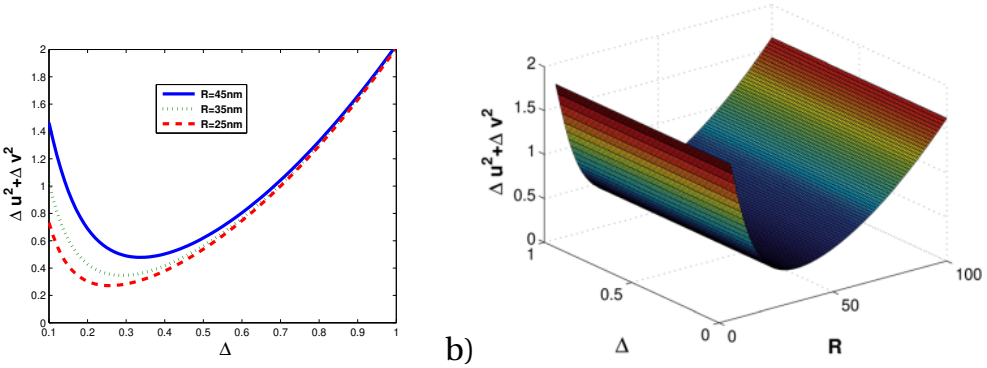


Figure 4.13: *Plot of Duan et al. Entanglement versus detuning for different size of MNS, and* $\kappa = 0.8$, $\omega_p = 13.716$ *and* $\lambda = 632nm$ *plotted using Eq.*(**??**). *a) 2D and b) 3D.*

Besides, Figure. 4.14 shows, degree of correlation increases with detuning and decreases as the size of Ag NPs increases since as the size of material increases, the absorption of light leads to the production of thermal energy that results in noise.

### 4.2.2 Analysis of Teleportation Quality of Biosignals

Quantum teleportation is a protocol in quantum information theory that allows, the transfer of quantum states between distant locations without physically mov-

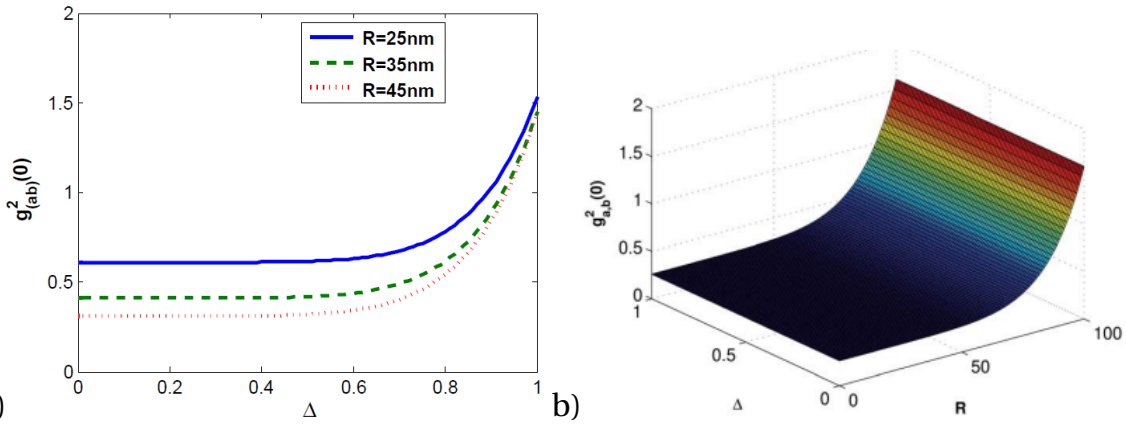


Figure 4.14: *Plots of second order correlation function versus detuning for different size of Ag NPs, and* $\kappa = 0.8$, $\omega_p = 13.716$, *plotted using Eq.*(3.27).

ing the particles carrying those states through entangled qubits and quantum teleportation protocols. The development of quantum networks, incorporating quantum teleportation, could provide a potential avenue for transferring information encoded in biological signals from one location to another using quantum teleportation techniques. This could facilitate the transmission of certain types of biological signal information between networked nodes.

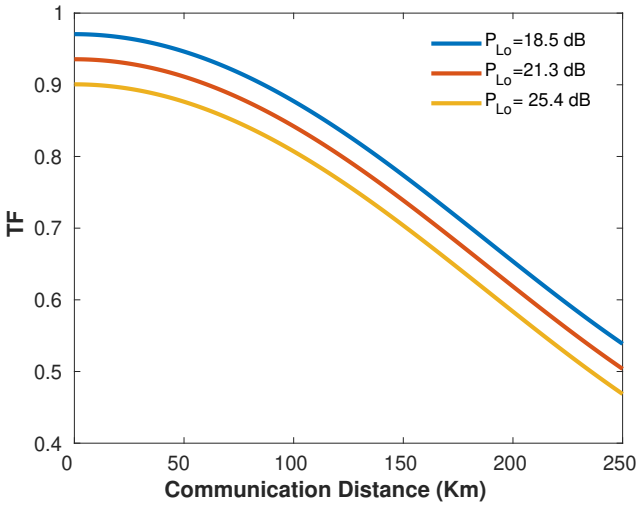


Figure 4.15: *Plot of teleportation fidelity versus communication distance (Eq.*(3.42)*) under different pumping power.*

Figure.4.15 shows, with the increasing pumping power and communication distance, the teleportation fidelity decreases to below the classical limit since increasing pumping power induces noise in the fiber channels. This shows the gradual reduction of quantum entanglement that consequences unsuccessful

communications. Therefore, for successful teleportation, considering fiber optics cable loss, pumping power of input light, and communication distance is vital. To this end, we can summarize the maximum communication distance (200 Km) achieved by limiting pumping power to 18.5 dB. The result agrees with previously reported experimental and theoretical work of (Wengerowsky et al., 2019; Zhang and Zheng, 2021; Fröhlich et al., 2017).

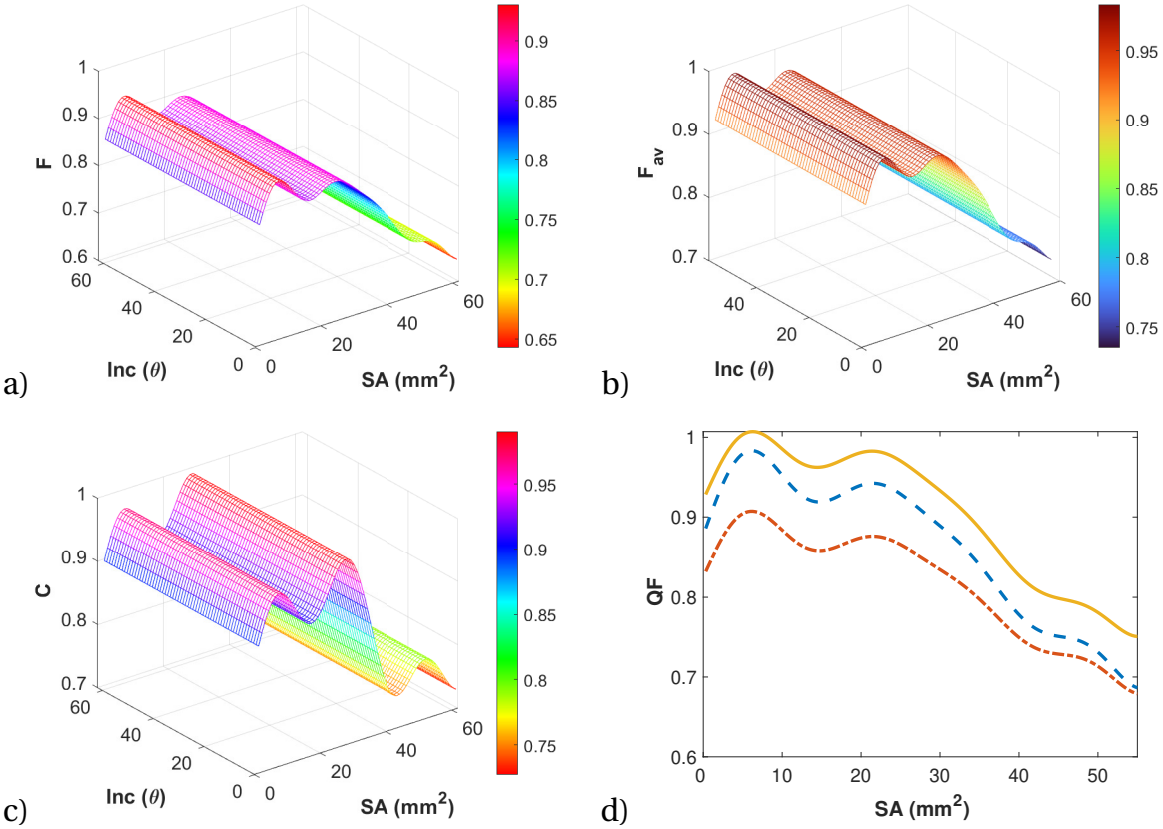


Figure 4.16: *Teleportation quality of the proposed quantum channel plotted using data dispensed in Table.3.1, and $\phi = \pi/2$, M=125 g as a function of sensor area (SA) and pumping angle (Inc). a) biosignal teleportation fidelity, b) average teleportation fidelity, c) a concurrence of shared entangled state between two healthcare stations, and d) comparison of all (F, $F_{av}$, and c) investigated QF (where solid line is for concurrence, dashed line (green) for average fidelity, and broken line (red) for fidelity).*

In Figure.4.16 we disclose the teleportation of the proposed quantum channel to connect two healthcare stations for effective lung cancer telediagnosis. In particular, we demonstrate the concurrence of shared entangled state in Figure.4.16 c), and the biosignal teleportation fidelity and average fidelity (Figure.4.16 a) and b)). We notice that the fidelity decrease as biosensor surface area increase, and

the strong QF is observed at the lowest incidence angle. Hence as the angle of incidence increases, there is a chance that the incident laser light interacts with the environment, which causes the noise that reduced the rate of fidelity. Moreover, in comparison of Figure.4.16 a) to d) with other related work Cao et al. (2022); Kirdi et al. (2023); El Anouz et al. (2020), it is evident that the proposed system shows the maximum degree of correlation and teleportation fidelity.

### 4.2.3 Computing QML Model for Biosignal Interpretation

Biosignal interpretation involves analyzing various biological signals, such as EEG (electroencephalography), EKG (electrocardiography), or EMG (electromyography), to gain insights into the underlying physiological processes. Quantum computing could potentially offer advantages for faster processing of large-scale datasets. So, employing Eq.3.46, the over all discussion measurement obtained. Further, to interpret the obtained result, Eq.3.48 employed. The result dispensed in Figure.4.17 shows that, as information of lung cancer clinical data (LCCD) restriction increase, the biosignal interpretation accuracy increases.

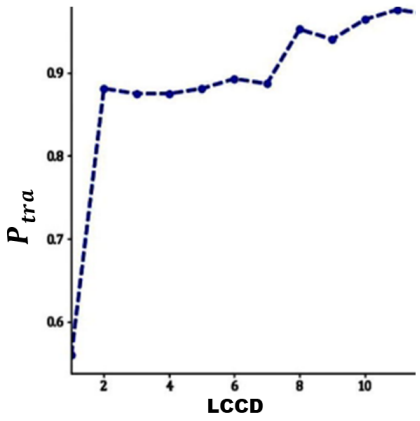


Figure 4.17: *Plot of biosignal interpretation accuracy (Eq.*(3.45)*) versus lung cancer clinical data.*

### 4.2.4 Evaluation of the teleportation of LITT

Quantum teleportation is transfer of quantum state between distance quantum ends. So, employing quantization of LITT (Eq.3.50 to Eq.3.53), the teleportation

fidelity of LITT illustrated in Figure.4.17

Figure.4.17 demonstrates teleportation fidelity of LITT decreases as the distance of communication increases and falls to the classical limit (below $2/3$) when it extends 250 Km. In addition, comparing Figure.4.17 a) and Figure.4.18, we notice that the maximum teleportation quality and distance achieved for LITT than biosignal teleportation. These show that the transmission fidelity decreases as pumping power increases, and the higher transmission fidelity (96% for 18.5 dB squeezing with 0.4% loss) biosignals and 98% for LITT. We deduce from this result that the more accelerating power tends to lose biosignals.

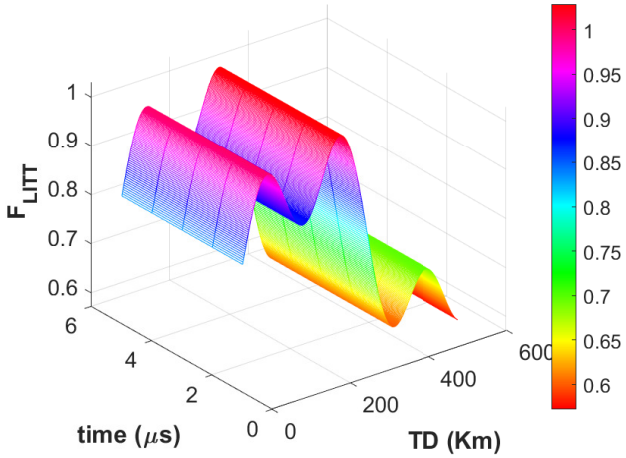


Figure 4.18: *The 3D plot of LITT teleportation fidelity as a function of cancer ablation time and teleportation distance (TD) for* $\theta = 45^o$, $\Phi = \pi/2$, $LITT_{in} = 805nm$, $\lambda = 1500nm$, $r_{in} = 4.2\ mm$, $r_{out} = 1mm$.

# 5

# Conclusions

In this research, we established the classical and quantum approach to modelling the optical properties of MNPs for enhancement of the sensitivity and selectivity of proposed biosensor. Using Maxwell equations and the modified Drude model, the equations of dielectric function of materials are obtained. Then, relaxation time, absorption efficiency, and extinction efficiency of linear and nonlinear optical properties of SPP are calculated. The numerical result shows that, the sensitivity of OPB increases as the size of noble MNPs decreases, and Ag NPs are more efficient for sensitivity and selectivity enhancement compared with other MNPs.

Further, applying the Fresnel and transfer matrix equation and refractive index of different lung cancer, the effects of different layers of Ag NPs and different concentrations of biomolecules on FWHM, DA, sensitivity, and FOM were investigated. After comparing the reflection spectra of the sample and medium-induced light, a description of the resulting biosignals has been developed. The results show that, the suggested approach has an extremely high sensitivity of 365 deg/RIU and an average sensor resolution of 26 $RIU^{-1}$. Furthermore, using the frequency interrogation method, the highest sensitivity (10421 nm/RIU), FOM (453.08 $RIU^{-1}$), and SR (3.63 RIU) were achieved. Taking the proposed sensor's overall performance and comparing it with previously published data, the suggested biosensor is well suited for detection of different lung cancer cells.

In addition, by quantizing the equation of propagation field, Hamiltonian of the

system, quantum Langevin equation, and quantum nature of SPP are examined. The result reveals that, to enable perfect encoding and transmitting quantum information, it is recommended to use nonlinear optical systems, homodyne detection or parametric amplification with small sizes. Then, the teleportation of biosignals between two healthcare stations has also been studied employing the quantum input-output relation, and at the optimum pumping strength (18.5 dB), the signals have successfully traveled 200 km via FOC. Moreover, by introducing quantum principles for biosignal processing and teleporting the dose of light, high transmission fidelity was recorded. This could open up a wide range of extremely exciting possibilities for cancer telemedicine in future medical applications.

# Future Research and Recommendations

The main finding of this research is optimization of the sensitivity of optoplasmonic biosensor employing different noble MNPs, teleportation of biosignals and laser interstitial thermal therapy, and interpretation of biosignals via quantum machine learning model to realise lung cancer telemedication. Thus, high sensitivity (10421 nm/RU), maximum teleportation distance (250 km) with 96% transmission fidelity, and high accuracy (94%) in clinical data processing employing a quantum support vector machine algorithm were theoretically achieved. However, due to financial and laboratory facility constraints, the experimental part was not addressed in this research. Therefore, in the future the hybridization of optoplasmonic biosensor with other optical materials like photonic crystals, metamaterials, optomechanics, and surface enhanced raman spectroscopy is a broad experimental and theoretical area of investigation. In addition, to further enhance teleportation distance, quantum repeaters are crucial devices for long-distance quantum teleportation and quantum communication.

# Appendix

## A Output Field

The input field for light-field interaction represents the incident light that interacts with a material or system. It describes the properties of the incoming light, such as its intensity, polarization, and spatial distribution. Understanding the input field is crucial for analyzing the interaction between light and the system, enabling the study of phenomena such as absorption, scattering, and modulation of the light field. Therefore, to broaden this investigation employing the Fourier transformation given in Eq.(A.1a), the position dependent field is transformed into frequency dependent field as,

$$\mathbf{E}(\omega,t) = \int \big[\mathbf{E}(r,t)exp(-2\pi\omega r)\big]dr, \tag{A.1a}$$

$$= A_0 exp(kr-\omega t). \tag{A.1b}$$

In which, $A_0$ is complex amplitude of the matter.

In the context of light-matter interaction, the output field can be described in terms of absorption, reflection, and transmission. Considering an interface between two different media where electromagnetic waves interact, we can write the plane wave solutions for the electric fields in medium 1 and medium 2 as follows:

$$\mathbf{E}_1(\omega,t) = A_1 exp(k_1 r-\omega t), \tag{A.2a}$$

$$\mathbf{E}_2(\omega,t) = A_2 exp(k_1 r-\omega t). \tag{A.2b}$$

Where, $A_1$ and $A_2$ is complex amplitude of medium.

The output field resulting from the interaction of incident field with interfaces or objects can indeed be analyzed in terms of absorption, transmission, and reflection.

$$\mathbf{E}_{out}(\omega,t) = \mathbf{E}_{abs}(\omega,t) + \mathbf{E}_{tra}(\omega,t) + \mathbf{E}_{ref}(\omega,t) \tag{A.3}$$

Where,

$$\mathbf{E}_{abs}(r,t) = A\mathbf{E}_{in}(r,t), \tag{A.4a}$$

$$\mathbf{E}_{tra}(r,t) = T\mathbf{E}_{in}(r,t), \tag{A.4b}$$

$$\mathbf{E}_{ref}(r,t) = R\mathbf{E}_{in}(r,t). \tag{A.4c}$$

In which, transmission coefficient ($T = \frac{|\mathbf{E}_{tra}|^2}{|\mathbf{E}_{inc}|^2}$), absorption coefficient ($A = \frac{|\mathbf{E}_{abs}|^2}{|\mathbf{E}_{inc}|^2}$), and reflection coefficient ($R = \frac{|\mathbf{E}_{ref}|^2}{|\mathbf{E}_{inc}|^2}$) for $\mathbf{E}_{inc}$, $\mathbf{E}_{tra}$, $\mathbf{E}_{ref}$, and $\mathbf{E}_{abs}$ are amplitude of incident field, amplitude of reflected field, amplitude of transmitted field, amplitude of reflected field, and amplitude of absorption field.

# B Quantization of SPP Field

Employing $\mathbf{E}_{SPP}(\omega,t) \rightarrow \hat{\mathbf{E}}_{SPP}(\omega,t)$ into Eq.(3.1), the generalized quantized field takes the form

$$\hat{\mathbf{E}}_{SPP}(r,t) = \sqrt{\frac{\hbar\omega}{2\epsilon_o V}}\hat{a}e^{i(kr-\omega t)} + \sqrt{\frac{\hbar\omega}{2\epsilon_o V}}\hat{a}^{\dagger}e^{-i(kr-\omega t)}. \tag{B.1}$$

# C Derivation of Hamiltonian

$$\hat{H}_F = \int \left|\hat{\mathbf{E}}_{SPP}(\omega,t)\right|^2 d^3r, \tag{C.1}$$

$$\hat{H}_M = \sum_n \hat{E}_n |n\rangle\langle n|, \tag{C.2a}$$

$$= \frac{E_e - E_g}{2}\big(|g\rangle\langle e| - |e\rangle\langle g|\big) - \frac{E_e - E_{g^*}}{2}\big(|g^*\rangle\langle e| - |e\rangle\langle g^*|\big), \tag{C.2b}$$

Following the interaction Hamiltonian takes the form,

$$\hat{H}_{Int} = \sum_{n=1}^{N} -\hat{d}.\hat{E}_n |n\rangle\langle n|. \tag{C.3}$$

In which, the dipole excited by incident electric field is defined by,

$$\hat{d} = \alpha.|\hat{\mathbf{E}}_{in}(\omega, t)|^2. \tag{C.4}$$

Where, polarizability is given by $\alpha = \frac{q^2}{\epsilon_0 m}\hat{b}$. Using Eq.C.4 into Eq.C.3 we find,

$$\hat{H}_{Int} = \frac{q^2}{\epsilon_0 m}\hat{b}.|\hat{\mathbf{E}}_{in}(\omega, t)|^2(\hat{\delta}^{i\dagger}_{eg} - \hat{\delta}^{i}_{eg}) + \frac{q^2}{\epsilon_0 m}\hat{b}^{\dagger}.|\hat{\mathbf{E}}^{*}_{in}(\omega, t)|^2(\hat{\delta}^{i\dagger}_{g^*e} - \hat{\delta}^{i}_{g^*e}), \tag{C.5}$$

# D Derivation of Equations of Evolution of Operators

Considering large time approximation ($\frac{d\hat{a}}{dt} \to 0$ for $t \to \infty$), Eqs. (3.12) and 3.13 rewritten as,

$$\hat{a} = \frac{-2ig}{\kappa - 2i\omega}\hat{\delta}^{i}_{eg}, \tag{D.1}$$

and

$$\hat{b} = \frac{-2g}{\kappa}\hat{\delta}^{i}_{g^*e}. \tag{D.2}$$

Applying the commutation relation of atomic operators, $[\hat{\delta}^i_{eg}, \hat{\delta}^{i\dagger}_{eg}] = \hat{\eta}^i_e$, $[\hat{\delta}^i_{eg}, \hat{\delta}^{i\dagger}_{g^*e}] = \hat{\eta}^i_{g'}$ and $[\hat{\delta}^i_{eg}, \hat{\delta}^i_{eg}] = [\hat{\delta}^i_{g^*e}, \hat{\delta}^i_{g^*e}] = 0$ we set evolution of atomic operators by,

$$\frac{d}{dt}\langle\hat{\delta}^i_{eg}\rangle = -i\Delta\big(\langle\hat{\eta}^i_e\rangle - \langle\hat{\eta}^i_g\rangle\big) + ig\big(\langle\hat{\eta}_e{}^i\hat{a}\rangle - \langle\hat{\eta}_g{}^i\hat{a}\rangle\big), \tag{D.3a}$$

$$\frac{d}{dt}\langle\hat{\delta}^i_{g^*e}\rangle = i\Delta\big(\langle\hat{\eta}^i_e\rangle - \langle\hat{\eta}^i_{g^*}\rangle\big) - ig\big(\langle\hat{\eta}_e{}^i\hat{b}\rangle - \langle\hat{\eta}^i_{g^*}\hat{b}\rangle\big), \tag{D.3b}$$

$$\frac{d}{dt}\langle\hat{\eta}^i_e\rangle = i\Delta\big(\langle\hat{\delta}^{i\dagger}_{eg}\rangle + \langle\hat{\delta}^i_{eg}\rangle - \langle\hat{\delta}^{i\dagger}_{g^*e}\rangle - \langle\hat{\delta}^i_{g^*e}\rangle\big) - ig\big(\langle\hat{\delta}^{i\dagger}_{eg}\hat{a}\rangle + \langle\hat{a}^\dagger\hat{\delta}^i_{eg}\rangle - \langle\hat{\delta}^{i\dagger}_{g^*e}\hat{b}\rangle - \langle\hat{b}^\dagger\hat{\delta}^i_{g^*e}\rangle\big), \tag{D.3c}$$

$$\frac{d}{dt}\langle\hat{\eta}^i_g\rangle = -i\Delta\big(\langle\hat{\delta}^{i\dagger}_{eg}\rangle + \langle\hat{\delta}^i_{eg}\rangle\big) + ig\big(\langle\hat{\delta}^{i\dagger}_{eg}\hat{a}\rangle + \langle\hat{a}^\dagger\hat{\delta}^i_{eg}\rangle\big), \tag{D.3d}$$

$$\frac{d}{dt}\langle\hat{\eta}^i_{g^*}\rangle = i\Delta\big(\langle\hat{\delta}^{i\dagger}_{g^*e}\rangle + \langle\hat{\delta}^i_{g^*e}\rangle\big) - ig\big(\langle\hat{\delta}^{i\dagger}_{g^*e}\hat{b}\rangle + \langle\hat{b}^\dagger\hat{\delta}^i_{g^*e}\rangle\big). \tag{D.3e}$$

Here, $\hat{\eta_e} = |e\rangle\langle e|$, $\hat{\eta_g} = |g\rangle\langle g|$ and $\hat{\eta_{g^*}} = |g^*\rangle\langle g^*|$ represent atom in top and bottom levels.

Introducing Eq.3.14 into Eqs.D.1 and (D.2) and summing three level atom over N we have,

$$\frac{d}{dt}\langle\hat{\delta}^i_{eg}\rangle = -i\Delta\big(\langle\hat{\eta}^i_e\rangle - \langle\hat{\eta}^i_g\rangle\big) - \frac{2ig^2}{\kappa - 2i\omega}\langle\hat{\delta}^i_{eg}\rangle. \tag{D.4}$$

Setting $\gamma_a = \frac{-2ig^2}{\kappa+2i\omega}$, $\gamma_b = \frac{-2ig^2}{\kappa}$, $\hat{X}_b = \sum_{i=1}^N \hat{\delta}^i_{eg^*}$, $\hat{Y}_a = \sum_{i=1}^N \hat{\eta}^i_e$, $\hat{Y}_b = \sum_{i=1}^N \hat{\eta}^i_g$, $\hat{Y}_c = \sum_{i=1}^N \hat{\eta}^i_{g^*}$ and $\hat{X}_a = \sum_{i=1}^N \hat{\delta}^i_{eg}$. we find,

$$\frac{d}{dt}\langle\hat{X}_a\rangle = -i\Delta\big(\langle\hat{Y}_a\rangle - \langle\hat{Y}_b\rangle\big) - i\gamma_a\langle\hat{X}_a\rangle. \tag{D.5}$$

Flowing the same procedure, we gate,

$$\frac{d}{dt}\langle\hat{X}_b\rangle = i\Delta\big(\langle\hat{Y}_a\rangle - \langle\hat{Y}_c\rangle\big) + i\gamma_b\langle\hat{X}_b\rangle, \tag{D.6a}$$

$$\frac{d}{dt}\langle\hat{Y}_a\rangle = i\Delta\big(\langle\hat{X}_a^\dagger\rangle + \langle\hat{X}_a\rangle - (\langle\hat{X}_b^\dagger\rangle + \langle\hat{X}_b\rangle)\big) + i2\gamma_a\langle\hat{Y}_b\rangle - 2\gamma_b\langle\hat{Y}_a\rangle), \tag{D.6b}$$

$$\frac{d}{dt}\langle\hat{Y}_b\rangle = -i\Delta\big(\langle\hat{X}_a^\dagger\rangle + \langle\hat{X}_a\rangle\big) - i2\gamma_a\langle\hat{Y}_b\rangle, \tag{D.6c}$$

$$\frac{d}{dt}\langle\hat{Y}_c\rangle = i\Delta\big(\langle\hat{X}_b^\dagger\rangle + \langle\hat{X}_b\rangle\big) + i2\gamma_b\langle\hat{Y}_a\rangle, \tag{D.6d}$$

From Eq. (D.3a) to Eq. (D.3d) we determine: $N = \langle\hat{Y}_a\rangle + \langle\hat{Y}_b\rangle + \langle\hat{Y}_c\rangle$ and $\hat{X}_a = N|e\rangle\langle g|$, $\hat{X}_b = N|e\rangle\langle g^*|$, $\hat{Y}_a = N|e\rangle\langle e|$, $\hat{Y}_b = N|g\rangle\langle g|$, $\hat{Y}_c = N|g^*\rangle\langle g^*|$. Then, Eq.(3.16) and (3.17c) takes the form

$$\frac{d}{dt}\hat{a} = -\frac{\kappa}{2}\hat{a} + \xi\hat{X}_a, \tag{D.7}$$

and

$$\frac{d}{dt}\hat{b} = -\frac{\kappa}{2}\hat{b} + \xi^*\hat{X}_b. \tag{D.8}$$

Taking large time approximation onto Eqs. (D.7) and . (D.8) we find,

$$\hat{a} = \frac{2\xi}{\kappa}\hat{X}_a, \tag{D.9}$$

and

$$\hat{b} = \frac{2\xi^*}{\kappa}\hat{X}_b. \tag{D.10}$$

Using commutation relation of Eqs. (D.9) and . (D.10) with its conjugate we have,

$$[\hat{a}, \hat{a}^\dagger] = \left(\frac{2\xi}{\kappa}\right)^2 N(\hat{Y}_a - \hat{Y}_b), \tag{D.11}$$

Similarly we have,

$$[\hat{b}, \hat{b}^\dagger] = \left(\frac{2\xi'}{\kappa}\right)^2 N(\hat{Y}_c - \hat{Y}_a). \tag{D.12}$$

The commutation relation of Eqs. (D.11) and . (D.12) with its complex conjugate gives,

$$[\hat{a}, \hat{a}^\dagger] = \left(\frac{-2ig^2}{\kappa - 2i\omega}\right)^2 (\hat{Y}_a - \hat{Y}_b), \tag{D.13}$$

and

$$[\hat{b}, \hat{b}^\dagger] = \left(\frac{-2ig^2}{\kappa}\right)^2 (\hat{Y}_c - \hat{Y}_a). \tag{D.14}$$

Equating Eq. (D.11) with Eq. (D.13) and Eq. (D.12) with (D.14) respectively gives,

$$\xi = \frac{g\kappa}{\sqrt{N}(\kappa - 2i\omega)}, \tag{D.15}$$

and

$$\xi^* = \frac{g}{\sqrt{N}}. \tag{D.16}$$

# List of Publications

Published Article

1. Alemayehu G. K. et al. Quantum Machine Learning Assisted Lung Cancer Telemedicine on AIP Advances. (2023)

2. Alemayehu G.K. et al. The quantum features of correlated photons with the effect of phase fluctuation on Ukrainian J. Phys., (2023).

3. Alemayehu G. K. et al. Optoplasmonic biosensor for lung cancer telediagnosis: Design and simulation analysis on Sensors Int., (2023).

4. Alemayehu G. K., Gemta, A. B., Desta, T. A. Kebede, A. Noble classical and quantum approach to model the optical properties of metallic nanoparticles to enhance the sensitivity of optoplasmonic sensors. RSC advances, (2022).

5. Hybridization of Plasmonic and Photonic Crystal for Effective Cancer Diagnosis: Recent Advances on Nanoscale Advances, (2023).

**Accepted Paper**

1. Computing Quantum machine learning Model for Biosignal Interpretation on Ukranian Journal of Physics

# A

# List of Conference

**In person**

1. Teleportation of Biosignal for Lung cancer Telediagnosis, presented at Adama Science and Technology University $4^{th}$ annual conference held on April 28-29, 2023.

2. Accurate optoplasmonic biosensor for lung cancer detection, presented at Addis Ababa University Second annual conference of CSESE held on January 4-5, 2023.

**On line**

1. Quantum properties of surface plasmon polariton, presented at ICTP held on September 19-20, 2022.

2. Spintronics for quantum repeaters application presented at International confirance on quantum information and quantum information science held on June 15, 2023.

# Bibliography


Aithal, P. (2023). Advances and new research opportunities in quantum computing technology by integrating it with other icct underlying technologies. *International Journal of Case Studies in Business, IT and Education (IJCSBE)*, 7(3):314–358.

Albahri, A. S., Alwan, J. K., Taha, Z. K., Ismail, S. F., Hamid, R. A., Zaidan, A., Albahri, O. S., Zaidan, B., Alamoodi, A. H., and Alsalem, M. (2021). Iot-based telemedicine for disease prevention and health promotion: State-of-the-art. *Journal of Network and Computer Applications*, 173:102873.

Ali, I. A. M., Ahmed, A. B., and Al-Ahmed, H. I. (2023). Green synthesis and characterization of silver nanoparticles for reducing the damage to sperm parameters in diabetic compared to metformin. *Scientific Reports*, 13(1):2256.

Alicki, R. (1989). Master equations for a damped nonlinear oscillator and the validity of the markovian approximation. *Physical Review A*, 40(7):4077.

Almawgani, A. H., Taya, S. A., Daher, M. G., Colak, I., Wu, F., and Patel, S. K. (2022). Detection of glucose concentration using a surface plasmon resonance biosensor based on barium titanate layers and molybdenum disulphide sheets. *Physica Scripta*, 97(6):065501.

Altintas, Z. and Tothill, I. (2013). Biomarkers and biosensors for the early diagnosis of lung cancer. *Sensors and Actuators B: Chemical*, 188:988–998.

Arora, I. and Tollefsbol, T. O. (2021). Computational methods and next-generation sequencing approaches to analyze epigenetics data: profiling of methods and applications. *Methods*, 187:92–103.

Arthurs, E. and Goodman, M. (1988). Quantum correlations: A generalized heisenberg uncertainty relation. *Physical review letters*, 60(24):2447.

Ashhab, S. (2022). Quantum state preparation protocol for encoding classical data into the amplitudes of a quantum information processing register's wave function. *Physical Review Research*, 4(1):013091.

Atesok, K., Tanaka, N., O'Brien, A., Robinson, Y., Pang, D., Deinlein, D., Manoharan, S. R., Pittman, J., and Theiss, S. (2018). Posttraumatic spinal cord injury without radiographic abnormality. *Advances in orthopedics*, 2018.

Awan, U., Hannola, L., Tandon, A., Goyal, R. K., and Dhir, A. (2022). Quantum computing challenges in the software industry. a fuzzy ahp-based approach. *Information and Software Technology*, 147:106896.

Azevedo, V., Silva, C., and Dutra, I. (2022). Quantum transfer learning for breast cancer detection. *Quantum Machine Intelligence*, 4(1):5.

Baghel, R., Maan, K., Haritwal, T., and Rana, P. (2021). Integration of epigenomics and metabolomics: From biomarkers discovery to personalized medicine. In *Epigenetics and Metabolomics*, pages 31–73. Elsevier.

Bainbridge, H., Salem, A., Tijssen, R. H., Dubec, M., Wetscherek, A., Van Es, C., Belderbos, J., Faivre-Finn, C., McDonald, F., et al. (2017). Magnetic resonance imaging in precision radiation therapy for lung cancer. *Translational lung cancer research*, 6(6):689.

Bastarrika, G., García-Velloso, M. J., Lozano, M. D., Montes, U., Torre, W., Spiteri, N., Campo, A., Seijo, L., Alcaide, A. B., Pueyo, J., et al. (2005). Early lung cancer detection using spiral computed tomography and positron emission tomography. *American journal of respiratory and critical care medicine*, 171(12):1378–1383.

Beechar, V. B., Prabhu, S. S., Bastos, D., Weinberg, J. S., Stafford, R. J., Fuentes, D., Hess, K. R., and Rao, G. (2018). Volumetric response of progressing post-srs

lesions treated with laser interstitial thermal therapy. *Journal of Neuro-oncology*, 137:57–65.

Bennett, C. H., Brassard, G., Crépeau, C., Jozsa, R., Peres, A., and Wootters, W. K. (1993). Teleporting an unknown quantum state via dual classical and einstein-podolsky-rosen channels. *Physical review letters*, 70(13):1895.

Björk, G. (2017). Information gain when measuring an unknown qubit. *European Journal of Physics*, 39(1):015403.

Blasone, M., Jizba, P., and Vitiello, G. (2003). Dissipation, emergent quantization, and quantum fluctuations. In *Decoherence and Entropy in Complex Systems: Selected Lectures from DICE 2002*, pages 151–163. Springer.

Blennow, K., Dubois, B., Fagan, A. M., Lewczuk, P., De Leon, M. J., and Hampel, H. (2015). Clinical utility of cerebrospinal fluid biomarkers in the diagnosis of early alzheimer's disease. *Alzheimer's & Dementia*, 11(1):58–69.

Boubertakh, B., Silvestri, C., and Di Marzo, V. (2022). Obesity: The fat tissue disease version of cancer. *Cells*, 11(12):1872.

Bourdine, A. V., Burdin, V. A., Janyani, V., Ghunawat, A. K., Singh, G., and Zhukov, A. E. (2018). Design of silica multimode optical fibers with extremely enlarged core diameter for laser-based multi-gigabit short-range optical networks. In *Photonics*, volume 5, page 37. MDPI.

Boutabba, N. and Eleuch, H. (2020). Quantum control of an optically dense atomic medium: Pulse shaping in a v-type three-level system. *Results in Physics*, 19:103421.

Bozinov, O., Yang, Y., Oertel, M. F., Neidert, M. C., and Nakaji, P. (2020). Laser interstitial thermal therapy in gliomas. *Cancer letters*, 474:151–157.

Bravin, A., Keyriläinen, J., Fernández, M., Fiedler, S., Nemoz, C., Karjalainen-Lindsberg, M.-L., Tenhunen, M., Virkkunen, P., Leidenius, M., Von Smitten, K.,

et al. (2007). High-resolution ct by diffraction-enhanced x-ray imaging: mapping of breast tissue samples and comparison with their histo-pathology. *Physics in Medicine & Biology*, 52(8):2197.

Budania, M., Verma, G., and Jeyakumar, A. (2020). Design and analysis of gtem cell using cst studio simulation. In *2020 IEEE International Conference on Electronics, Computing and Communication Technologies (CONECCT)*, pages 1–5. IEEE.

But, D., Mittendorff, M., Consejo, C., Teppe, F., Mikhailov, N., Dvoretskii, S., Faugeras, C., Winnerl, S., Helm, M., Knap, W., et al. (2019). Suppressed auger scattering and tunable light emission of landau-quantized massless kane electrons. *Nature Photonics*, 13(11):783–787.

Cacciapuoti, A. S., Caleffi, M., Van Meter, R., and Hanzo, L. (2020). When entanglement meets classical communications: Quantum teleportation for the quantum internet. *IEEE Transactions on Communications*, 68(6):3808–3833.

Cao, J., Zhai, L., and Guo, J.-L. (2022). Improving teleportation of quantum fisher information and fidelity for entangled state under decoherent channel. *International Journal of Theoretical Physics*, 61(2):22.

Cao, Y., Chen, J., Zhang, G., Fan, S., Ge, W., Hu, W., Huang, P., Hou, D., and Zheng, S. (2021). Characterization and discrimination of human colorectal cancer cells using terahertz spectroscopy. *Spectrochimica Acta Part A: Molecular and Biomolecular Spectroscopy*, 256:119713.

Cardia, A., Cannizzaro, D., Stefini, R., Chibbaro, S., Ganau, M., and Zaed, I. (2023). The efficacy of laser interstitial thermal therapy in the management of spinal metastases: a systematic review of the literature. *Neurological Sciences*, 44(2):519–528.

Casado, A., Guerra, S., Plácido, J., et al. (2010). Partial bell-state analysis with parametric down conversion in the wigner function formalism. *Advances in Mathematical Physics*, 2010.

Cetin, A. E., Coskun, A. F., Galarreta, B. C., Huang, M., Herman, D., Ozcan, A., and Altug, H. (2014). Handheld high-throughput plasmonic biosensor using computational on-chip imaging. *Light: Science & Applications*, 3(1):e122–e122.

Challis, L. (2005). Mechanisms for interaction between rf fields and biological tissue. *Bioelectromagnetics*, 26(S7):S98–S106.

Chang, C.-Y., Lin, H.-T., Lai, M.-S., Shieh, T.-Y., Peng, C.-C., Shih, M.-H., and Tung, Y.-C. (2018). Flexible localized surface plasmon resonance sensor with metal–insulator–metal nanodisks on pdms substrate. *Scientific reports*, 8(1):1–8.

Chen, J.-S., Chen, P.-F., Lin, H. T.-H., and Huang, N.-T. (2020). A localized surface plasmon resonance (lspr) sensor integrated automated microfluidic system for multiplex inflammatory biomarker detection. *Analyst*, 145(23):7654–7661.

Chen, M.-H., Hanagata, N., Ikoma, T., Huang, J.-Y., Li, K.-Y., Lin, C.-P., and Lin, F.-H. (2016). Hafnium-doped hydroxyapatite nanoparticles with ionizing radiation for lung cancer treatment. *Acta biomaterialia*, 37:165–173.

Chen, Y. (2013). Macroscopic quantum mechanics: theory and experimental concepts of optomechanics. *Journal of Physics B: Atomic, Molecular and Optical Physics*, 46(10):104001.

Childress, L., Taylor, J., Sørensen, A. S., and Lukin, M. (2006). Fault-tolerant quantum communication based on solid-state photon emitters. *Physical review letters*, 96(7):070504.

Chiu, N.-F., Lin, T.-L., and Kuo, C.-T. (2018). Highly sensitive carboxyl-graphene oxide-based surface plasmon resonance immunosensor for the detection of lung cancer for cytokeratin 19 biomarker in human plasma. *Sensors and Actuators B: Chemical*, 265:264–272.

Collins, C. M. and Wang, Z. (2011). Calculation of radiofrequency electromagnetic fields and their effects in mri of human subjects. *Magnetic resonance in medicine*, 65(5):1470–1482.

Combes, J., Kerckhoff, J., and Sarovar, M. (2017). The slh framework for modeling quantum input-output networks. *Advances in Physics: X*, 2(3):784–888.

Córcoles, A. D., Kandala, A., Javadi-Abhari, A., McClure, D. T., Cross, A. W., Temme, K., Nation, P. D., Steffen, M., and Gambetta, J. M. (2019). Challenges and opportunities of near-term quantum computing systems. *Proceedings of the IEEE*, 108(8):1338–1352.

Creighton, J. A., Blatchford, C. G., and Albrecht, M. G. (1979). Plasma resonance enhancement of raman scattering by pyridine adsorbed on silver or gold sol particles of size comparable to the excitation wavelength. *Journal of the Chemical Society, Faraday Transactions 2: Molecular and Chemical Physics*, 75:790–798.

Daniels, J. K. and Chumanov, G. (2005). Nanoparticle- mirror sandwich substrates for surface-enhanced raman scattering. *The Journal of Physical Chemistry B*, 109(38):17936–17942.

Das, R., Mitra, M., and Singh, C. (2023). *Era of Artificial Intelligence: The 21st Century Practitioners' Approach*. CRC Press.

Díaz-Santos, S. and Escanez-Exposito, D. (2023). Classical vs. quantum machine learning for breast cancer detection. In *2023 19th International Conference on the Design of Reliable Communication Networks (DRCN)*, pages 1–5. IEEE.

Doria-Rose, V. P., Marcus, P. M., Szabo, E., Tockman, M. S., Melamed, M. R., and Prorok, P. C. (2009). Randomized controlled trials of the efficacy of lung cancer screening by sputum cytology revisited: a combined mortality analysis from the johns hopkins lung project and the memorial sloan-kettering lung study. *Cancer: Interdisciplinary International Journal of the American Cancer Society*, 115(21):5007–5017.

El Anouz, K., El Aouadi, I., El Allati, A., and Mourabit, T. (2020). Dynamics of quantum correlations in quantum teleportation. *International Journal of Modern Physics B*, 34(10):2050093.

El-Hussein, A., Manoto, S. L., Ombinda-Lemboumba, S., Alrowaili, Z. A., and Mthunzi-Kufa, P. (2021). A review of chemotherapy and photodynamic therapy for lung cancer treatment. *Anti-Cancer Agents in Medicinal Chemistry (Formerly Current Medicinal Chemistry-Anti-Cancer Agents)*, 21(2):149–161.

Eriksen, E. (1968). Properties of higher-order commutator products and the baker-hausdorff formula. *Journal of Mathematical Physics*, 9(5):790–796.

Fano, U. (1941). The theory of anomalous diffraction gratings and of quasi-stationary waves on metallic surfaces (sommerfeld's waves). *JOSA*, 31(3):213–222.

Fazio, B., Irrera, A., Pirotta, S., D'Andrea, C., Del Sorbo, S., Josè Lo Faro, M., Gucciardi, P. G., Iati, M. A., Saija, R., Patrini, M., et al. (2017). Coherent backscattering of raman light. *Nature Photonics*, 11(3):170–176.

Fernandez-Corbaton, I., Zambrana-Puyalto, X., Tischler, N., Vidal, X., Juan, M. L., and Molina-Terriza, G. (2013). Electromagnetic duality symmetry and helicity conservation for the macroscopic maxwell's equations. *Physical review letters*, 111(6):060401.

Fischer, G. S., Iordachita, I., Csoma, C., Tokuda, J., DiMaio, S. P., Tempany, C. M., Hata, N., and Fichtinger, G. (2008). Mri-compatible pneumatic robot for transperineal prostate needle placement. *IEEE/ASME transactions on mechatronics*, 13(3):295–305.

Ford, G. W., Lewis, J. T., and O'Connell, R. (1988). Quantum langevin equation. *Physical Review A*, 37(11):4419.

Forrest, L. F., Adams, J., Wareham, H., Rubin, G., and White, M. (2013). Socioeconomic inequalities in lung cancer treatment: systematic review and meta-analysis. *PLoS medicine*, 10(2):e1001376.

Frankell, A. M., Dietzen, M., Al Bakir, M., Lim, E. L., Karasaki, T., Ward, S., Veeriah,

S., Colliver, E., Huebner, A., Bunkum, A., et al. (2023). The evolution of lung cancer and impact of subclonal selection in tracerx. *Nature*, pages 1–9.

Fröhlich, B., Lucamarini, M., Dynes, J. F., Comandar, L. C., Tam, W. W.-S., Plews, A., Sharpe, A. W., Yuan, Z., and Shields, A. J. (2017). Long-distance quantum key distribution secure against coherent attacks. *Optica*, 4(1):163–167.

Fröwis, F., Sekatski, P., Dür, W., Gisin, N., and Sangouard, N. (2018). Macroscopic quantum states: Measures, fragility, and implementations. *Reviews of Modern Physics*, 90(2):025004.

Furusawa, A. and Van Loock, P. (2011). *Quantum teleportation and entanglement: a hybrid approach to optical quantum information processing*. John Wiley & Sons.

Gangareddy, J., Bheemaiah, E., Gandhiraj, V., James, J. T., Jose, J. K., Katturi Naga, K., and Soma, V. R. (2018). Nonlinear optical studies of sodium borate glasses embedded with gold nanoparticles. *Applied Physics B*, 124:1–9.

Giannini, V., Fernández-Domínguez, A. I., Sonnefraud, Y., Roschuk, T., Fernández-García, R., and Maier, S. A. (2010). Controlling light localization and light–matter interactions with nanoplasmonics. *small*, 6(22):2498–2507.

Gohagan, J. K., Marcus, P. M., Fagerstrom, R. M., Pinsky, P. F., Kramer, B. S., Prorok, P. C., Ascher, S., Bailey, W., Brewer, B., Church, T., et al. (2005). Final results of the lung screening study, a randomized feasibility study of spiral ct versus chest x-ray screening for lung cancer. *Lung cancer*, 47(1):9–15.

Gordillo, N., Montseny, E., and Sobrevilla, P. (2013). State of the art survey on mri brain tumor segmentation. *Magnetic resonance imaging*, 31(8):1426–1438.

Graniel, O., Weber, M., Balme, S., Miele, P., and Bechelany, M. (2018). Atomic layer deposition for biosensing applications. *Biosensors and Bioelectronics*, 122:147–159.

Grover, V. P., Tognarelli, J. M., Crossey, M. M., Cox, I. J., Taylor-Robinson, S. D., and McPhail, M. J. (2015). Magnetic resonance imaging: principles and techniques: lessons for clinicians. *Journal of clinical and experimental hepatology*, 5(3):246–255.

Güneş, F., Aykaç, A., Erol, M., Erdem, Ç., Hano, H., Uzunbayir, B., Şen, M., and Erdem, A. (2022). Synthesis of hierarchical hetero-composite of graphene foam/$\alpha$-fe2o3 nanowires and its application on glucose biosensors. *Journal of Alloys and Compounds*, 895:162688.

Gupta, S., Modgil, S., Bhatt, P. C., Jabbour, C. J. C., and Kamble, S. (2023). Quantum computing led innovation for achieving a more sustainable covid-19 healthcare industry. *Technovation*, 120:102544.

Haes, A. J., Hall, W. P., Chang, L., Klein, W. L., and Van Duyne, R. P. (2004). A localized surface plasmon resonance biosensor: First steps toward an assay for alzheimer's disease. *Nano letters*, 4(6):1029–1034.

Haleem, A., Javaid, M., Singh, R. P., and Suman, R. (2021). Telemedicine for healthcare: Capabilities, features, barriers, and applications. *Sensors International*, 2:100117.

Hannay, J. (1983). The clausius-mossotti equation: an alternative derivation. *European Journal of Physics*, 4(3):141.

He, L., Dai, D., Xie, L., Chen, Y., and Zhang, C. (2021). Biological effects, applications and strategies of nanomodification of dental metal surfaces. *Materials & Design*, 207:109890.

Hill, R. T. (2015). Plasmonic biosensors. *Wiley Interdisciplinary Reviews: Nanomedicine and Nanobiotechnology*, 7(2):152–168.

Ho, L.-J., Yang, H.-Y., Chung, C.-H., Chang, W.-C., Yang, S.-S., Sun, C.-A., Chien, W.-C., and Su, R.-Y. (2021). Increased risk of secondary lung cancer in patients

with tuberculosis: a nationwide, population-based cohort study. *PLoS One*, 16(5):e0250531.

Hofmann, T., Yu, T. H., Folse, M., Weinhardt, L., Bar, M., Zhang, Y., Merinov, B. V., Myers, D. J., Goddard III, W. A., and Heske, C. (2012). Using photoelectron spectroscopy and quantum mechanics to determine d-band energies of metals for catalytic applications. *The Journal of Physical Chemistry C*, 116(45):24016–24026.

Hossain, B., Paul, A. K., Islam, M. A., Rahman, M. M., Sarkar, A. K., and Abdulrazak, L. F. (2022). A highly sensitive surface plasmon resonance biosensor using snse allotrope and heterostructure of bluep/mos2 for cancerous cell detection. *Optik*, 252:168506.

Hossain, M. B., Akib, T. B. A., Abdulrazak, L. F., and Rana, M. M. (2019). Numerical modeling of graphene-coated fiber optic surface plasmon resonance biosensor for brca1 and brca2 genetic breast cancer detection. *Optical Engineering*, 58(3):037104.

How, M.-L. and Cheah, S.-M. (2023). Business renaissance: Opportunities and challenges at the dawn of the quantum computing era. *Businesses*, 3(4):585–605.

Hu, M.-L., Yang, Z.-J., Du, X.-J., and He, J. (2021). Towards strong linear and nonlinear light-matter interactions in hybrid nanostructures of a single molecule and a plasmonic nanocavity. *Physical Review B*, 104(6):064311.

Huang, L., Liang, F., Feng, Y., Zhao, P., and Wang, W. (2020). On-chip integrated optical stretching and electrorotation enabling single-cell biophysical analysis. *Microsystems & Nanoengineering*, 6(1):1–14.

Huang, Z.-M., Huang, W.-Q., Liu, S.-R., Dong, T.-G., Wang, G., Wu, X.-K., Han, Z.-R., and Qin, C.-J. (2017). Enhanced emission in the three-level system of si and ge nanostructures. *Optics Communications*, 383:1–5.

Huo, M., Qin, J., Cheng, J., Yan, Z., Qin, Z., Su, X., Jia, X., Xie, C., and Peng, K. (2018). Deterministic quantum teleportation through fiber channels. *Science advances*, 4(10):eaas9401.

Inamura, K. (2017). Lung cancer: understanding its molecular pathology and the 2015 who classification. *Frontiers in oncology*, 7:193.

Iurov, A. and Gumbs, G. A. (2013). Conference 8749: Quantum information and computation xi. *Defense Security+ Sensing*, 16:408.

Jabin, M. A., Ahmed, K., Rana, M. J., Paul, B. K., Islam, M., Vigneswaran, D., and Uddin, M. S. (2019). Surface plasmon resonance based titanium coated biosensor for cancer cell detection. *IEEE Photonics Journal*, 11(4):1–10.

Jain, P. K., Huang, X., El-Sayed, I. H., and El-Sayed, M. A. (2008). Noble metals on the nanoscale: optical and photothermal properties and some applications in imaging, sensing, biology, and medicine. *Accounts of chemical research*, 41(12):1578–1586.

Jaynes, E. T. and Cummings, F. W. (1963). Comparison of quantum and semiclassical radiation theories with application to the beam maser. *Proceedings of the IEEE*, 51(1):89–109.

Jha, M., Gupta, R., and Saxena, R. (2020). A review on non-invasive biosensors for early detection of lung cancer. In *2020 6th International Conference on Signal Processing and Communication (ICSC)*, pages 162–166. IEEE.

Jiang, Y., Mei, Y., and Du, S. (2023). Quantum langevin theory for two coupled phase-conjugated electromagnetic waves. *Physical Review A*, 107(5):053703.

Joarder, R. and Crundwell, N. (2009). *Chest X-ray in clinical practice*. Springer Science & Business Media.

Jongen, N., Bowen, P., Lemaître, J., Valmalette, J.-C., and Hofmann, H. (2000). Precipitation of self-organized copper oxalate polycrystalline particles in the

presence of hydroxypropylmethylcellulose (hpmc): control of morphology. *Journal of Colloid and Interface Science*, 226(2):189–198.

Kais, G. and Hamdi, Y. (2022). Introductory chapter: Application of bioinformatics tools in cancer prevention, screening, and diagnosis. *Cancer Bioinformatics*, page 3.

Kamel, H. F. M. and Al-Amodi, H. S. A. B. (2017). Exploitation of gene expression and cancer biomarkers in paving the path to era of personalized medicine. *Genomics, proteomics & bioinformatics*, 15(4):220–235.

Kandala, A., Temme, K., Córcoles, A. D., Mezzacapo, A., Chow, J. M., and Gambetta, J. M. (2019). Error mitigation extends the computational reach of a noisy quantum processor. *Nature*, 567(7749):491–495.

Kantner, M., Mittnenzweig, M., and Koprucki, T. (2018). A hybrid quantum-classical modeling approach for electrically driven quantum light sources. In *Physics and Simulation of Optoelectronic Devices XXVI*, volume 10526, page 1052603. SPIE.

Kargbo, R. B. (2022). Kras inhibitors and target engagement technology: From undruggable to druggable targets in cancer therapeutics.

Karki, B., Pal, A., Singh, Y., and Sharma, S. (2022a). Sensitivity enhancement of surface plasmon resonance sensor using 2d material barium titanate and black phosphorus over the bimetallic layer of au, ag, and cu. *Optics Communications*, 508:127616.

Karki, B., Uniyal, A., Chauhan, B., and Pal, A. (2022b). Sensitivity enhancement of a graphene, zinc sulfide-based surface plasmon resonance biosensor with an ag metal configuration in the visible region. *Journal of Computational Electronics*, 21(2):445–452.

Kauranen, M. and Persoons, A. (1996). Theory of polarization measurements

of second-order nonlinear light scattering. *The Journal of chemical physics*, 104(10):3445–3456.

Khulbe, M. (2023). Simulation of a plasmonic sensor using kinetic theory of plasma with the vlasov equation in matlab. *Journal of Optics*, 25(7):075001.

Kiilerich, A. H. and Mølmer, K. (2019). Input-output theory with quantum pulses. *Physical review letters*, 123(12):123604.

Kim, C. and Kumar, P. (1994). Quadrature-squeezed light detection using a self-generated matched local oscillator. *Physical review letters*, 73(12):1605.

Kim, J., Jang, H., Kim, D., and Lee, J. (2022). Exploration of the virtual reality teleportation methods using hand-tracking, eye-tracking, and eeg. *International Journal of Human–Computer Interaction*, pages 1–14.

Kira, M. and Koch, S. W. (2011). *Semiconductor quantum optics*. Cambridge University Press.

Kirdi, M. E., Slaoui, A., Hadfi, H. E., and Daoud, M. (2023). Improving the probabilistic quantum teleportation efficiency of arbitrary superposed coherent state using multipartite even and odd j-spin coherent states as resource. *Applied Physics B*, 129(6):94.

Kish, L. B. (2023). 'quantum supremacy'revisited: low-complexity, deterministic solutions of the original deutsch–jozsa problem in classical physical systems. *Royal Society Open Science*, 10(3):221327.

Koh, E. H., Lee, W.-C., Choi, Y.-J., Moon, J.-I., Jang, J., Park, S.-G., Choo, J., Kim, D.-H., and Jung, H. S. (2021). A wearable surface-enhanced raman scattering sensor for label-free molecular detection. *ACS Applied Materials & Interfaces*, 13(2):3024–3032.

Koniorczyk, M., Kiss, T., and Janszky, J. (2001). Teleportation: from probability distributions to quantum states. *Journal of Physics A: Mathematical and General*, 34(35):6949.

Kretschmann, E. and Raether, H. (1968). Radiative decay of non radiative surface plasmons excited by light. *Zeitschrift für Naturforschung A*, 23(12):2135–2136.

Kumela, A. G., Gemta, A. B., Desta, T. A., and Kebede, A. (2022a). Noble classical and quantum approach to model the optical properties of metallic nanoparticles to enhance the sensitivity of optoplasmonic sensors. *RSC advances*, 12(25):16203–16214.

Kumela, A. G., Gemta, A. B., Desta, T. A., and Kebede, A. (2022b). Noble classical and quantum approach to model the optical properties of metallic nanoparticles to enhance the sensitivity of optoplasmonic sensors. *RSC Adv.*, 12:16203–16214.

Kumela, A. G., Gemta, A. B., Hordofa, A. K., Dagnaw, H., Sheferedin, U., and Tadesse, M. (2023a). Quantum machine learning assisted lung cancer telemedicine. *AIP Advances*, 13(7).

Kumela, A. G., Gemta, A. B., Hordofa, A. K., Desta, T. A., Dangish, M., and Mekonnen, H. D. (2023b). Optoplasmonic biosensor for lung cancer telediagnosis: Design and simulation analysis. *Sensors International*, 4:100232.

Lahham, A., Issa, A., and ALMasri, H. (2018). Patient radiation dose from chest x-ray examinations in the west bank—palestine. *Radiation protection dosimetry*, 178(3):298–303.

Lamb, H. (1904). I. on the propagation of tremors over the surface of an elastic solid. *Philosophical Transactions of the Royal Society of London. Series A, Containing papers of a mathematical or physical character*, 203(359-371):1–42.

Lambert, R. G., Hermann, K. G. A., and Diekhoff, T. (2021). Low-dose computed tomography for axial spondyloarthritis: update on use and limitations. *Current Opinion in Rheumatology*, 33(4):326–332.

Lawrie, B. J., Lett, P. D., Marino, A. M., and Pooser, R. C. (2019). Quantum sensing with squeezed light. *Acs Photonics*, 6(6):1307–1318.

Lemjabbar-Alaoui, H., Hassan, O. U., Yang, Y.-W., and Buchanan, P. (2015). Lung cancer: Biology and treatment options. *Biochimica et Biophysica Acta (BBA)-Reviews on Cancer*, 1856(2):189–210.

Li, B., Cheng, T., Chen, J., and Yan, X. (2019). Graphene-enhanced surface plasmon resonance liquid refractive index sensor based on photonic crystal fiber. *Sensors*, 19(17):3666.

Li, D., Deng, C., Fu, F., Bai, J., Li, Y., Zhang, Y., and Chen, H. (2023). Impact of prior cancer history on outcomes of resected lung cancer. *Annals of surgical oncology*, pages 1–7.

Li, F., Shen, J., Guan, C., Xie, Y., Wang, Z., Lin, S., Chen, J., and Zhu, J. (2022). Exploring near-field sensing efficiency of complementary plasmonic metasurfaces for immunodetection of tumor markers. *Biosensors and Bioelectronics*, 203:114038.

Li, L., Yang, W.-X., Shui, T., and Wang, X. (2020). Ultrasensitive sizing sensor for a single nanoparticle in a hybrid nonlinear microcavity. *IEEE Photonics Journal*, 12(3):1–8.

Lin, C., Li, Y., Peng, Y., Zhao, S., Xu, M., Zhang, L., Huang, Z., Shi, J., and Yang, Y. (2023). Recent development of surface-enhanced raman scattering for biosensing. *Journal of Nanobiotechnology*, 21(1):149.

Liou, Y.-R., Torng, W., Kao, Y.-C., Sung, K.-B., Lee, C.-H., and Kuo, P.-L. (2014). Substrate stiffness regulates filopodial activities in lung cancer cells. *PLoS One*, 9(2):e89767.

Liu, C., Zeng, X., An, Z., Yang, Y., Eisenbaum, M., Gu, X., Jornet, J. M., Dy, G. K., Reid, M. E., Gan, Q., et al. (2018a). Sensitive detection of exosomal proteins via a compact surface plasmon resonance biosensor for cancer diagnosis. *ACS sensors*, 3(8):1471–1479.

Liu, J., Gao, H., Wang, J., He, Y., Lu, X., Cheng, Z., and Wu, S. (2023). Recent research

advances on simulation modeling of temperature distribution in microwave ablation of lung tumors. *Computer Assisted Surgery*, 28(1):2195078.

Liu, J., Lovrenski, J., Ye Hlaing, A., and Kurepa, D. (2021). Neonatal lung diseases: lung ultrasound or chest x-ray. *The Journal of Maternal-Fetal & Neonatal Medicine*, 34(7):1177–1182.

Liu, S., Su, W., Li, Y., Zhang, L., and Ding, X. (2018b). Manufacturing of an electrochemical biosensing platform based on hybrid dna hydrogel: Taking lung cancer-specific mir-21 as an example. *Biosensors and Bioelectronics*, 103:1–5.

Liu, Y., Liu, Q., Chen, S., Cheng, F., Wang, H., and Peng, W. (2015). Surface plasmon resonance biosensor based on smart phone platforms. *Scientific reports*, 5(1):1–9.

Llopis-Cardona, F., Armero, C., and Sanfélix-Gimeno, G. (2023). Estimating disease incidence rates and transition probabilities in elderly patients using multi-state models: a case study in fragility fracture using a bayesian approach. *BMC Medical Research Methodology*, 23(1):40.

Luo, Y.-H., Chen, M.-C., Erhard, M., Zhong, H.-S., Wu, D., Tang, H.-Y., Zhao, Q., Wang, X.-L., Fujii, K., Li, L., et al. (2021). Quantum teleportation of physical qubits into logical code spaces. *Proceedings of the National Academy of Sciences*, 118(36):e2026250118.

MacDonald, D. (1952). Properties of metals at low temperatures. *Progress in Metal Physics*, 3:42–75.

Madureira, J. R., Vasconcellos, A. R., Luzzi, R., Casas-Vázquez, J., and Jou, D. (1998). Evolution of dissipative processes via a statistical thermodynamic approach. i. generalized mori–heisenberg–langevin equations. *The Journal of chemical physics*, 108(18):7568–7579.

Maheshwari, D., Garcia-Zapirain, B., and Sierra-Sosa, D. (2022). Quantum machine learning applications in the biomedical domain: A systematic review. *Ieee Access*.

Malik, H. and Anees, T. (2022). Bdcnet: Multi-classification convolutional neural network model for classification of covid-19, pneumonia, and lung cancer from chest radiographs. *Multimedia Systems*, 28(3):815–829.

Mataji-Kojouri, A., Ozen, M. O., Shahabadi, M., Inci, F., and Demirci, U. (2020). Entangled nanoplasmonic cavities for estimating thickness of surface-adsorbed layers. *ACS nano*, 14(7):8518–8527.

Matiatou, M., Giannios, P., Koutsoumpos, S., Toutouzas, K. G., Zografos, G. C., and Moutzouris, K. (2021). Data on the refractive index of freshly-excised human tissues in the visible and near-infrared spectral range. *Results in Physics*, 22:103833.

Matsubara, N., Teramoto, A., Saito, K., and Fujita, H. (2020). Bone suppression for chest x-ray image using a convolutional neural filter. *Physical and Engineering Sciences in Medicine*, 43:97–108.

McClements, D. J. and Gumus, C. E. (2016). Natural emulsifiers—biosurfactants, phospholipids, biopolymers, and colloidal particles: Molecular and physicochemical basis of functional performance. *Advances in Colloid and interface Science*, 234:3–26.

McCoy, D. E., Shneidman, A. V., Davis, A. L., and Aizenberg, J. (2021). Finite-difference time-domain (fdtd) optical simulations: a primer for the life sciences and bio-inspired engineering. *Micron*, 151:103160.

Mervak, B. M., Wilson, S. B., Handly, B. D., Altun, E., and Burke, L. M. (2019). Mri of acute appendicitis. *Journal of Magnetic Resonance Imaging*, 50(5):1367–1376.

Mohr, N. M., Young, T., Harland, K. K., Skow, B., Wittrock, A., Bell, A., and Ward, M. M. (2019). Telemedicine is associated with faster diagnostic imaging in stroke patients: a cohort study. *Telemedicine and e-Health*, 25(2):93–100.

Moosmüller, H., Giri, R., Sorensen, C. M., and Berg, M. J. (2021). Black metal

nanoparticles from abrasion processes in everyday life: Bicycle drivetrains and rock-climbing ropes. *Optics Communications*, 479:126413.

Motogaito, A., Nakamura, S., Miyazaki, J., Miyake, H., and Hiramatsu, K. (2015). Using surface-plasmon polariton at the gap-au interface in order to detect chemical species in high-refractive-index media. *Optics Communications*, 341:64–68.

Nangare, S. and Patil, P. (2023). Black phosphorus nanostructure based highly sensitive and selective surface plasmon resonance sensor for biological and chemical sensing: a review. *Critical Reviews in Analytical Chemistry*, 53(1):1–26.

Narla, A., Shankar, S., Hatridge, M., Leghtas, Z., Sliwa, K. M., Zalys-Geller, E., Mundhada, S. O., Pfaff, W., Frunzio, L., Schoelkopf, R. J., et al. (2016). Robust concurrent remote entanglement between two superconducting qubits. *Physical Review X*, 6(3):031036.

Nazir, M., Shakil, S., and Khurshid, K. (2021). Role of deep learning in brain tumor detection and classification (2015 to 2020): A review. *Computerized Medical Imaging and Graphics*, 91:101940.

Neha, K. et al. (2023). Quantum programming: Working with ibm's qiskit tool. *The Scientific Temper*, 14(01):93–99.

Nevraumont, A., Deltombe, M., Favresse, J., Guillaume, L., Chapelle, V., Twerenbold, R., and Gruson, D. (2022). Interferences with cardiac biomarker assays: understanding the clinical impact.

Nicoletti, D. and Cavalleri, A. (2016). Nonlinear light–matter interaction at terahertz frequencies. *Advances in Optics and Photonics*, 8(3):401–464.

Ofiara, L. M., Navasakulpong, A., Beaudoin, S., and Gonzalez, A. V. (2014). Optimizing tissue sampling for the diagnosis, subtyping, and molecular analysis of lung cancer. *Frontiers in oncology*, 4:253.

OMODELE, A. D., HALIMAT, B. A., and INIOLUWA, A. V. (2023). Chemical analysis by laser-based raman spectroscopy.

Otto, A. (1968). Excitation of nonradiative surface plasma waves in silver by the method of frustrated total reflection. *Zeitschrift für Physik A Hadrons and nuclei*, 216(4):398–410.

Ouyang, Q., Zeng, S., Jiang, L., Hong, L., Xu, G., Dinh, X.-Q., Qian, J., He, S., Qu, J., Coquet, P., et al. (2016). Sensitivity enhancement of transition metal dichalcogenides/silicon nanostructure-based surface plasmon resonance biosensor. *Scientific reports*, 6(1):28190.

Pandey, A. K., Sharma, A. K., and Marques, C. (2020). On the application of sio2/sic grating on ag for high-performance fiber optic plasmonic sensing of cortisol concentration. *Materials*, 13(7):1623.

Pang, S., Kapur, A., Zhou, K., Anastasiadis, P., Ballirano, N., Kim, A. J., Winkles, J. A., Woodworth, G. F., and Huang, H.-C. (2022). Nanoparticle-assisted, image-guided laser interstitial thermal therapy for cancer treatment. *Wiley Interdisciplinary Reviews: Nanomedicine and Nanobiotechnology*, 14(5):e1826.

PAPAIOANNOU, A. N. and FRANCIS, K. C. (1965). 14 scapulectomy for the treatment of primary malignant tumors of the scapula. *Clinical Orthopaedics and Related Research®*, 41:125–132.

Paydar, R., Takavar, A., Kardan, M., Babakhani, A., Deevband, M., and Saber, S. (2012). Patient effective dose evaluation for chest x-ray examination in three digital radiography centers. *International Journal of Radiation Research*, 10(3/4):139.

Pazzi, A. A., Vij, P., Salhadar, N., George, E., and Tripathi, M. K. (2023). A new era of rna personalized vaccines for cancer and cancer-causing infectious diseases. In *RNA Therapeutics-History, Design, Manufacturing, and Applications*. IntechOpen.

Phillips, M., Altorki, N., Austin, J. H., Cameron, R. B., Cataneo, R. N., Kloss, R., Maxfield, R. A., Munawar, M. I., Pass, H. I., Rashid, A., et al. (2008). Detection of lung cancer using weighted digital analysis of breath biomarkers. *Clinica chimica acta*, 393(2):76–84.

Pietzner, M., Chua, R. L., Wheeler, E., Jechow, K., Willett, J. D., Radbruch, H., Trump, S., Heidecker, B., Zeberg, H., Heppner, F. L., et al. (2022). Elf5 is a potential respiratory epithelial cell-specific risk gene for severe covid-19. *Nature communications*, 13(1):1–15.

Pirandola, S., Eisert, J., Weedbrook, C., Furusawa, A., and Braunstein, S. L. (2015). Advances in quantum teleportation. *Nature photonics*, 9(10):641–652.

Polavarapu, L., Porta, A. L., Novikov, S. M., Coronado-Puchau, M., and Liz-Marzán, L. M. (2014). Pen-on-paper approach toward the design of universal surface enhanced raman scattering substrates. *Small*, 10(15):3065–3071.

Pourkarimi, M. R. and Rahnama, M. (2014). Quantum teleportation under the effect of dissipative environment and hamiltonian xy model. *International Journal of Theoretical Physics*, 53:1415–1423.

Prabhakar, B., Shende, P., and Augustine, S. (2018). Current trends and emerging diagnostic techniques for lung cancer. *Biomedicine & Pharmacotherapy*, 106:1586–1599.

Puiu, M. and Bala, C. (2016). Spr and spr imaging: Recent trends in developing nanodevices for detection and real-time monitoring of biomolecular events. *Sensors*, 16(6):870.

Purcell, E., Pound, R., and Bloembergen, N. (1946). Nuclear magnetic resonance absorption in hydrogen gas. *Physical Review*, 70(11-12):986.

Retzker, A., Solano, E., and Reznik, B. (2007). Tavis-cummings model and collective multiqubit entanglement in trapped ions. *Physical Review A*, 75(2):022312.

Rice, P. R. and Carmichael, H. (1994). Photon statistics of a cavity-qed laser: A comment on the laser–phase-transition analogy. *Physical Review A*, 50(5):4318.

Rich, R. L. and Myszka, D. G. (2000). Advances in surface plasmon resonance biosensor analysis. *Current opinion in biotechnology*, 11(1):54–61.

Richards, D., Stirling, W., and Ellis, S. (1982). Second order corrections to the energy-energy correlation function in quantum chromodynamics. *Physics Letters B*, 119(1-3):193–197.

Roch, B., Coffy, A., Jean-Baptiste, S., Palaysi, E., Daures, J.-P., Pujol, J.-L., and Bommart, S. (2020). Cachexia-sarcopenia as a determinant of disease control rate and survival in non-small lung cancer patients receiving immune-checkpoint inhibitors. *Lung Cancer*, 143:19–26.

Rodriguez-Canales, J., Parra-Cuentas, E., and Wistuba, I. I. (2016). Diagnosis and molecular classification of lung cancer. *Lung Cancer: Treatment and Research*, pages 25–46.

Röntgen, W. C. (1896). On a new kind of rays. *Science*, 3(59):227–231.

Roughton, J. (1982). Non-invasive measurements. *Journal of Physics E: Scientific Instruments*, 15(12):1257.

Roy, P. and Saikia, B. (2016). Cancer and cure: A critical analysis. *Indian journal of cancer*, 53(3):441–442.

Ruggenthaler, M., Penz, M., and Bauer, D. (2010). General runge-gross-type theorem for dipole laser-matter interaction. *Physical Review A*, 81(6):062108.

Ruggenthaler, M., Tancogne-Dejean, N., Flick, J., Appel, H., and Rubio, A. (2018). From a quantum-electrodynamical light–matter description to novel spectroscopies. *Nature Reviews Chemistry*, 2(3):1–16.

Sakulkhu, U., Mahmoudi, M., Maurizi, L., Coullerez, G., Hofmann-Amtenbrink, M., Vries, M., Motazacker, M., Rezaee, F., and Hofmann, H. (2015). Significance of surface charge and shell material of superparamagnetic iron oxide nanoparticle (spion) based core/shell nanoparticles on the composition of the protein corona. *Biomaterials science*, 3(2):265–278.

Samanta, D., Singh, R., Gedela, S., Perry, M. S., and Arya, R. (2021). Underutilization of epilepsy surgery: Part ii: Strategies to overcome barriers. *Epilepsy & Behavior*, 117:107853.

Schick, F. (2005). Whole-body mri at high field: technical limits and clinical potential. *European radiology*, 15:946–959.

Schulte, C. H., Hansom, J., Jones, A. E., Matthiesen, C., Le Gall, C., and Atatüre, M. (2015). Quadrature squeezed photons from a two-level system. *Nature*, 525(7568):222–225.

Schuurmans, M. and Van Dijk, J. (1984). On radiative and non-radiative decay times in the weak coupling limit. *Physica B+ C*, 123(2):131–155.

Scott, B. (2019). *Elements of Quantum Optics*. Scientific e-Resources.

Selenica, P., Marra, A., Choudhury, N., Gazzo, A., Falcon, C., Patel, J., Pei, X., Zhu, Y., Ng, C., Curry, M., et al. (2022). Apobec mutagenesis, kataegis, chromothripsis in egfr-mutant osimertinib-resistant lung adenocarcinomas. *Annals of oncology*, 33(12):1284–1295.

Sergi, C. M. (2019). Digital pathology: the time is now to bridge the gap between medicine and technological singularity. *Interactive Multimedia-Multimedia Production and Digital Storytelling*.

Shams, M., Choudhari, J., Reyes, K., Prentzas, S., Gapizov, A., Shehryar, A., Affaf, M., Grezenko, H., Gasim, R. W., Mohsin, S. N., et al. (2023). The quantum-medical nexus: Understanding the impact of quantum technologies on healthcare. *Cureus*, 15(10).

Shankar, A., Saini, D., Dubey, A., Roy, S., Bharati, S. J., Singh, N., Khanna, M., Prasad, C. P., Singh, M., Kumar, S., et al. (2019). Feasibility of lung cancer screening in developing countries: challenges, opportunities and way forward. *Translational lung cancer research*, 8(Suppl 1):S106.

Shi, J., Li, D., Liang, D., and He, Y. (2021). Epidemiology and prognosis in young lung cancer patients aged under 45 years old in northern china. *Scientific Reports*, 11(1):6817.

Shintani, T., Matsuo, Y., Iizuka, Y., Mitsuyoshi, T., Umeoka, S., Nakamoto, Y., Mizowaki, T., Togashi, K., and Hiraoka, M. (2017). Assessment of treatment response after lung stereotactic body radiotherapy using diffusion weighted magnetic resonance imaging and positron emission tomography: a pilot study. *European Journal of Radiology*, 92:58–63.

Si, P., Razmi, N., Nur, O., Solanki, S., Pandey, C. M., Gupta, R. K., Malhotra, B. D., Willander, M., and de la Zerda, A. (2021). Gold nanomaterials for optical biosensing and bioimaging. *Nanoscale Advances*, 3(10):2679–2698.

Siegal, T. (2016). Clinical relevance of prognostic and predictive molecular markers in gliomas. *Advances and technical standards in neurosurgery: volume 43*, pages 91–108.

Siegel, R. L., Miller, K. D., Wagle, N. S., and Jemal, A. (2023). Cancer statistics, 2023. *CA: a cancer journal for clinicians*, 73(1):17–48.

Simons, J. (1978). Dynamics of molecules in contact with an external medium at equilibrium. *International Journal of Quantum Chemistry*, 13(4):553–562.

Singh, A., Dev, K., Siljak, H., Joshi, H. D., and Magarini, M. (2021). Quantum internet—applications, functionalities, enabling technologies, challenges, and research directions. *IEEE Communications Surveys & Tutorials*, 23(4):2218–2247.

Skoulidis, F. and Heymach, J. V. (2019). Co-occurring genomic alterations in non-small-cell lung cancer biology and therapy. *Nature Reviews Cancer*, 19(9):495–509.

Slaoui, M. and Fiette, L. (2011). Histopathology procedures: from tissue sampling to histopathological evaluation. *Drug Safety Evaluation: Methods and Protocols*, pages 69–82.

Sohail, A. and Ashiq, U. (2023). Quantum inspired improved ai computing for the sensors of cardiac mechano-biology. *Sensors International*, 4:100212.

Steinkamp, J. and Cook, T. S. (2021). Basic artificial intelligence techniques: natural language processing of radiology reports. *Radiologic Clinics*, 59(6):919–931.

Stenmark, M. H., Cai, X.-W., Shedden, K., Hayman, J. A., Yuan, S., Ritter, T., Ten Haken, R. K., Lawrence, T. S., et al. (2012). Combining physical and biologic parameters to predict radiation-induced lung toxicity in patients with non-small-cell lung cancer treated with definitive radiation therapy. *International Journal of Radiation Oncology* Biology* Physics*, 84(2):e217–e222.

Sullivan, T. B., Bastrom, T., Reighard, F., Jeffords, M., and Newton, P. O. (2017). A novel method for estimating three-dimensional apical vertebral rotation using two-dimensional coronal cobb angle and thoracic kyphosis. *Spine deformity*, 5(4):244–249.

Sun, X., Xu, Y., Wu, J., Zhang, Y., and Sun, K. (2013). Detection of lung cancer tissue by attenuated total reflection–fourier transform infrared spectroscopy—a pilot study of 60 samples. *Journal of surgical research*, 179(1):33–38.

Sun, Y., Lo, F. P.-W., and Lo, B. (2019). Security and privacy for the internet of medical things enabled healthcare systems: A survey. *IEEE Access*, 7:183339–183355.

Tainsky, M. A. (2009). Genomic and proteomic biomarkers for cancer: a multitude of opportunities. *Biochimica et Biophysica Acta (BBA)-Reviews on Cancer*, 1796(2):176–193.

Tal-Ezer, H. and Kosloff, R. (1984). An accurate and efficient scheme for propagating the time dependent schrödinger equation. *The Journal of chemical physics*, 81(9):3967–3971.

Tammemägi, M. C., Ruparel, M., Tremblay, A., Myers, R., Mayo, J., Yee, J., Atkar-Khattra, S., Yuan, R., Cressman, S., English, J., et al. (2022). Uspstf2013 versus

plcom2012 lung cancer screening eligibility criteria (international lung screening trial): interim analysis of a prospective cohort study. *The Lancet Oncology*, 23(1):138–148.

Tammemägi, M. C., Ten Haaf, K., Toumazis, I., Kong, C. Y., Han, S. S., Jeon, J., Commins, J., Riley, T., and Meza, R. (2019). Development and validation of a multivariable lung cancer risk prediction model that includes low-dose computed tomography screening results: a secondary analysis of data from the national lung screening trial. *JAMA network open*, 2(3):e190204–e190204.

Tarasov, P., Isaev, E., Grigoriev, A., and Morgunov, A. (2020). The utilization of perspective quantum technologies in biomedicine. In *Journal of Physics: Conference Series*, volume 1439, page 012040. IOP Publishing.

Tasgin, M. E. (2020). Measuring nonclassicality of single-mode systems. *Journal of Physics B: Atomic, Molecular and Optical Physics*, 53(17):175501.

Tesfa, S. (2012). Role of phase fluctuation and dephasing in the enhancing continuous variable entanglement of a two-photon coherent beat laser. *Chinese Physics B*, 21(1):014204.

Thrall, D. E. (2017). Introduction to radiographic interpretation. *Textbook of veterinary diagnostic radiology*, pages 110–122.

Tseng, M. L., Jahani, Y., Leitis, A., and Altug, H. (2020). Dielectric metasurfaces enabling advanced optical biosensors. *Acs Photonics*, 8(1):47–60.

Uniyal, A., Chauhan, B., Pal, A., and Singh, Y. (2022). Surface plasmon biosensor based on bi 2 te 3 antimonene heterostructure for the detection of cancer cells. *Applied Optics*, 61(13):3711–3719.

Van Loock, P. (2011). Optical hybrid approaches to quantum information. *Laser & Photonics Reviews*, 5(2):167–200.

Vasudevan Pillai Radha, S., Santhakumari Amma Ravindran Nair, S. K., and Sankaranarayana Iyer, S. (2021). Surface plasmon resonance-based fiber-optic metallic multilayer biosensors. *ACS omega*, 6(23):15068–15077.

Venturini, M., Cariati, M., Marra, P., Masala, S., Pereira, P. L., and Carrafiello, G. (2020). Cirse standards of practice on thermal ablation of primary and secondary lung tumours. *CardioVascular and Interventional Radiology*, 43:667–683.

Vu Nhat, P., Si, N. T., Tien, N. T., and Nguyen, M. T. (2021). Theoretical study of the binding of the thiol-containing cysteine amino acid to the silver surface using a cluster model. *The Journal of Physical Chemistry A*, 125(16):3244–3256.

Vyshnevyy, A., Lebedev, A., Lesovik, G., and Blatter, G. (2013). Two-particle entanglement in capacitively coupled mach-zehnder interferometers. *Physical Review B*, 87(16):165302.

Wang, C., Fu, Z., Mao, W., Qie, J., Stone, A. D., and Yang, L. (2023). Non-hermitian optics and photonics: from classical to quantum. *Advances in Optics and Photonics*, 15(2):442–523.

Wang, M., Wang, T., Ojambati, O. S., Duffin, T. J., Kang, K., Lee, T., Scheer, E., Xiang, D., and Nijhuis, C. A. (2022a). Plasmonic phenomena in molecular junctions: Principles and applications. *Nature Reviews Chemistry*, 6(10):681–704.

Wang, Q., Ren, Z.-H., Zhao, W.-M., Wang, L., Yan, X., Zhu, A.-s., Qiu, F.-m., and Zhang, K.-K. (2022b). Research advances on surface plasmon resonance biosensors. *Nanoscale*, 14(3):564–591.

Ward, H. S. (1896). *Practical Radiography: a Hand-book of the Applications of the X-rays*. Pub. for the Photogram, Limited, Dawbarn & Ward, Limited.

Wei, L., Liu, H., Xu, J., Shi, L., Shan, Z., Zhao, B., and Gao, Y. (2023). Quantum machine learning in medical image analysis: A survey. *Neurocomputing*.

Wengerowsky, S., Joshi, S. K., Steinlechner, F., Zichi, J. R., Dobrovolskiy, S. M., Van der Molen, R., Los, J. W., Zwiller, V., Versteegh, M. A., Mura, A., et al. (2019).

Entanglement distribution over a 96-km-long submarine optical fiber. *Proceedings of the National Academy of Sciences*, 116(14):6684–6688.

Wieman, C. E., Pritchard, D. E., and Wineland, D. J. (1999). Atom cooling, trapping, and quantum manipulation. *Reviews of Modern Physics*, 71(2):S253.

Wigle, D. A., Jurisica, I., Radulovich, N., Pintilie, M., Rossant, J., Liu, N., Lu, C., Woodgett, J., Seiden, I., Johnston, M., et al. (2002). Molecular profiling of non-small cell lung cancer and correlation with disease-free survival. *Cancer Research*, 62(11):3005–3008.

Wolf, J. C., Baumgartner, W. A., Blazer, V. S., Camus, A. C., Engelhardt, J. A., Fournie, J. W., Frasca Jr, S., Groman, D. B., Kent, M. L., Khoo, L. H., et al. (2015). Non-lesions, misdiagnoses, missed diagnoses, and other interpretive challenges in fish histopathology studies: a guide for investigators, authors, reviewers, and readers. *Toxicologic pathology*, 43(3):297–325.

Wood, R. W. (1902). Xlii. on a remarkable case of uneven distribution of light in a diffraction grating spectrum. *The London, Edinburgh, and Dublin Philosophical Magazine and Journal of Science*, 4(21):396–402.

Wu, C., Simonetti, M., Rossell, C., Mignardi, M., Mirzazadeh, R., Annaratone, L., Marchiò, C., Sapino, A., Bienko, M., Crosetto, N., et al. (2018a). Rollfish achieves robust quantification of single-molecule rna biomarkers in paraffin-embedded tumor tissue samples. *Communications biology*, 1(1):209.

Wu, W.-T., Chen, C.-H., Chiang, C.-Y., and Chau, L.-K. (2018b). Effect of surface coverage of gold nanoparticles on the refractive index sensitivity in fiber-optic nanoplasmonic sensing. *Sensors*, 18(6):1759.

Xavier, J., Yu, D., Jones, C., Zossimova, E., and Vollmer, F. (2021). Quantum nanophotonic and nanoplasmonic sensing: towards quantum optical bioscience laboratories on chip. *Nanophotonics*, 10(5):1387–1435.

Xu, W., Ling, X., Xiao, J., Dresselhaus, M. S., Kong, J., Xu, H., Liu, Z., and Zhang, J. (2012). Surface enhanced raman spectroscopy on a flat graphene surface. *Proceedings of the National Academy of Sciences*, 109(24):9281–9286.

Yadavendra and Chand, S. (2020). A comparative study of breast cancer tumor classification by classical machine learning methods and deep learning method. *Machine Vision and Applications*, 31(6):46.

Yan, J., Liu, X., Ma, C., Huang, Y., and Yang, G. (2020). All-dielectric materials and related nanophotonic applications. *Materials Science and Engineering: R: Reports*, 141:100563.

Yang, D., Kim, J., Yoo, J., Cha, W. C., Paik, H., et al. (2022). Identifying the risk of sepsis in patients with cancer using digital health care records: Machine learning–based approach. *JMIR Medical Informatics*, 10(6):e37689.

Yang, J., Li, Y., Liu, Q., Li, L., Feng, A., Wang, T., Zheng, S., Xu, A., and Lyu, J. (2020). Brief introduction of medical database and data mining technology in big data era. *Journal of Evidence-Based Medicine*, 13(1):57–69.

Yang, L., Feng, Z., and Meng, J. (2023). An intelligent experimental container suite: using a chemical experiment with virtual-real fusion as an example. *Virtual Reality & Intelligent Hardware*, 5(4):317–337.

Yasli, A. (2021). Cancer detection with surface plasmon resonance-based photonic crystal fiber biosensor. *Plasmonics*, 16(5):1605–1612.

Yeh, C. and Shimabukuro, F. I. (2008). *Fundamental Electromagnetic Field Equations*. Springer.

Yu, D., Humar, M., Meserve, K., Bailey, R. C., Chormaic, S. N., and Vollmer, F. (2021). Whispering-gallery-mode sensors for biological and physical sensing. *Nature reviews methods primers*, 1(1):83.

Yu, H., Peng, Y., Yang, Y., and Li, Z.-Y. (2019). Plasmon-enhanced light–matter interactions and applications. *npj Computational Materials*, 5(1):45.

Yung, R. (2003). Tissue diagnosis of suspected lung cancer: selecting between bronchoscopy, transthoracic needle aspiration, and resectional biopsy. *Respiratory care clinics of North America*, 9(1):51–76.

Zhang, C., Xue, T., Zhang, J., Liu, L., Xie, J., Wang, G., Yao, J., Zhu, W., and Ye, X. (2021). Terahertz toroidal metasurface biosensor for sensitive distinction of lung cancer cells. *Nanophotonics*, 11(1):101–109.

Zhang, C., Xue, T., Zhang, J., Liu, L., Xie, J., Wang, G., Yao, J., Zhu, W., and Ye, X. (2022). Terahertz toroidal metasurface biosensor for sensitive distinction of lung cancer cells. *Nanophotonics*, 11(1):101–109.

Zhang, C.-Y. and Zheng, Z.-J. (2021). Entanglement-based quantum key distribution with untrusted third party. *Quantum Information Processing*, 20:1–20.

Zheng, J., Almossalami, H. A., Chen, K., Yu, X., and Ye, H. (2021). Permittivity acquisition of plasmonic materials at epsilon near zero wavelengths. *Journal of Applied Physics*, 129(10):103101.